Thèse de doctorat

Présentée et soutenue publiquement pour l'obtention du titre de

DOCTEUR DE L'UNIVERSITE DE LORRAINE

dans la spécialité: «**Physique**»

par **Anton KYIANYTSIA**

Propriétés magnétiques et magnétoélastiques de l'alliage à mémoire de forme NiTi et de la bicouche NiTi/Ni

Magnetic and magnetoelastic properties of NiTi shape memory alloy and NiTi/Ni bilayer

le 16 décembre 2019

Membres de jury :

Mme. Silvana Mercone	Rapportrice	Maître de Conférences, Université Paris 13 - LSPM
M. Vincent Repain	Rapporteur	Professeur, Université Paris Diderot -MPQ
Mme. Laura Thevenard	Examinatrice	Chargé de Recherche, Sorbonne Université - INSP
M. Jean-Marc Raulot	Examinateur	Professeur, Université de Lorraine-LEM3
M. Thomas Hauet	Directeur	Maître de Conférences, Université de Lorraine - IJL
M. Bertrand Kierren	Co-directeur	Professeur, Université de Lorraine - IJL
M. Sébastien Palay	Invité	PDG de Cryoscan

Institut Jean Lamour - UMR CNRS 7198
Université de Lorraine - Faculté des Sciences et Technologies
CRYOSCAN SAS

Résumé

L'objectif initial de la thèse est d'étudier la manipulation de l'anisotropie magnétique d'une couche mince ferromagnétique par déformation par couplage élastique avec un alliage à mémoire de forme NiTi. Premièrement, les caractéristiques structurales et la nature paramagnétique du NiTi sont étudiées en détails. Ensuite, le couplage magnétoélastique dans une bicouche NiTi / Ni est étudié.

Dans la première partie, les caractéristiques paramagnétiques d'un échantillon polycristallin de NiTi autoporté de 20 μm d'épaisseur, fabriqué par pulvérisation cathodique magnétron, sont étudiées à l'aide de magnétomètres, en fonction du champ magnétique, de la température, de la structure cristalline et des contraintes mécaniques. La structure en NiTi est caractérisée par la diffraction des rayons X, notamment en relation avec son état de déformation. Les échantillons sont déformés en tension dans la large gamme de magnitudes de déformation, la distribution des contraintes est caractérisée par une technique numérique de corrélation d'images. Nous montrons que la magnétométrie est une technique efficace pour sonder les états de transition et de déformation des alliages à mémoire de forme. Les variations de la susceptibilité magnétique de NiTi sont expliquées sur la base de la théorie du paramagnétisme de Pauli, en comparant les données expérimentales à des calculs ab-initio. La relation entre susceptibilité, densité d'état au niveau de Fermi et paramètres de maille est mise en lumière via les variations induites par les contraintes de traction.

Dans la deuxième partie, nous montrons que, dans la bicouche NiTi/Ni, l'effet de mémoire de forme dans le film NiTi libre permet d'induire et de commuter de manière réversible à 90° l'anisotropie magnétique uniaxiale induite dans la couche de Ni. La commutation est réalisée par un cycle thermique entre 300K et 400K. L'amplitude du changement d'anisotropie magnétique au cours d'un cycle thermique est dépendante de la valeur de pré-contrainte, qui est réglable. La qualité de l'interface de la bicouche est étudiée à l'aide de la technique de microscopie électronique à transmission (TEM). Le taux de transmission de la contrainte de NiTi à Ni est estimé indépendamment à partir de la distribution de la contrainte dans NiTi, de l'amplitude de l'anisotropie magnétique du Ni et vérifié par TEM.

Mots-clés: magnétoélasticité, magnétique, alliage à mémoire de forme, NiTi, Ni.

Abstract

The initial goal of the thesis is to investigate the manipulation of magnetic anisotropy of a ferromagnetic thin layer through strain by means of shape memory effect in NiTi/ferromagnetic bilayer. First, the structural features and paramagnetic nature of NiTi are broadly studied. Then, magnetoelastic coupling in NiTi/Ni bilayer is investigated.

In the first part, paramagnetic features of a freestanding 20μm thick NiTi polycrystalline samples grown by magnetron sputtering are studied with commercial magnetometers, as a function of a magnetic field, temperature, crystal structure, and mechanical strain. NiTi structure is characterized by X-ray diffraction, particularly in relation to its strain state. The samples are deformed in tension in the broad range of deformation magnitudes, the strain distribution is characterized by digital image correlation technique. Magnetometry is demonstrated to be an efficient technique for probing of shape memory alloys transition and strain state. Variations of NiTi magnetic susceptibility are explained based on considerations that NiTi is Pauli paramagnetic material by comparing experimental data with ab-initio calculations. It is found that magnetic susceptibility depends on particular trends in NiTi lattice parameters induced by tensile strain.

In the second part, we prove that shape memory effect in freestanding NiTi is viable to induce and reversibly switch by 90° a uniaxial magnetic anisotropy of the Ni layer deposited on top of it. Switching is accomplished by thermal cycling between 300K and 400K. The magnitude of magnetic anisotropy change during a thermal cycle is shown to be dependent on the pre-strain value, that is tunable. The interface quality of the bilayer is investigated with the transmission electron microscopy (TEM) technique. Consistent strain transmission rate to Ni from NiTi is independently estimated from strain distribution in NiTi, from Ni magnetic anisotropy magnitude and verified by TEM.

Keywords: magnetoelasticity, magnetic, shape memory alloy, NiTi, Ni

Acknowledgments

Here I would like to thank a lot of people who made this thesis possible in one or another way. At first, I would like to thank my supervisor Thomas Hauet for his invaluable help, advice and ideas that he has been constantly providing me during these four years. His abilities to encourage and to motivate were crucial for me to went through the hardest periods of this PhD study. I want to thank Dr. Bertrand Kierren, my co-advisor, his polymathic and insightful mind has been inspiring our discussions. I want also to thank him and Cryoscan company for my financial (and not only financial) support during this thesis and even behind initial contractual obligations. I would like to thank also the whole team of Cryoscan company, who warmly welcomed me during the first years, especially to Luc Moreau, Sebastien Palay, Roman Charleux, Gauthier Wirth, Sarah Xing, Stephane Devaux.

I am grateful to Mme. Silvana Mercone, M. Vincent Repain, Mme. Laura Thevenard, and M. Jean-Marc Raulot for accepting to be a part of my jury and for valuable comments and corrections they have proposed.

I owe many thanks to people from different departments and competence centers of Institut Jean Lamour, without their help and expertise this work would not be possible. I thank Pascal Boulet, the head of CC X-Gamma, with whom we spent many pleasant hours in front of a diffractometer discussing the results or launching numerous measurements. I also want to express my gratitude to Sylvie Robert and Ghouti Medjahdi, who helped me a lot with XRD measurements. To Crosby Chang, Tom Ferte and Stephane Suire from CC Magnetometry for their availability and help in the measurements and fixing the problems (including my faults). I want to thank the team of CC 3M, especially Jaafar Ghanbaja, Sylvie Migot and Christine Genderme for their great work, that they have done to characterize my samples, their reactiveness and beautiful pictures Jaafar obtained with my messy samples.

I want to express my appreciation to Marc Poncot and Adrien Letoffe, their help with strain experiments and their openness to collaboration played an important role in the success of this work, as well as ab-initio calculations done by Emilie Gaudry and I want to thank her for this.

I want to address my special thanks to all the members of 101 Spintronic and nanomagnetism team: professors, old and new PostDocs and PhD students. Their competences and help, as well as their human qualities and attitude made my life during

these years much better and pleasant. Special thanks to Gauthier Masset, Elodie Martin, Ibrahim Cinar, Kosseila Ait Oukaci, Mariam Massouras, Elmer Monteblanco, Filip Schleicher, Marwan Deb, Jean-Lois Bello, Charles Guillemard, Quentin Remy, Claudia Sanchez De Melo , Yassine Quessab, Vincent Polewczyk, Alexandre Dekens, Pierre Vallobra, Thibaud Fache, Huyen Nong, Philippe Scheid, Boris Seng, Boyu Zhang, Maxime Verges and to the professors: Jon Gorchon, Carlos Rojas Sanchez, Sébastien Petit-Watelot, Julius Hohlfeld, François Montaigne, Stéphane Mangin, Grégory Malinowski, Daniel Lacour, Michel Hehn, Karine Dumesnil, Olivier Copie, Stéphane Andrieu.

Last but not least, I want to acknowledge the huge contribution of my mother and father, who inspired me to dig into science, and always were ready to help and support me in any circumstances. And, the main motivation and reinforcement, unlimited source of energy and relief during these years was my wife Maryna, who shared with me all the joy and sorrow of our new life abroad. Without her I could not finish this work.

Table of Contents

General introduction

Many existing or developing technologies rely on controlling of magnetization direction of a ferromagnet: microelectronic sensors, actuators and especially memory technologies, such as hard disk drive (HDD) or magnetic random-access memory (MRAM), etc. Accelerating technological progress requires not only higher capacity data storage but also the new efficient approaches for reducing the power needed for rewriting of the bit. This brings to the forefront the research on magnetic anisotropy control.

On the other hand, there is constantly growing interest over the last decades in materials with additional functionalities whose properties could be tailored. Such alloys and composites capable for sensing or actuation are called active materials [1]. A remarkable group of active materials is shape memory alloys (SMA), which are capable to exhibit the largest strains among the other active materials. Strain output is driven by thermoelastic phase transformation, while both the temperature and strain magnitudes may be tuned. Sputter deposition is proved[2], [3] to produce reliable and highly performing NiTi-based SMAs, together with developing of fabrication technologies [4]–[6], it allows integration of SMAs to microsystems.

Therefore, utilizing shape memory alloys for magnetic anisotropy control looks promising for the role of a non-volatile low-power system with tunable functionality and potential to be integrated into magnetic recording technologies. Thus, the first experimental results on the realization of this approach were done in 2016 by Feng et al.[4]–[6].

Within this context, the aim of the thesis is to investigate the manipulation of magnetic anisotropy in ferromagnet by shape memory alloy. But, also, to study paramagnetic features of the NiTi shape memory alloy itself. In the first chapter, the mechanisms and the means of magnetic anisotropy control are discussed. Then, the essential background concerning shape memory alloys is given. Before starting the study of magnetic anisotropy control in Ni by shape memory effect in NiTi in Chapter IV, we firstly decided to investigate the magnetic response from the NiTi. Meanwhile, interesting paramagnetic features were found and mainly fundamental interest to physical properties but also some practical aspects of investigation of NiTi through magnetometry led us to the broader study of NiTi, which is presented in Chapter II, and, then, in Chapter III, where the influence of strain on magnetic properties and structure is studied.

CHAPTER I. **BACKGROUND: MAGNETIC ANISOTROPY CONTROL AND SHAPE MEMORY ALLOYS**

I.1. **Control of magnetic anisotropy**

Some of the existing approaches for magnetic properties manipulation are briefly reviewed in the following in order to put the subject of the thesis in the context and to justify its choice.

I.1.1. Magnetic anisotropy induced by interfaces

Magnetic anisotropy is one of the key properties of magnetic materials. Magnetic anisotropy consists in the ability of ferromagnetic material to have a preferential orientation of magnetization along with certain crystallographic directions. Practically it means that ferromagnetic material may be magnetized and saturated more easily along one certain direction, which is called easy axis (EA). Conversely, magnetization along another direction (hard axis) requires a higher magnetic field. In a monocrystalline ferromagnet, the easy axis is usually well defined along with its crystal directions, and magnetic anisotropy symmetry corresponds to crystal type, e.g. cubic or hexagonal. For example, the easy axis in Fe cubic crystal lies along [100] and the hard axis along [111], while in Ni it is inverse. Such a difference in anisotropies of both materials results in very weak anisotropy of their alloy, so-called Permalloy.

Magnetic anisotropy direction is related to crystal axis because it results from a combined effect of spin-orbit coupling and crystal field interaction (coupling between electron orbitals and lattice). Therefore a change in the electronic structure leads to a change of magnetic anisotropy. Modification of electronic structure may be induced by the effects on the interface of magnetic material and/or by external influences. For instance, it may also be due to the crystalline phase transition in temperature.

When working with thin and ultra-thin films composed of multiple layers [7], interface effects lead to remarkable properties. As thin films are usually produced by different sputtering or evaporation technics, there is a lot of possibilities to tune magnetic properties by growth method, conditions and by varying the interface[7]. Strain, chemical

intermixing and surface morphology[7] may have a strong influence on electronic properties at the interface. For example, it is possible to induce perpendicular magnetic anisotropy in NiFe (111) by evaporation onto atomically flat Cu(111) substrate[8]. Also, intrinsic magnetic anisotropy may be enhanced in hundred times by alloying with Pt[9], [10]. Hybridization between Fe 3d and Pt 5d states leads to an enhancement of spin-orbit coupling. On the other hand, the stress, caused by epitaxial misfits between the substrate and magnetic layer lattices may induce certain magnetic anisotropy in the latter by magnetoelastic coupling[11], [12] or favor some particular crystal orientation[13]. These methods are good for inducing magnetic anisotropy, but once it is induced, it is very hard to be modified. In what follows, we will look at the methods, that allow to reversibly control magnetic anisotropy.

In order to manipulate magnetic anisotropy or to switch magnetization, there are several methods to do it, besides direct magnetic field application. Voltage, polarized current, spin current, heat or polarized light are used as external excitation sources to orient the magnetic moment. Among them, the voltage control is one of the most attractive[14] methods because of the low power dissipation, reversibility, nonvolatility, possibility of working on high frequencies and good compatibility with conventional industry technologies. Despite the method of control is the same, there are several different physical mechanisms can stand behind. Charge carrier densities modification based mechanism has been observed in magnetic metals, ferromagnetic semiconductors and oxides[15]. The famous example is the Fe/MgO[16] junction or MgO/CoFeB/Ta[17], where a significant change of interface magnetic anisotropy was caused by the electric field. In Fe/MgO stack, hybridization between the Fe 3d and O 2p orbitals modifies the electronic structure and the interface, which induces certain magnetic anisotropy in Fe. Applying magnetic field changes Fermi energy position and magnetic anisotropy in Fe may be modulated[18].

A large group of materials, so-called multiferroic composite materials, also combine magnetoelectric coupling and/or magnetoelastic coupling. In conventional examples of artificial multiferroics composites, ferromagnetic material is coupled to ferroelectric, piezoelectric or flexible polymer-based material. In the first case, the magnetic field is coupled to applied voltage through electrical polarization. One of such system example[18] is perovskite manganite, as a ferromagnetic $La_{1-x}Sr_xMnO3$(LSMO) coupled with ferroelectric $BaTiO_3$. Change of ferroelectric polarization in BTO leads to change in the lattice strain and/or charge carrier modulation at the interface. Both can

modulate Curie temperature and magnetization on changing the polarization of the ferroelectric.

The case of piezoelectric/magnetostrictive composites is probably one of the most matured one [14], [19]–[22]. Here, magnetic anisotropy may be tuned by strain transferred from piezoelectric material. Very small voltages are sufficient to induce the directional strain due to the inverse piezoelectric effect and to switch the magnetization of the magnetic layer[23]. Growing demand on low-power technologies for computing and information storage motivates such research. Therefore, so-called straintronics research field emerged[19], [23], [24], that unite the strain effects to develop a new generation of low power information, sensor and energy technologies. For example, in the domain of magnetic storage technologies, "straintronic" magnetic tunneling junction(MTJ) (see [25] and references inside), or strain-assisted spin-orbit torque switching[26] have been studied during last years.

Such a relation between mechanical strain and magnetic properties is generally called magnetoelastic coupling. Well-known magnetostriction phenomena, which consists in changing the sample's dimensions as a result of magnetic moments aligning in the response to applied magnetic field or cooling under curie temperature, is the manifestation of magnetoelastic coupling. Magnetostriction is usually characterized by saturation magnetostriction coefficient λ_s, which is simply the maximum strain of the saturated sample along the field comparing to the demagnetized sample. Depending on the mutual orientation of applied magnetic field and strain, λ_s can have positive, negative value or even zero. The inverse effect, when magnetic properties affected by strain is called Villari or magnetoelastic effect.

Stress, applied to magnetic material may change the range of its properties, as magnetic anisotropy, coercive field or Curie temperature, as was mentioned before. Therefore, there is a various and complex physical mechanism behind that. In general, lattice strain in magnetic material causes the change of distances between the atoms. This change, or strain in other worlds, modifies the strength or character of spin-orbit or dipole-dipole coupling[19] between the magnetic moments or atoms, that lead to a change of magnetic anisotropy.

The general equation describing magneto-elastic coupling in the cubic crystal structure is magnetoelastic energy density (only first-order terms) [11],[27] is:

$$E_{me} = B_1\left[\varepsilon_{xx}\left(\alpha_1^2 - \frac{1}{3}\right) + \varepsilon_{yy}\left(\alpha_2^2 - \frac{1}{3}\right) + \varepsilon_{zz}\left(\alpha_3^2 - \frac{1}{3}\right)\right] + B_2\left(\varepsilon_{xy}\alpha_1\alpha_2 + \varepsilon_{yz}\alpha_2\alpha_3 + \varepsilon_{xz}\alpha_1\alpha_3\right) \quad (1)$$

Where ε_{ij} represents the strain tensor and α_i are the direction cosines with respect to the main strain direction. $B_{1,2}$ are magneto-elastic coupling coefficients, which are related to magnetostriction coefficients by elastic constants as[11]:

$$\lambda_{100} = -\frac{2}{3}\frac{B_1}{(c_{11}-c_{12})}\ ,\ \lambda_{111} = -\frac{1}{3}\frac{B_2}{c_{44}} \quad (2)$$

where $c_{i,j}$ is elastic constant.

I.1.2. Thermally triggered magnetic anisotropy

In the field of magnetic recording and storage, there are two promising emergent technologies that are about to enter the market: spin-transfer torque magnetoresistive random access memory (STT-MRAM) and heat-assisted magnetic recording (HAMR).

On the one hand, magnetic random-access memory(MRAM) is the conventional technology, dominated in the market of magnetic storage since its developing in the 1980s[28]. MRAM stores the data as the magnetic bits, which consists in the so-called magnetic tunnel junction. Based on the tunnel magnetoresistance effect, “0” or “1” of such a cell can be read-out by measuring its electrical resistance. STT (spin-transfer torque) benefits from spin-polarized current in magnetic tunnel junction in order to switch its free magnetic layer and is used to write data. Writing still induces heat in the free layer and thermal fluctuations during electrical pulse remain a problem for such systems[29].

On the other hand, a new generation of HDD using the heat-assisted magnetic recording (HAMR) developed by Seagate is already at the stage of consumer testing[30]. Here laser heating delivered to the cell by waveguides [31]is used to reduce its coercivity by approaching Curie temperature and then to write information at low magnetic fields, reducing power consumption.

In both technologies, magnetic media experiences heat and it needs to be managed. Unwanted heat could be reduced if the media anisotropy could be independently decreased during the writing phase. On the other hand, heat may be used as a trigger. Changing the properties of the material as the response to heat can be observed everywhere, but there is increasing interest in materials, which undergo a phase transition in temperature. These materials show an interplay between its structural,

electronic and magnetic properties[29]. An interesting example is FeRh alloy, that transforms from low temperature antiferromagnetic phase to high temperature ferromagnetic phase[32]. Or V_2O_3, which demonstrates the transition between paramagnetic metal and antiferromagnetic insulator phases. The large group of first-order phase transition materials is martensite transformation materials, which transform from monoclinic martensite phase at low temperature to cubic austenite phase at high temperature.

I.1.3. Shape memory alloy as a functional layer to trigger strain transfer and magnetic anisotropy change in a ferromagnetic layer

Martensite transformation is responsible for shape memory effect in the so-called shape memory alloys (SMA) which can exhibit large strains upon temperature transitions. Regarding the demand of non-volatile systems and looking back to the growing interest to the heterostructures, where the strain results in the change of magnetic, electronic or transport properties, as piezoelectric/ferroelectric + ferromagnetic composite or straintronic devices, utilizing shape memory alloys for magnetic anisotropy control looks promising.

In contrast to multiferroic composites, the shape memory alloys-based composites exhibit pure strain effect. The strain amplitudes are nearly in order of magnitude larger than in piezoelectric materials[33], which opens the possibility for stronger interfacial effects and for manipulation of harder magnetic materials. Such great strains originate from shape memory effect (SME), which can be artificially induced and tuned. For now, NiTi-based SMA exhibit the largest work output among the other active materials[1]. Another property, that motivates applications of SMAs is superelasticity, which allows material to sustain the great deformations and recover its previous shape upon unloading. Nowadays due to such remarkable properties as shape memory effect and pseudoelasticity, shape memory alloys have found numerous applications in the microactuators [34] and MEMS [35], in medicine [36]-[37], automotive devices [38] and aerospace [39]. Moreover developed fabrication technologies[3], [33] of shape memory alloys allow growing freestanding microfilms, deposition on required surfaces, together with micropatterning manufacturing expands its potential to information technologies, spintronic devices, and microsensors.

The idea of a strain assisted memory device for spintronic technologies based on shape memory alloy was proposed by Hauet et al. in the patent[40]. In 2016, Feng et al.[4]–[6] performed the first experimental realization of this approach using a thermally controlled NiTiNb shape memory alloy. They obtained pioneer results and show variation of coercive field H_c in NiTiNb(0.5mm)/FePt(10-20nm) and tuning of magnetic anisotropy field H_k in NiTiNb(0.5mm)/Fe(2-5nm), both with in-plane anisotropy. X-ray photoemission spectroscopy and ab-initio calculations demonstrated that lattice strains up to 2% transferred from NiTiNb significantly modify the spin-orbit coupling, orbital overlap and electronic density of states in the deposited film.

Showed feasibility of this approach and the hysteretic nature of martensite transformation motivated us to continue this research and explore the possibility of magnetization reversal in a similar system. Another motivation was an idea (and consequently proposed patent) about SMA/ferromagnetic based temperature threshold sensor. The basic mechanism of the sensor is that it irreversibly, in the known and controllable limits, switches its magnetization direction when the threshold temperature is exceeded. The particularity of this sensor is that it is completely non-volatile, and the result may be read by means of an external contactless device or it can be visualized on the top of the sensor by means of film containing magnetic suspending.

For the role of shape memory alloy in this study nearly equiatomic NiTi (also known as “Nitinol”) is selected. It was the first metallic alloy, where the shape memory effect(SME) was discovered in 1959[41], and still, NiTi and NiTi-based alloys are the most preferable SMAs for applications[33] because of its superior mechanical characteristics and thermo-mechanical performance. NiTi-based SMAs can produce as much as 4% of reversible strain (two-way shape memory effect) and recover up to 10% (one-way shape memory effect) of the initial deformation[42], [43]. The transformation temperatures can be tuned from 250K to 1000K[33]. Thermal hysteresis width can be adjusted from a few Kelvin [44] up to about 80°K [45]. Finally, SME is scalable down to the nanometer scale[46] and its triggering time is mostly limited by the actuation mechanism, and on our knowledge, it was reduced to 20μs [47].

The study of magnetic anisotropy control by shape memory effect is presented in the last chapter. Broad investigation of NiTi itself is done and presented before, therefore some basics of shape memory alloys will be given in the next section.

I.2. **NiTi shape memory alloys**

In the following, the essential information about NiTi shape memory alloys, needed for discussion in the next chapters, will be given.

I.2.1. Shape memory effect and pseudoelasticity

Shape memory alloys are remarkable materials due to their unique properties of shape memory effect (SME) and pseudoelasticity, as in Figure 1[1]. SME consists in the ability of a material that has been deformed to recover its original shape by heating it. On the other hand, PE means that material accommodates reversibly large amounts of stress during the loading-unloading cycles, for instance, NiTi wire typically recovers 8% strain, which is at least 80 times larger than the conventional elastic strain in metals [48]. These properties are the manifestation of phase change, called martensite transformation (MT).

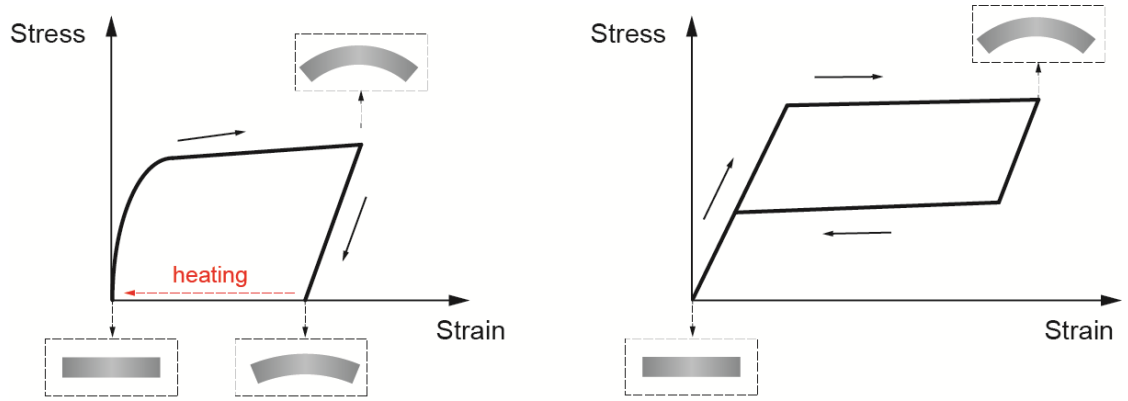

Figure 1. Shape-memory effect (left) and pseudoelasticity (right) in stress-strain plots, bending of the sample as an example of deformation.

I.2.2. Martensite transformation

Martensite transformation is the first order reversible phase transformation. Transformation occurs between high temperature austenite phase (parent phase) and low temperature martensite phase (product phase). This transformation occurs in a hysteretic manner as it is schematically represented in Figure 2, where Ms and Mf are the common notations for temperatures corresponding to start and finish of martensite formation from austenite upon cooling. As and Af are respectively start and finish temperatures of austenite formation on heating. These temperatures are extremely sensitive to chemical

composition and depend on post-treatment [49]. For instance, a 1% reducing of Ni atoms in NiTi alloy may lead to approximately 50°K shift of thermal hysteresis towards low temperatures.

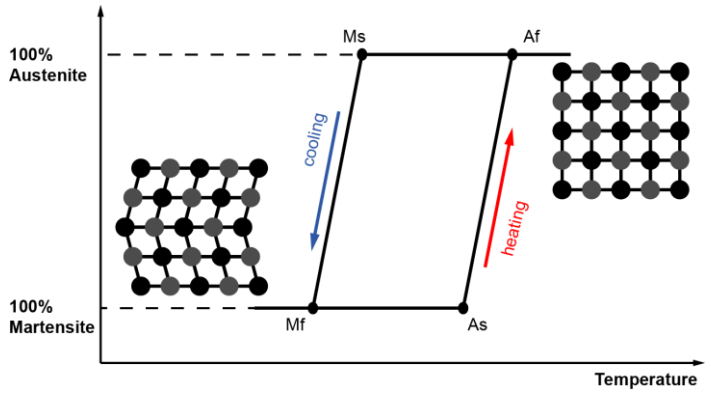

Figure 2. Notional thermal hysteresis of phase transformation in NiTi SMA. Crystal structure on the left schematically represents monoclinic twinned structure of martensite at temperatures below Mf, on the right – cubic structure of austenite phase at temperatures above Af.

Hysteresis between direct and reverse martensite transformation is accounted, for constrains at martensite boundaries and, on the other hand, for hysteretic energy barrier upon transformation between B2 cubic crystal structure in austenite and B19' monoclinic structure of martensite[50]. Martensite transformation occurs by cooperative shear-dominant atom motion[48] as described in Figure 3, taken from [50]. The initial B2 phase can be seen as a tetragonal phase, on the intersection of 4 cubic cells. Then tetragonal phase transforms into B19 phase by orthorhombic distortion along [010]B19 direction and a shuffle of interior Ni and Ti atoms. The next step consists in a shear distortion of the orthorhombic phase and planar shuffle, resulting in the monoclinic B19' structure with an angle around 97° between a and c. Actually, in the literature, the angle value varies from 96° to 98° [51]. Paper to paper variation of this angle is very rarely discussed.

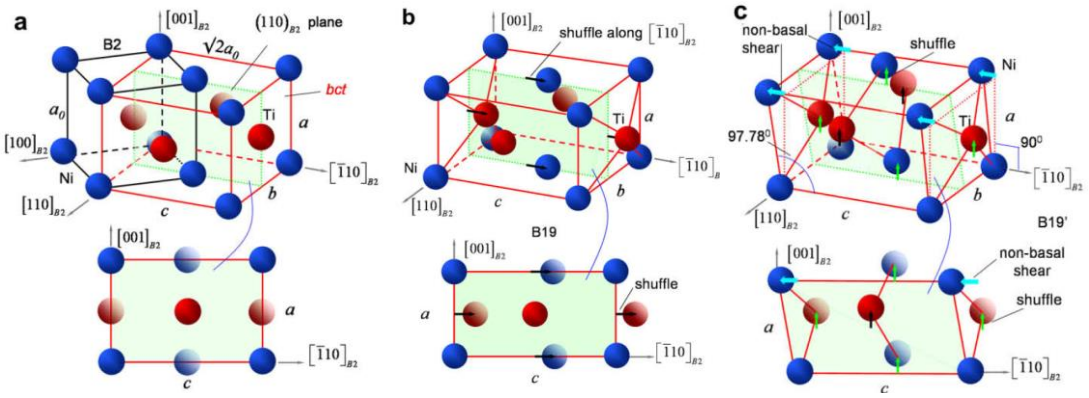

Figure 3. Martensite transformation in 3 stages: (a) structure relationship between B2 cubic phase and body-centered tetragonal phase; (b) orthorhombic B19 structure and (c) monoclinic B19' martensite with shear and shuffle. Figure is from ref. [52].

An important feature of this process is the absence of atom diffusion, which means that the atoms move over the distances smaller than interatomic distance and it makes transformation almost instantaneous. As a consequence martensite phase transformation velocity approaches the speed of the sound [52]. At any point between Ms and Mf or As and Af, NiTi contains the mixture of phases. For example, during the cooling from Ms temperature, martensite variants nucleate and grow inside the austenite grains in the form of lenticular plates, which grow along certain planes. Such an interface plane that separates two phases is called invariant (habit) plane (see Figure 4).

The crystallographic transformation described above involves a change of material physical properties, which are often used to detect martensite transformation. For example, utilizing the change of latent heat or resistivity[1]. Detection by means of magnetic measurements will be investigated in detail later in Chapter II.

The mechanism responsible for minimizing the strains during martensite transformation is called lattice invariant shear and it works by two different mechanisms: twinning or slip. In the case of NiTi, as more generally SMAs, the main mechanism is twinning. That is why in zero-stress conditions martensite phase of NiTi consists of martensites of different directions which are twin-related to each other (Figure 4), hereinafter will be called twinned martensite. Each twin consists of martensite unit cell of two different crystallographic orientation with respect to the austenite phase. These unit cells of different orientations are called martensite variants. For instance in NiTi alloys up to 24 different martensite variants can be formed upon martensite transformation[1].

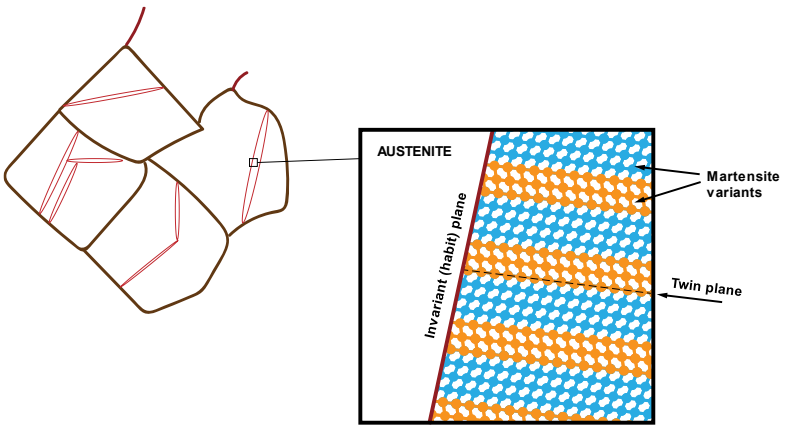

Figure 4. Martensite plates nucleation in austenite grains (on the left). Schematically illustrated twinned martensite near martensite-austenite interface (on the right).

If stress is applied to such twinned self-accommodate martensite, the most preferred variant according to stress direction will grow at the cost of other variants, which eventually can lead to single variant martensite. This is known as the detwinning of martensite (like in Figure 5). What happens to the material under applied stress will be discussed in more detail in the section I.2.4.

The process of martensite transformation in NiTi in some conditions may include also intermediate R-phase, which stands for rhombohedral crystal structure. This transformation takes place prior to the start of martensite growing on cooling and can be formed by elongating along any of the diagonals of the cubic cell. R-phase is also reversible transformation, but its hysteresis is very small comparing to martensite transformation, and it is usually in the range of few °K. R-phase could appear in NiTi as a consequence of certain thermo-mechanical treatment, substituting of Ni with small amounts of Al or Fe, precipitates formation or large enough deformations [53].

To summarize the mechanism of martensite transformation it should be pointed out that there are two main processes responsible for it: cooperative shear-dominant atom motion and twinning. It makes martensite transformation reversible and diffusionless with no observable strain in macroscale because of the formation of martensite variants in such a way to accommodate the strain.

I.2.3. Shape memory effect

In Figure 5 from Mohd Jani review paper [33], all the main effects taking place in SMA are clearly presented. Shape memory and pseudoelasticity effects represented schematically in terms of martensite or austenite crystal structure in coordinates of temperature, stress, and strain.

When an external force is applied to the sample in the martensite phase (at a temperature below M_f), martensite undergoes detwinning processes resulting in a bent wire as sketched in Figure 5 (a) to (b). After removing the force, at stage (c) in Figure 5, the wire remains bent and if we heat it above A_f, the wire restores its previous shape as a consequence of reverse martensite transformation to austenite (d). Then during cooling, transformation to martensite occurs and the martensite phase as before bending is obtained in stage (a) due to the self-accommodating manner of martensite, which is growing from the same parent austenite phase. During subsequent heating-cooling cycles, the same structural changes occur. The process described above is a convenient

shape memory effect, which is the direct consequence of martensitic transformation. It is also called a one-way shape memory effect.

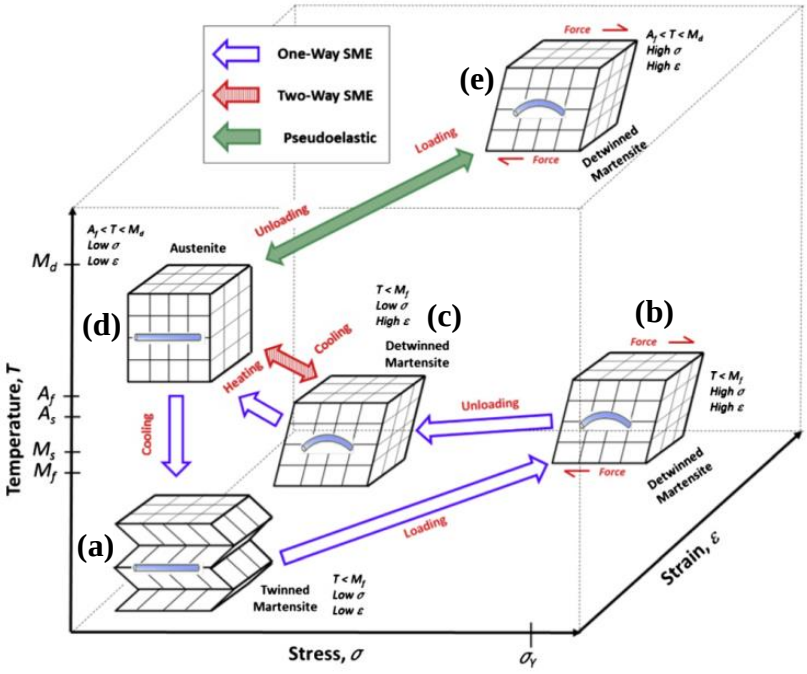

Figure 5. Shape memory effect and pseudoelasticity as a function of stress, strain, and temperature. Correspondent crystallographic change and deformation of the sample schematically depicted. Figure from [33].

In contrast to intrinsic SME, it is also possible to "remember" two different shapes on heating and cooling without applying external force each time after heating (red arrow between (c) and (d) stage in Figure 5. In that case, it is called a two-way SME. Unlike one-way SME, which is an intrinsic property of thermoelastic martensite transformation, to acquire two-way SME certain training procedures must be done. Commonly accepted that the aim of these procedures is to create certain sources of oriented stress, as an anisotropic dislocation field, precipitations, etc. Dislocation field and preferentially reoriented variants in turn create stress fields, which control the arrangement of variants to grow in preferential orientation [43],[54]–[56].

Several different approaches to training are usually used [43], [56]–[58]:

- Shape memory cycling (cycling of one-way SME, deformation below Ms then heating to austenite and back, after a certain amount of repetitions the sample begins to change its shape upon cooling).

- Deformation of martensite via martensite reorientation (introduction of internal plastic strains by martensite deformation over the usual recovering limit).
- Thermal cycling of the constrained sample (deformed sample temperature cycling between martensite and austenite phases).
- Pseudoelastic training (mechanical loading-unloading in the pseudoelastic regime, that is stress-induced martensite formation above Af and below Md).

Two-way SME is very useful to commute an object from a selected shape to another selected shape, independently of the original shape in as-grown martensite material. Nevertheless, one has to highlight that two-way SME demonstrates a significantly smaller ability to shape regaining than one-way SME. Maximum recovered strains in the case of one-way SME in NiTi typically around 10% contrary to ~4% for the two-way effect [33], [43].

I.2.4. NiTi under external stress

The influence of tensile strain on the magnetic properties of NiTi will be heavily discussed in Chapter III. Therefore, in the following, we focus on the processes taking place in NiTi alloy under tensile stress only and in the martensite phase only.

Figure 6 shows the typical stress-strain curve of NiTi sample during tensile stress. Normally it consists of 4 main stages [59]. At stage 1, which ends before 1% elongation, deformation is elastic, and the structure of twinned martensite shouldn't change. For stress plateau at stage 2, (b to c in Figure 6), detwinning of dominated [011] Type II twin and martensite reorientation processes are driving mechanisms. Note, that completely detwinned grain in Figure 6 at point *c* is rather a simplification, internal constraints usually don't allow complete detwinning. Martensite reorientation term usually refers to lattice orientation change and motion of the interfaces between two neighboring habit plane variants[60], [61] and it results in detwinning of reoriented martensite variants. Stage 3 (d to g in Figure 6) is characterized by the significant increase in the stress by further reorientation and detwinning. (001) compound twins, as well as dislocation network growth, is usually observed at this stage. Additionally, (100) and (20-1) twins can be inserted in the (001) twin. After apparent yield at stage 4, plastic deformation

dominates and leads eventually to fracture. At this stage (20-1) and (113) deformation twinning and dislocations processes are dominant.

Deformation mechanism of martensite is fairly complex, and the general picture stated above may be supplemented by numerous details and discrepancies as shown in a literature [59],[62]. For example, inelastic contributions in the stress-strain curve have been already observed at stage 1 after unload. Also, there are studies[43],[63] showing the evidence of dislocations emergence at stage 2 and it is suggested that martensite reorientation deformation and even pure thermo-elastic transformation of the polycrystalline sample is necessarily followed by defects formation. In particular, this is due to the different crystallographic orientations between neighboring grains which lead to orientation mismatches between variants on grain boundaries during deformation. So, to achieve martensite reorientation in the preferred direction of external tension, misoriented variants are compensated by plastic deformation. It has been observed that the tensile deformation of martensite to less than 4% leads to the emergence of dislocations [64].

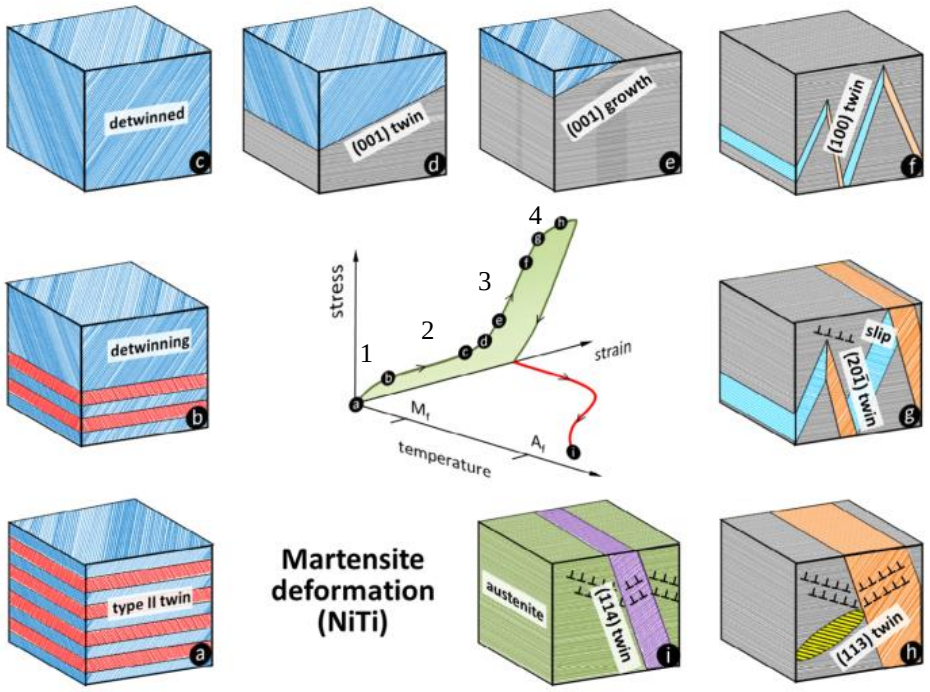

Figure 6. In the center, typical stress/strain curve of NiTi on tension; Scheme (a-i) represents NiTi structure from [62], at different deformation stages processes of initial detwinning, then growing of various deformation twins and dislocations by slip (T-shape signs).

Usually, the sample doesn't recover completely its initial shape in austenite as shown in Figure 6, Unrecovered plastic strain ε_{pl} occurs in shape memory effect, whose amplitude nonlinearly increases with increasing pre-strain ε_{max} until ε_{pl} dominates at some point at stage 4. The amount of irrecoverable strain is usually accounted for the {20-1} and {113} deformation twins which cannot transform into a single cubic phase of austenite[65]. Another significant reason is the defects, such as dislocations, which are most commonly observed in NiTi, and point defects. Such structures lower the correspondence of martensite to austenite phase[42]. These two reasons may cause the (114) and (112) twins, which have been observed in austenite (Figure 6, point i)[62]. Closely related to the mentioned above mechanism of dislocation formation is the phenomenon of transformation stabilization and thermomechanical fatigue[45],[60].

I.2.5. Literature overview on the subject of magnetism in NiTi.

Nitinol (NiTi) is one of the most heavily studied and widely used shape memory alloy within a wide range of applications in industry, military technologies, and health care. Although it contains half of the Nickel atoms, surprisingly, the magnetic properties of Nitinol are only rarely discussed in the literature. Magnetic properties of NiTi usually only fragmentary mentioned as related to the subject characteristic and as a general subject have been found just in several papers[66]–[69]. We summarize in the following section barely all the publications and pieces of work that we were able to collect.

The first work we have found has been published in 1967 in Ref. [70]. Wasilewski et al. listed magnetic susceptibility as one of the properties affected by martensite transformation as well as elastic modulus or electrical resistivity.

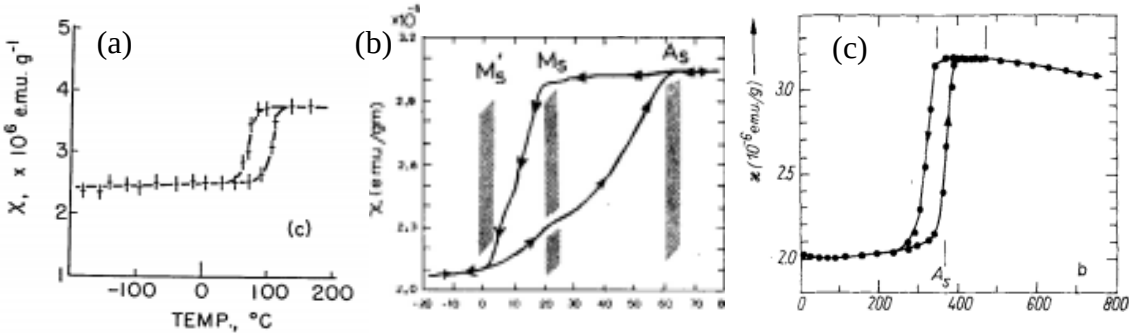

Figure 7. Magnetic susceptibility as a function of temperature (a) for NiTi with 50.6% Ti in [70], (b) for NiTi rod [71] and (c) for near-equiatomic NiTi sample[72].

In 1968 were published an article of Wang et al. [71] where the martensite transformation model was proposed based on the idea of electron transition from more covalent state in austenite to more conduction state in martensite by means of s-band shift and change of the d-band width, while the density of states doesn't change. However, future ab-initio density of states (DOS) calculations didn't confirm this model[73], [74]. Magnetic susceptibility χ, measured by Ainsworth automatic vacuum chemical balance, and electrical resistivity were used to confirm the model. Figure 7b shows their experimental χ values as a function of temperature. Surprisingly, hysteresis has a triangular shape, that is no features of the beginning of the transformation to the austenite phase. The values of magnetic susceptibility are found to be equal to $2.1 \cdot 10^{-6}$ emu/g in martensite and $3 \cdot 10^{-6}$ emu/g in austenite. Both austenite and martensite susceptibilities are stated to be independent of temperature. Consequently, the origin of magnetic susceptibility is expected to be of Pauli paramagnetism. This assumption was yet developed in [66] considering the electronic density of states. According to this model, martensite transformation in NiTi is accompanied by 1.1eV Fermi energy shift with no change in the shape of the density of states. Later DOS calculation [75], [76] showed that it is not a case, however, the overall shape is similar.

Shabalovskaya et al. in [77] and [72] have shown rectangular thermal hysteresis of magnetic susceptibility in equiatomic and Ni-rich NiTi alloy, while in Ti-rich alloy hysteresis is suppressed and transition occurs at the same points in both ways of transition. Within susceptibility versus temperature plot in Figure 7(c), a negative slope is observed in the austenite phase whereas a positive slope is found in martensite. In [72] electron related properties of NiTi in the region of martensite transformation are broadly discussed. In particular X-ray photoemission spectra are compared with magnetic and electrical resistivity features. It is assumed that the positive slope of susceptibility in austenite and negative in martensite phases originates from a minimum and maximum of DOS at E_f, respectively. However this assumption is doubted by DOS calculations and the authors suppose that the extreme sensitivity of NiTi to doping or treatment and specific behavior of the magnetic susceptibility are resulted from the peculiarities of NiTi electron system. Such peculiarities as peak in the DOS of width kT, the degenerate state at the Fermi level, disappearing indirect gaps in the band structure, negligible small parts of the Fermi surface and nesting surfaces.

In the paper of Bihlmayer et al. [74] the authors referred to the paper of Lashkarev et al. from 1992 (was not possible to found) where the slopes were not confirmed and as

the reason of lower magnetic susceptibility proposed the higher Debye temperature at martensite phase. However, the same group of authors has shown in [67] that the slope and the shape of magnetic susceptibility versus temperature characteristic depends on treatments of NiTi powder used in the experiment (Figure 8). The NiTi powder containing up to 0.6 wt. % oxygen was pressed, sintered, fired, annealed and oxidized. The signs of Curie paramagnetism were found and attributed to Ti_2Ni precipitations, resulted from the alloy oxidation. The authors also mentioned that the deformation of porous NiTi increases its magnetic susceptibility in both phases. The impact of NiTi structure on NiTi susceptibility is also confirmed by the susceptibility variation upon B2-R-B19' transformation in Ti-48.0Ni-1.7Fe(at%) [75].

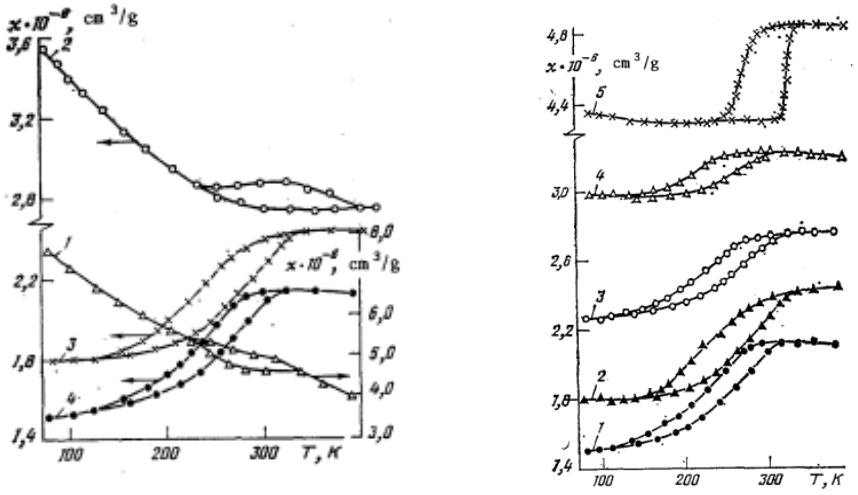

Figure 8. Magnetic susceptibility temperature dependence of NiTi with different treatment. From reference [67]. (a) 1) initial powder, 2) 45% porosity pressing, 3) 41% porosity specimen sintered at 1423K, 4)powder fired at 1423K; (b) Magnetic susceptibility temperature dependence of NiTi powder fired in vacuum at 1423K for 30min (1), 41% porosity specimens sintered at 1423K for 1hour(2)then compressively deformed at 320 MPa (4) and then annealed at 1423K for 30min(3), NiTi obtained from the fused state(5).

More recently, we could find 2 publications related to Magnetic resonance imaging (MRI) where NiTi, NiTiPt and NiTiEr compatibility with MRI is tested [68],[69]. Magnetic signal of hot-rolled and extruded NiTi was demonstrated to be the same, however the authors assumed that NiTi was in the mixture of phases, and crystal structure was not characterized.

Fukuda et al. [75] suggested that the lowering of the density of states at Fermi energy as transformation proceeds from austenite to martensite phases may explain respectively magnetic susceptibility lowering. However, the system to which magnetic susceptibility was referred is Ti-48.0Ni-1.7Fe(at%). Iron-doped NiTi was also studied by Choi et al.[78] where they demonstrated temperature dependence of magnetic susceptibility and correspondence of its transitions to transformation temperatures obtained with resistivity measuring technique. Interestingly, hysteresis disappears when Fe composition increases from 2 to 4%.

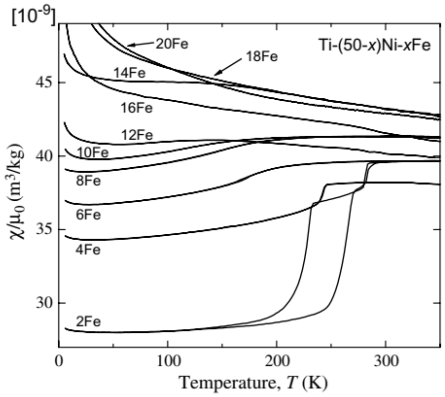

Figure 9. Temperature dependence of magnetic susceptibility of Ti-(50-x)Ni-xFe alloys from [78].

As a summary, it was shown that NiTi phase transition is reflected in its magnetic response. However, there are only a few studies where the magnetism of NiTi is the main subject of interest and its origin is discussed. In the mentioned papers, usually the crystal structure and morphology of the samples were not studied although several different metallurgical treatments and dopings were used. So, it makes difficult to compare these results in order to find common tendencies or contradictions. Concerning the physical origin of paramagnetism, it was mainly accepted to be the Pauli paramagnetism. However, there is no studies where this assumption was quantitatively verified. There is a lack of studies were both structure and magnetic features of NiTi experimentally investigated along with ab-initio calculations in order to clarify the topic.

CHAPTER II. MAGNETISM AND CRYSTAL STRUCTURE OF SPUTTER-DEPOSITED NITI ALLOY

In the first part of the present chapter NiTi samples and their growth route are described, and the chemical composition is measured. Then the structure is characterized by means of X-ray diffraction and transmission electron microscopy. In the second part, magnetic susceptibility of NiTi is studied depending on its phase, structure, and temperature. The origin of paramagnetism in NiTi is examined by comparing experimental data with ab-initio calculations. Then the magnetometry probing capabilities of shape memory alloys transition temperature and stress state are demonstrated.

II.1. Growth and structural characterization of NiTi

II.1.1. Choice of the sample and its growth

All the experimental data presented in the present and next chapters are obtained on 20-micron thick NiTi free-standing samples grown by DC sputtering by Acquandas company.

Sputter-deposited NiTi based shape memory alloys have attracted attention along with growing demand for microactuators. Among the main reasons for the interest is work output per unit volume which is the larger than an output of other microactuators mechanisms[79]. Physical vapor deposition (PVD) enable to grow pure NiTi alloys with reliable and highly performing shape memory effect and pseudoelasticity as in conventional SMAs[2]. The significant aspect is that sputter deposition allows micropatterning manufacturing of SMAs[80], which allows overcoming some limitations of the conventional manufacturing processes[81]. PVD facilitates avoiding typical manufacturing processes as ingots melting, hot/cold rolling, forming, polishing, mechanical or laser shaping. It leads to a reduction or absence of inclusions, contaminations, microcracks. Therefore sputter-deposited NiTi shows better fatigue performance[2], mechanical and corrosion properties.

Additionally to the advantages stated above, our choice for sputtering NiTi film originally came from the lower surface roughness shown by these films compared to other techniques. Low surface roughness was necessary to maximize strain transfer from NiTi to a ferromagnetic layer deposited on top of it, as presented in Chapter IV. Nevertheless, the high NiTi purity and low defect density obtained by sputtering makes it also very interesting for studying of the intrinsic origin of NiTi magnetism, comparing to existing literature presented in the previous section. Finally, sputter-deposited NiTi films allow micropatterning manufacturing which can be required if it is implemented into an electrically connected device for instance [3].

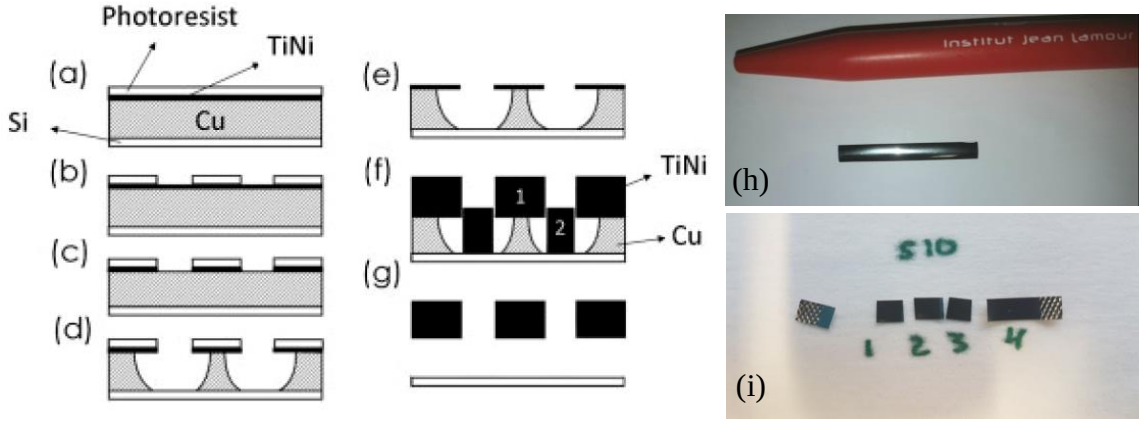

Figure 10. Schematic flow chart: (a) sputtering of Cu sacrificial layer and NiTi thin film followed by spin coating of the photoresist, (b) patterning of photoresist by means of UV lithography, (c) wet etching of TiNi thin film, (d) wet etching of Cu sacrificial layer, (e) removing of photoresist, (f) deposition of thick TiNi film, and (g) wet etching of remaining sacrificial layer.(a)-(g) from Ref. [80]; (h) and (i) are pictures of the final NiTi as-grown and cut (after tensile strain or not). The regular pen is nearby for size comparison.

Figure 10 shows the schematic flow chart of the fabrication route developed in this work as presented in Ref [80]. As the first step, a 10μm Cu layer is deposited on a Si wafer with the Cu acting as a sacrificial material for further processing. This is followed by the deposition of a NiTi thin film with 1.5μm thickness, which is much thinner than the required total NiTi film thickness (20μm). NiTi alloy growth is operated with an Alcatel 450 magnetron sputtering system at a base pressure below 1×10^{-7}mbar with a deposition rate of 3.9nm/s. After the sputtering process, the wafer is spin-coated with a 2.3 mm thick photoresist AZ1518 (Figure 10a). The soft bake is performed on a hotplate at 105°C for 2 min followed by rehydration for another 2 min. UV lithography is applied as the second step using a Karl Suss mask aligner MJB4 in hard contact mode. A chromium covered quartz mask with a feature resolution of 500nm is used in soft contact. The exposure time is 2 s and the resist is developed using a AZ716 MIF solution for 1

min, forming the desired geometry (Figure 10b). The hard bake is performed at 120°C for 20 min. The third step consists of the wet etching of the 1.5μm NiTi thin film using a HF solution resulting in an etching rate of 0.6μm/min (Figure 10c). In the fourth step, the sacrificial layer is wet etched forming a mushroom-like structure (Figure 10d), due to the isotropic behavior of the wet etching process. As a selective etchant, a standard BASF Selectipur Chromium Etch (etching rate 0.8 μm/min) is used, which does not affect the NiTi thin film. As the fifth step, the photoresist is removed using acetone (Figure 10e). To achieve the required total NiTi film thickness, as the sixth step the corresponding NiTi thick film is now deposited on top of the structured NiTi thin film, using the same parameters as before. The mushroom like structure allows the growth of the film on top of the pre-structured mesh, avoiding any coalescence with the films growing in between the meshes (Figure 10f). As the final step the sacrificial layer is then completely wet etched using again the same BASF Selectipur Chromium Etch, which results in freestanding NiTi membrane (Figure 10g). In order to make magnetometry and tensile strain experiments easier, we chose sample dimensions as 0.5mm width and 30mm length as shown in Figure 10h. Later, the sample may be cut into pieces to be characterized (Figure 10i). In total 5 batches of samples were prepared by Acquandas at different moments during this study.

II.1.2. Composition and crystal structure of NiTi samples

Nominal concentration (in atomic percentage) of the NiTi sheets provided by Acquandas was 50.6 at% Ti / 49.4 at% Ni with a resolution of ± 0.5%. These values were obtained by Energy-dispersive X-ray spectroscopy (EDS). Nevertheless, because EDS measurements were not performed by Acquandas specifically on our samples, Christine Genderme from Institute Jean Lamour performed wavelength dispersive X-ray spectroscopy (WDS) using an electron probe microanalyzer (EPMA) in order to confirm the nominal values. Under a voltage of 20 kV, the probed volume is expected to be 1 μm^3 at the surface of the sample. One hundred measurements were performed over an area of 500 × 500 μm. The average concentration value (in atomic percentage) is found to be 52 at% Ti / 48 at% Ni with a resolution of ± 0.5%. We do not understand yet where this discrepancy comes from.

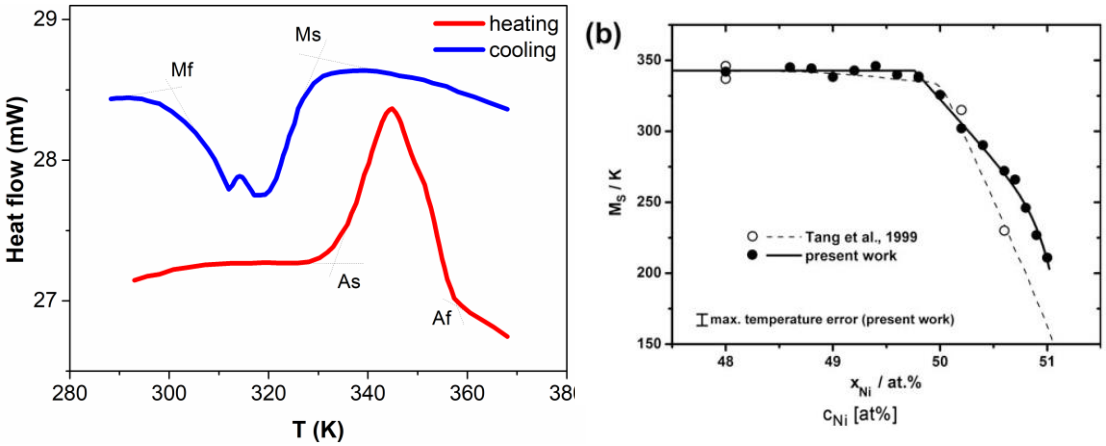

Figure 11. (a) Differential scanning calorimetry for our NiTi samples. (b) Start temperature for Martensite transition as function Ni concentration from Ref.[82]

In order to get further information about the concentration of our sample, we can look at the martensitic transformation. It is known that the transformation temperatures are sensitive to the ratio of Ni to Ti atoms. Figure 11(a) shows the results of differential scanning calorimetry measurement performed by Acquandas on the first batch of the samples that we received. Transition temperatures are as follows: A_f= 360K, A_s= 335K, M_s= 330K and M_f=305K. One can notice that the sample is completely in austenite above 360K and in martensite below 305K. Unfortunately, depending on the study we refer to, these values of transition temperatures could match with various concentrations between 49.8 to 52% of Ti [56],[82],[83]. The uncertainty in literature values originates from the subtle differences in preparation processes, differences in characterization methods, oxygen and carbon pick-up during melting, stress state, etc. Available literature on sputter deposited NiTi [79], [83],[84] doesn't clarify the situation since transformation temperatures significantly vary whether it is thin or bulk film, freestanding or constrained by its substrate[85].

Finally, the unique feature that is common to all the studies is that transformation temperatures are almost constant in the concentration range from 48 to 50 at% of Ti as shown in Figure 11b. Therefore, we did not investigate further the discrepancy between nominal and measured concentration.

X-ray diffraction and transmission electron microscopy measurements

The X-ray diffraction measurements (XRD) were performed with the valuable help of Pascal Boulet, the head of the skill center "X-Gamma" of Institute Jean Lamour. Except for low-temperature measurements, that were performed with the help of another member of "X-gamma" - Ghouti Medjahdi. The X-ray diffraction measurements presented in this section were conducted in order to study crystal structure, texture of the NiTi samples and to confirm transformation temperatures measured by the supplier. Bruker D8 Discover diffractometer at 1.7889 wavelengths provided by Co Kα source was used. Cycles of measurements were performed in Bragg-Brentano geometry at room temperature, below M_f, and then step-by-step up to 400K, above austenite finish A_f. During each XRD measurement temperature was maintained stable until heating/cooling to the next temperature. Heating was accomplished in-situ by means of the DHS 1100 oven. Heating/cooling experiments were performed at atmospheric pressure.

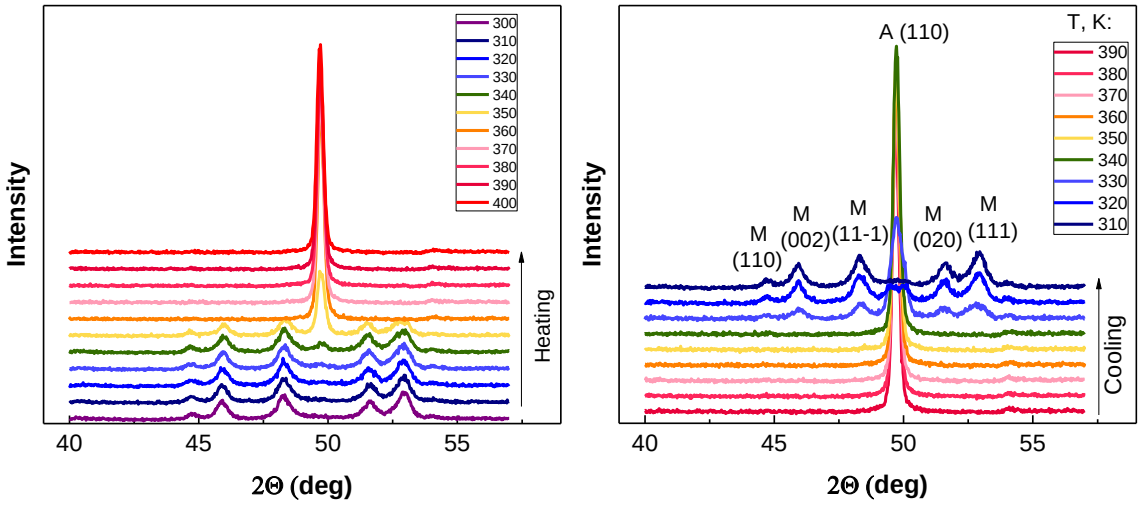

Figure 12. XRD of NiTi sample as a function of temperature. Stepwise measurements of diffraction patterns on heating(left) and on cooling(right) illustrate martensite transformation and its hysteretic shift in temperature between heating and cooling. "A" and "M" stand for austenite and martensite diffraction planes.

Measured XRD scans at the range of temperatures are presented in Figure 12. The diffraction patterns were analyzed in Diffrac.EVA software and compared with powder patterns of near-equiatomic NiTi alloy from the database. As expected, the reversible thermo-elastic martensitic transformation takes place. In low temperature martensitic phase sample possess B19' monoclinic structure that belongs to $P2_1/m$ space group (as in Figure 3). In austenite NiTi is in B2 cubic structure, PM-3M space group.

The fit of the XRD scans and adjusting of lattice constants in Diffrac.Eva results in: a =2.894 Å, b=4.115 Å, c=4.637 Å, and monoclinic angle β=97.41°. For cubic phase a= 3.015 Å. Found values are in agreement with various experimental data in the literature [51]. No signs of other then NiTi phases were not found.

It can be observed that during heating martensite grows into the cubic austenite phase on interval from 340 K to 360 K. However, during the specimen cooling transformation happens between 330 K and 310 K. Actual temperatures are 3K higher because of rounding from C° to K. These temperatures are in agreement with previous DCS measurement taking into account as high as 10K step in XRD experiment. As distinct from the regular NiTi, sputter Nitinol doesn't require hot- or cold-rolling work, as a result, in the martensite phase our samples are completely polycrystalline and its XRD pattern is similar to one from powder NiTi. While in regular Nitinol rolling induces preferential orientation of crystals.

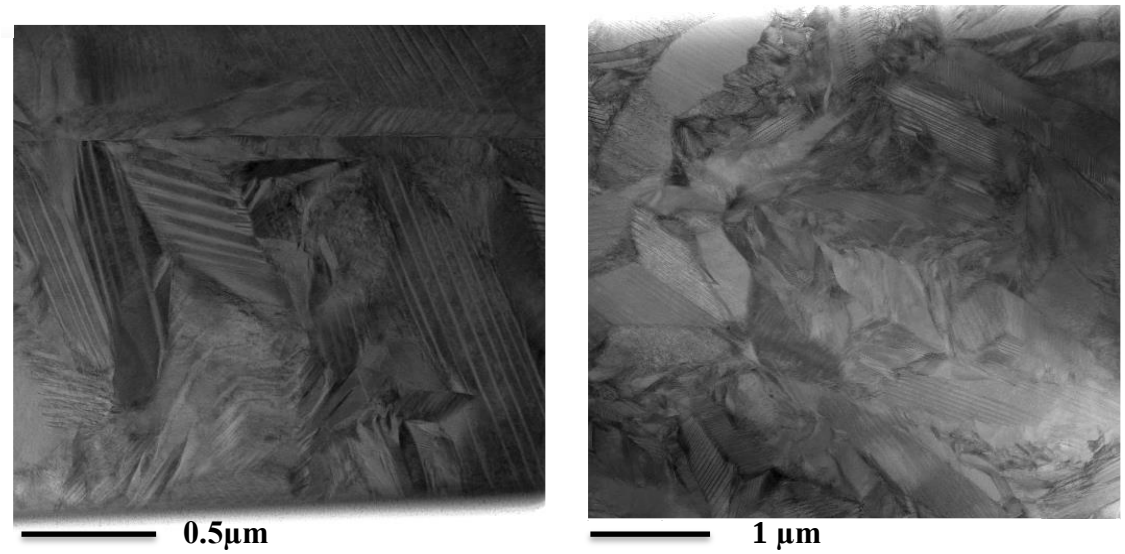

Figure 13. Bright field TEM micrograph.

Transmission electron microscopy (TEM) measurements have been done in competence center CC MEM of Institute Jean Lamour by Jaafar Ghanbaja, on JEOL ARM 200F cold FEG microscope dedicated for structural and chemical analysis at high resolution. Sylvie Migot prepared a thin cross-section cut of the sample by focused ion beam technique. Analysis of the sample at room temperature confirmed results about the crystal structure of martensite obtained by the XRD technique. Bright-field micrographs in Figure 13 show the grains in the range of 1 µm, where the twinned structure introduced in section I.2.2 is observed everywhere. The sample is polycrystalline, and any preferred orientation was not found. The dislocations were rarely but constantly encountered in

TEM images. The thin Ti-rich oxidized layer(~12nm) was found on the surface of NiTi (see Chapter IV).

From the point of view of magnetism related measurements, it was important to know that there is no ferromagnetic signal from nickel in the NiTi samples and check the presence of other phases. Ni and Ti sensitive X-ray mapping from EDS measurements in Figure 14 corresponds to the zones in Figure 13. Resolution of probe is 0.5nm but it is limited by image pixel size so in the figures below resolution is 7.8 nm. Measurement demonstrates the absence of Ni or Ti segregations and homogeneity of the sample. The composition dispersion in various local zones (<100nm) doesn't exceed ±2% of Ni or Ti. The latter suggests the absence of Ti_2Ni phase in the bulk of our samples, which may be encountered in Ti-rich samples[65].

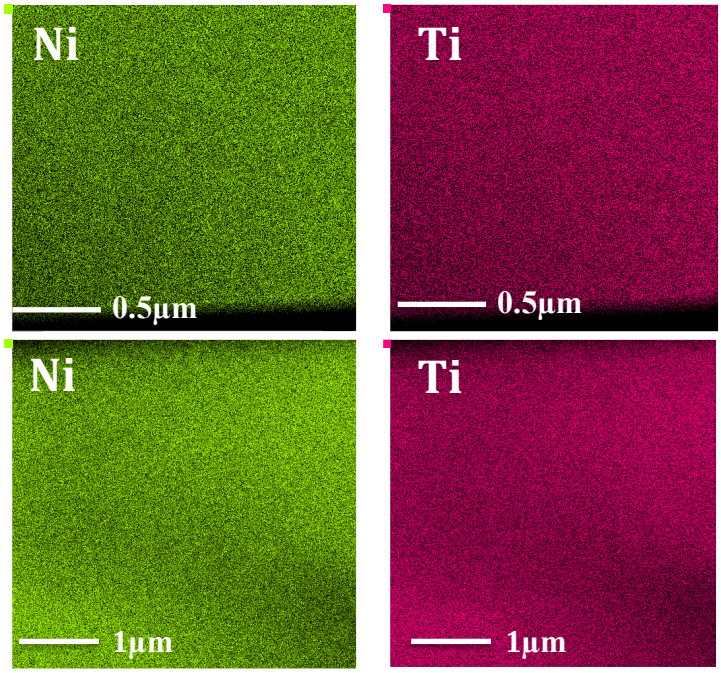

Figure 14. X mapping of Nitinol sections from Figure 13, showing the absence of Ni or Ti segregations.

In order to study the temperature dependence of NiTi crystal structure on temperature, a set of XRD measurements between ambient temperature and 123K were performed on the X'Pert Pro MPD diffractometer working on K_a(Cu) wavelength in Bragg-Brentano geometry. The results presented in Figure 15(a) demonstrate a slight but monotonical shift of the diffraction peaks on cooling, which signifies the lattice parameters change. The tendencies of peak shifting are summarized in Figure 15(b), where the changes of lattice parameters relatively to 311K are plotted as a function of temperature. The change of monoclinic angle is the most pronounced, β increases on cooling, as well as *c*, while *b* decreases. However, an increase in parameter *a* is barely

significant. Such behavior of NiTi at low temperature is in agreement with experiments [51] and theory [86], however the rate of change is significantly lower than in found references.

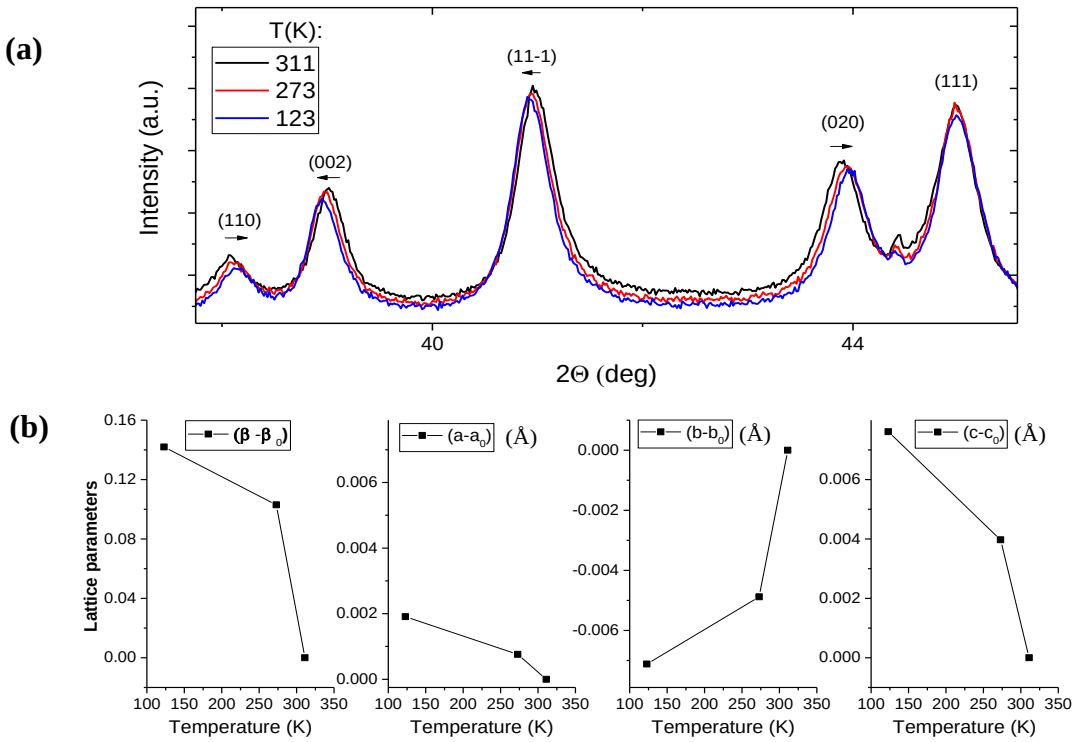

Figure 15. (a) XRD of non-deformed NiTi martensite at low temperatures, different theta degrees are because of Cu X-ray source. (b) Lattice parameters extracted from measurements in (a) as a function of temperature.

Series of XRD measurements in high temperature were done as well. Resulted lattice parameter *a* of austenite BCC structure is about 3.016A and the linear coefficient of thermal expansion extracted from the data is 1.15, which is coherent with literature.

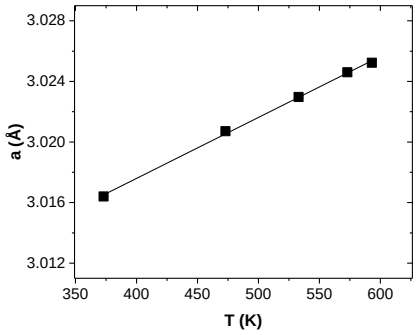

Figure 16. Lattice parameter a of BCC austenite structure as a function of temperature.

II.2. **Magnetism investigation in NiTi alloy**

After the structure and composition of the NiTi were characterized, in the following section NiTi will be investigated by magnetometry techniques. Its magnetic response will be studied depending on magnetic field, structure, temperature. The origin of NiTi paramagnetism will be examined.

II.2.1. Measurement techniques and general magnetic characteristics

In the following section magnetometry techniques and their limitations in terms of the current study are discussed. The main magnetic characteristics of NiTi, as magnetization versus magnetic field and versus temperature are presented, and their results compared with literature.

Most of the magnetic moment measurements in this chapter have been performed by vibrating sample magnetometers (VSM). The principle behind this technique is Faraday's law of induction: $V = d\Phi/dt$. That is a sample vibrates inside a coil and induces the voltage V in a coil by changing the flux Φ across it as a function of time. Two main parameters characterizing sample's vibration is amplitude A and frequency ω. Substituting these terms in Faraday's law of induction gives the general equation for output the voltage of magnetometer coil: $V = -(d\Phi/dz)\, A\omega \cos(\omega t)$, where $d\Phi/dz$ is the spatial flux gradient in the direction of vibration **z**. This term depends on the sample's moment which is the measured quantity, flux coupling to the coil or "coil geometry factor" and sample dimensions or sample geometry factor. The latter term should be considered because it may have significant influence the measured signal. For our sample geometry factor variates as a function of sample dimensions in range from 0.97 to 1.035.

Some measurements of the magnetic moment versus field M(H) and some moment versus temperature M(T) measurements were performed with Physical Property Measurement System (PPMS) with VSM option from Quantum Design (QD). However, this tool at IJL is limited to 400K. Magnetic measurements as a function of temperature were performed by means of Superconducting Quantum Interference Device (SQUID) magnetometer. This device allows reaching 1000 K with Joule heater in oven mode. SQUID magnetometer also works on the basis of Faraday's law. The sample is moving

inside two parallel Josephson junctions, which consists of electrical superconducting coils, separated by a thin insulating layer. In this case, magnetic flux itself generates a signal. More detailed information about SQUID can be found in Ref. [87]. Magnetic moment measurement resolution of QD SQUID is about 10^{-8} kA.m^2 (= 10^{-8} emu) as compared with 5.10^{-7} kA.m^2 in the case of PPMS-VSM. Both resolutions are perfectly fine with our 20 μm thick NiTi membranes which provide up 10^{-4} signal for few tesla (see Figure 18(b). Note that the SQUID at IJL is also equipped with a VSM option whose vibration at 17Hz is used as in a regular VSM to filter out noise using lock-in modulation. It mostly allows to accelerate the measurements. PPMS-VSM, resp. SQUID-VSM, is equipped with superconducting coils that produce magnetic field up to 9 T, resp. 7 T.

One of the main limitations in PPMS-VSM and SQUID magnetometers is that apart from the sample, magnetometers measure everything inside the detector coils. Usually, it may be a substrate, sample holder, contaminants trapped in the chamber. Moreover, any irregularities like defects, scratches in quartz rod or dust in mounting tape or even inhomogeneities in its composition may bring some false positive moments. Partially these contributions from sample holder and mounting tape or foil normally can be subtracted by measuring background signal without the sample. Also, some tool- or measurement-related problems have been observed. For example, superconducting coils used in PPMS VSM and SQUID are able to trap magnetic flux. Thus, the real field inside the coil is the field that corresponds to applied current + trapped flux, and it cannot be measured because there is no probe of magnetic field in the chamber. The trapped flux problem can be solved by magnetic field ramping from +/-1 T down to 0T. Overall, we found that background is never reproducible from one measurement to another. Moreover, background amplitude is always of the order of a few percent and not higher than 8% of effective magnetic signal. Example of the M(T) plot before and after background deduction is presented in Figure 18. Consequently, and taking into account that in our work mainly relative change of susceptibility are discussed, we decided to neglect background subtraction in each measurement and include it in error bars when absolute values are discussed.

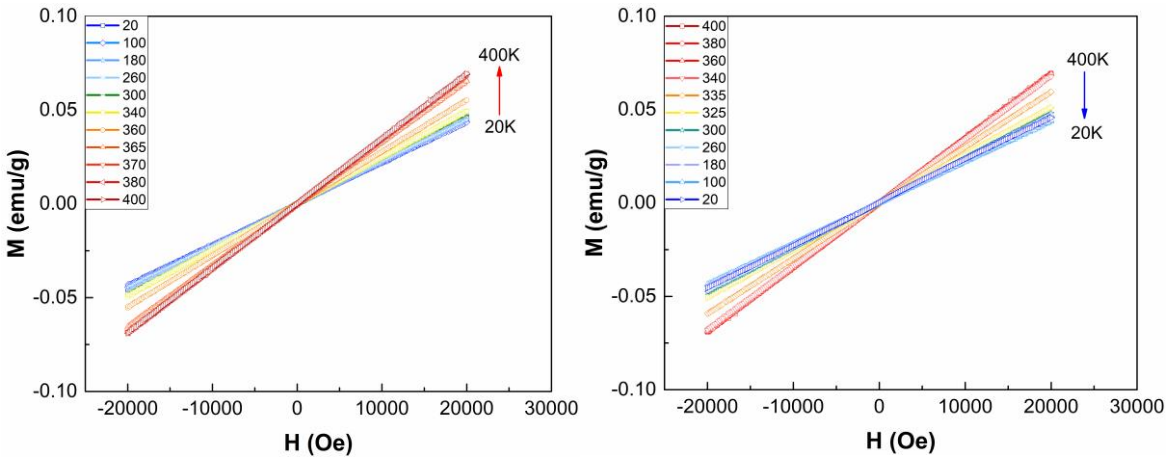

Figure 17. Magnetization versus applied magnetic field loops from 20K to 400K and from 400K to 20K.

Figure 17 shows M(H) signal of NiTi for various temperatures between 20K and 400K. Background subtraction performed for this measurement permitted to remove the low field hysteresis and to reveal pure paramagnetic signal, which is demonstrated by the positive linear M(H) dependence. The slope of M(H) loop is a magnetic susceptibility value: $\chi = {}^{M}/_{H}$. In the following, this parameter will be broadly used in this work as a universal characteristic of magnetic material convenient for comparison of different samples. Units are $\mathrm{emu}/(\mathrm{g} \cdot \mathrm{Oe})$. The sample mass is measured with a precision balance.

The slopes of M(H) loops change with temperature. In Figure 18(a) M(H) slopes are plotted, successively extracted from M(H) measurements as a function of temperature. There is a hysteretic behavior in temperature in the range between 280K and 380 K. This range corresponds to the martensite transformation in our NiTi samples as identified by DSC in Figure 11 and by XRD on Figure 12. Characteristic temperatures A_s, A_f, M_s, and M_f are in agreement with the values extracted by DSC and XRD within a given step of the measurements. It is to be noted that the same result can be obtained in measuring moment as a function of temperature at a fixed magnetic field. An example is shown in Figure 18(b). M(T) procedure under the constant field allows to get a better view of the transition temperature with more points while accelerating the measurements.

Mass magnetic susceptibility extracted in this case is $\chi_m = 2.44 \times 10^{-6}$ $\mathrm{emu}/(\mathrm{g} \cdot \mathrm{Oe})$ in martensite and $\chi_a = 3.46 \times 10^{-6}\,\mathrm{emu}/(\mathrm{g} \cdot \mathrm{Oe})$ in austenite phase. Evaluations of magnetic susceptibility from numerous magnetic measurements that have been done in this study usually give the χ_m values between 2×10^{-6} and $2.4 \times 10^{-6}\,\mathrm{emu}/(\mathrm{g} \cdot \mathrm{Oe})$ and χ_a between 3×10^{-6} and $3.4 \times 10^{-6}\,\mathrm{emu}/(\mathrm{g} \cdot \mathrm{Oe})$. The values include measurements done in different tools, for samples with different shape, and from different deposition batches but, as always in this work, for the same

composition. Despite of given dispersion of susceptibility, the difference between χ_m and χ_a values (for the stress-free sample) is quite stable from one to another measurement and is equal to $(\chi_a - \chi_m) = 1 \times 10^{-6} \pm 0.08 \times 10^{-6}\ \mathrm{emu}/(\mathrm{g} \cdot \mathrm{Oe})$. Error here includes experimental variation of measured quantities and sample's geometry factor.

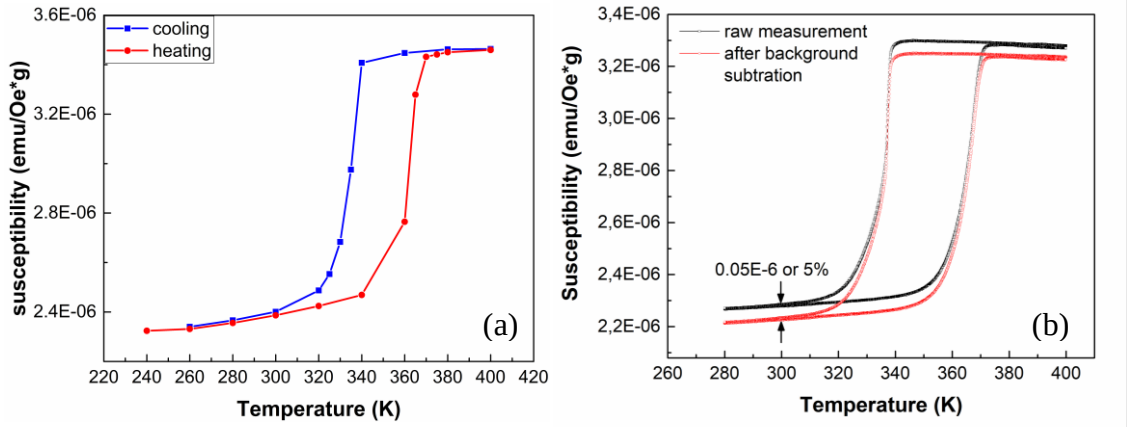

Figure 18. (a) Magnetic susceptibility from M(H) slopes as a function of temperature. (b) Typical M(T) under 1T with and without background

Overall, our values are similar to those in commercial specifications and previously discussed scientific papers (see I.2.5): $2.4 - 2.5 \times 10^{-6}$ and $3.7 - 3.8 \times 10^{-6}\ \mathrm{emu}/(\mathrm{g} \cdot \mathrm{Oe})$ [88],[89] or $3 \times 10^{-6}\ \mathrm{emu}/(\mathrm{g} \cdot \mathrm{Oe})$ [90], $2 - 2.1 \times 10^{-6}$ and 3.1×10^{-6} [71],[72] for NiTi sheets and wires. But the studied samples were mostly grown by melting processes and subsequent metallurgical procedures (annealing, hot/cold rolling, etc.) and their structural features are not described enough to directly compare them with our samples.

In this subsection, magnetometry techniques were described and their contributions to the background are investigated. The pure paramagnetic behavior of NiTi is demonstrated. Average magnetic susceptibility is 2.2×10^{-6} in martensite phase and 3.2×10^{-6} in austenite phase. Though the absolute values fluctuate depending on background contribution, magnetization versus temperature loop of NiTi is shown to be reproducible in defined limits, its amplitude is $1 \times 10^{-6} \pm 0.08 \times 10^{-6}\ \mathrm{emu}/(\mathrm{g} \cdot \mathrm{Oe})$.

II.2.2. Magnetic field and thermal cycling influence on MT.

As it was previously shown, magnetization measurement of NiTi alloy when heated reflects the course of martensite transformation. Consequently, the question is

rising: does magnetic field have an influence on phase transformation in this alloy? It is known that magnetic field affects both martensite transformation[91] and also solid-solid diffusional transformations[92] in different ferrous alloys, steels or metamagnetic shape memory alloys[93]. Materials, exhibiting such properties, are ferromagnetic in both martensite and austenite phases or in just austenite phase, while paramagnetic in martensite[94]. Because of the Zeeman energy gain from the applied magnetic field, transformation temperatures can shift to favor more magnetic phase. However, the studied NiTi shape memory alloy is paramagnetic in both phases, as it was shown in previous section. Nevertheless, austenite and martensite magnetizations are though weak, but different, so the effect cannot be excluded. Thus, several experiments with different applied magnetic fields from lowest to highest possible were performed.

Before conducting such measurement, the effect of thermal cycling on stabilization of phase transformation should be considered. It has been observed in numerous studies that thermal cycling changes mechanical properties and gradually reduces transformation temperatures of martensite transformation in NiTi systems[95], [96]. According to Miyazaki et al.[97] the main reason of the effect is a stress field introduced by dislocations appearing on thermal cycling.

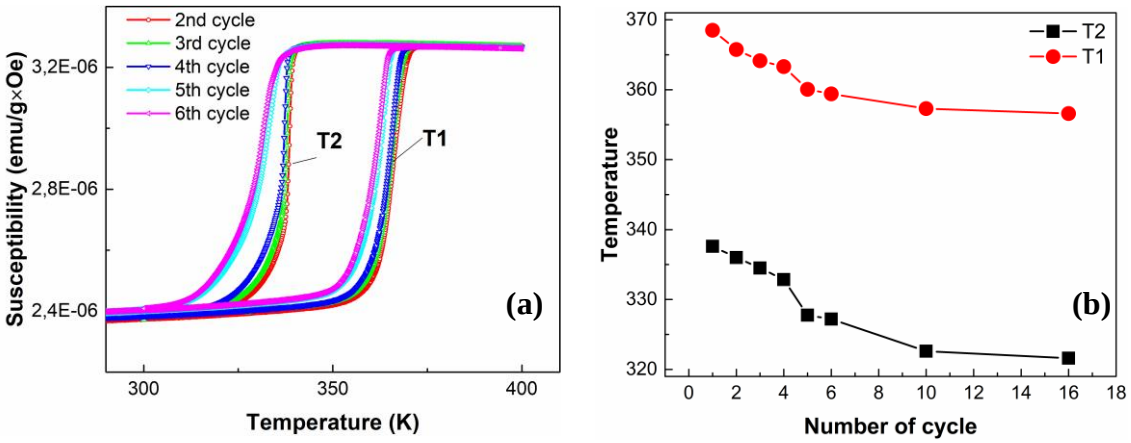

Figure 19. Effect of thermal cycling on transformation temperatures: (a) M(T) measurements of the V1_3 NiTi sample; (b) characteristic transformation temperatures as a function of cycle number; data acquired from V1_3 and V2 NiTi samples, presented on Figure 20.

The sequence of magnetization measurements of the NiTi specimen at constant magnetic field (20kOe) and heating/cooling rate (2K/min) was performed (see Figure 19). After 5th cycle transformation temperatures are relatively stabilized to have less than 1K shift between two consecutive loops. The shape of hysteresis stabilizes and becomes

wider after the first few cycles, while transition regions become smoother and more extended in temperature. In Figure 19(b) the effect of thermal cycling is summarized, where *T1=(As+Af)/2* and *T2=(Ms+Mf)/2*. The temperature shift is larger for transformation back to martensite, which results in the broadening of thermal hysteresis. However, the width *ΔT=(T1-T2)* is 31K at the 1st cycle, 32K at 6th and 35K at the 16th cycle, which makes it acceptably reproducible in known limits.

According to previous results, sample was cycled 10 times between 270K and 400K forth and back, in prior to check the field influence on martensite transformation. Hereafter one thermal cycle means full transformation from martensite to austenite and back to martensite. M(T) measurements in Figure 20 demonstrate that transformation behavior is not affected by magnetic field, at least below 70kG. T1 and T2 temperatures don't change in the limit of ±1K. However, the slope in the upper and lower parts of the loop changes significantly. This is a result of background contribution, that rises at low fields, as well as false moments described at the beginning of the section II.2.1. It was found that usually it is not constant in temperature (except rare cases as in Figure 20(b)) and also hysteretic and not reproducible well enough. It should be mentioned that discussed measurement reveals only the absence of field influence on transformation temperatures, but it doesn't mean that there is no influence, for instance, on preferred variants formation in NiTi.

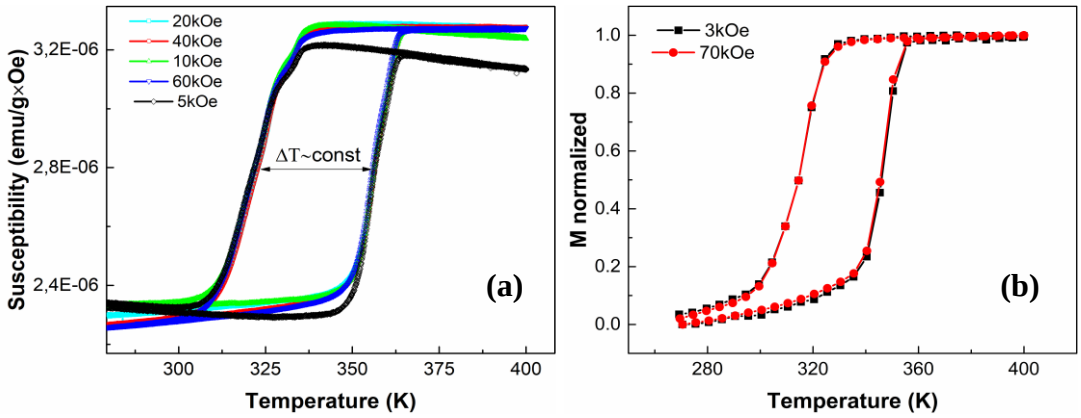

Figure 20. M(T) measurements at different applied magnetic fields(a). Normalized M(T) loops at 3kOe and 7kOe (b).

To ensure that a difference does not occur at lower fields than 3kOe, a set of magnetic measurements was done at low H fields (Figure 21). It is noteworthy that transformation was clearly seen at as low as 50 Oe magnetic fields, only the smoothing procedure was applied to reduce the noise in the raw signal. Figure 21(b) summarizes the

problem of low field measurement mentioned before, we may see that slope decreases with field increasing and became stable after 10-20kOe. The thermal hysteresis width changes only slightly in range of few Kelvin, this change presumably is not dependent on field and can be accounted for differences in loop's shapes and measurement error.

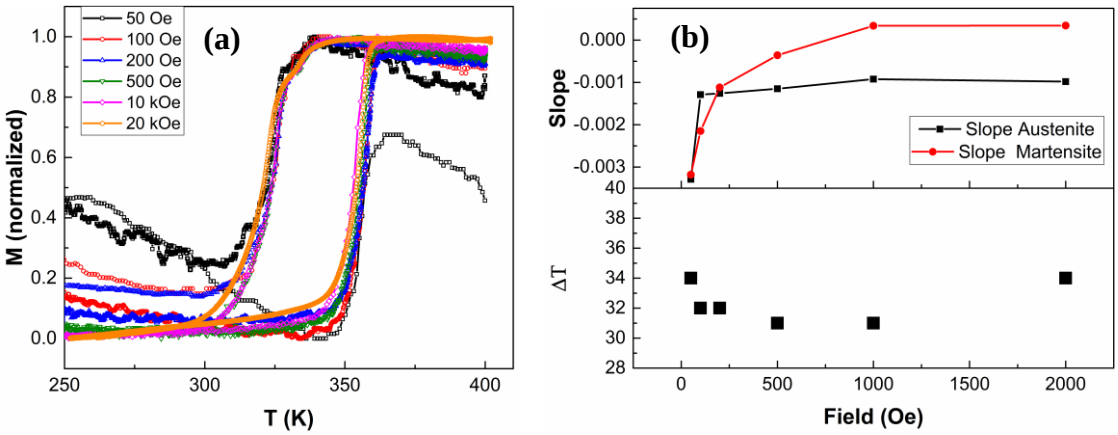

Figure 21. M(T) measurements at the range of weak magnetic fields (a). The slopes of corresponding M(T) loops and (T1-T2) thermal hysteresis width as a function of field (b).

In this section, NiTi was thermally cycled and the effect of M(T) hysteresis stabilization is observed. Stabilization consists in the lowering of transformation temperatures and in the changes of its shape. No noticeable influence of an external magnetic field on neither transformation temperatures, nor M(T) amplitude was found. Magnetic field strength of 2T was selected as a large enough to overcome background and false signal contributions and will be used for M(T) measurements.

II.2.3. Origin of paramagnetism of NiTi SMA

In order to examine the nature of observed paramagnetism in NiTi, there is the two main sources of paramagnetism are usually considered: localized electrons (Curie paramagnetism) and nearly free electrons at Fermi energy (Pauli paramagnetism).

Paramagnetism coming from atoms is usually described by Langevin model. In this case magnetic susceptibility of the material results from localized unpaired electron moments. The net atomic moment ***m*** consists of spin and orbital components and the moments are not interacting. Accepting condition $\mu_0 mH/k_B T \ll 1$, which is usually the case, magnetic susceptibility can be expressed by Curie law: $\chi = \frac{N\,\mu_0 \mathbf{m^2}}{3k_B T} = \frac{C}{T}$. Where N is a number of moments per unit volume and C is Curie constant. This law shows that

susceptibility increases when temperature decreases. Previous magnetic measurements of NiTi have shown that temperature dependence is very weak (far away from 1/T) and is opposite in two phases. Magnetic susceptibility of NiTi is in order of magnitude smaller than typical Curie paramagnet. Also, our ab-initio calculations showed NiTi remanent atomic magnetic moments at 0K are equal to 0, which means that localized electrons don't contribute to NiTi paramagnetism.

Often paramagnetism cannot be explained by the local moments model above and it is usually true for 3d transition elements. So, in this case paramagnetism comes from outer, nearly-free electrons. Because of Pauli exclusion principle, electron states needed for reorientation in Langevin model are occupied. Only the electrons with an energy k_BT of the Fermi level have a chance to reorient [98]. Considering the parabolic distribution of nearly free electrons, applying a magnetic field breaks equilibrium and it leads to the energy difference between spin parallel and antiparallel to the field $E = 2\mu_B B$.

Resulted susceptibility is linearly proportional to the DOS at Fermi energy:

$$\chi_{pauli} = \mu_B^2 D(Ef) \quad (3)$$

Pauli susceptibility is small relatively to Curie and is comparable with diamagnetic susceptibility of free electrons (Landau diamagnetism) [99]: $\chi_{diam} \approx \frac{1}{3}\chi_{pauli}$, which should be taken into account: $\chi = \frac{2}{3}\mu_B^2 D(Ef)$ (4)

In order to examine assumption about Pauli origin of paramagnetism in NiTi, ab-initio calculations of the electronic density of states (DOS) were done, using lattice parameters extracted from XRD measurement in the section II.1.2: a =2.894Å, b=4.115Å, c=4.637Å and β=97.41°. As well as the atomic positions used in the calculations are for Ni: x=0.0372, y=1/4, z=0.1752 and for Ti : x = 0.4176, y =1/4 , z=0.7164.

Calculations based on the Density Functional Theory (DFT) were performed by Emilie Gaudry from Institute Jean Lamour with the Vienna ab initio Simulation Package (VASP)[100]–[102]. The interactions between the valence electrons and the ionic core is described using the projector-augmented wave (PAW) method and the calculations are performed with the generalized gradient approximation (GGA-PBE)[103]–[105]. Spin polarization is considered. A plane wave basis set for electron wave functions with cutoff energy of 500 eV is used. Integrations in the Brillouin zone are performed using a k-grid generated according to the Monkhorst-Pack scheme: 33x23x23 for the martensite NiTi.

Density of states calculations were performed with the tetrahedron method for Brillouin-zone integrations[106].

Indeed, as it was pointed out in some studies mentioned in I.2.5, DOS in the vicinity of Fermi energy is higher in austenite phase than in martensite, so it should be responsible for the corresponding relation of magnetic susceptibilities. The overall shape of DOS is similar to other calculations found in literature[74], [75], [107], [108], where it consists of two groups of peaks and the valley between them. Fermi energy level stands close to the right group of the peaks in both phases. To look closer on the DOS profile around Fermi energy E_f, the calculations of the narrow range of energies but with the small step were done. In the magnified region of these calculations in Figure 22(b) we see that in the austenite phase E_f lies in the plateau, surrounded by two local hills. However, in the martensite phase, DOS lies in the deep and narrow hollow. The hollow suggests that any subtle changes in the lattice may lead to the change in the density of states at the Fermi level $D(E_f)$ and to change its properties. Total DOS values at Fermi energy for spin up+spin down extracted from Figure 22 in martensite phase is $D(E_f)_M = 0.71\ states/(eV \cdot atom)$ and in austenite $D(E_f)_A = 1.38\ states/(eV \cdot atom)$.These values are close to some other quantities found in literature, as to aprox. 0.8 and 1.3 in [73] or 0.75 and 1.45 calculated by Kulkova et al.[76], 0.69 in martensite phase only by Kellou [108], while Fukuda results[75] and Bihlmayer[74] are less consistent with the others: aprox. 1 and 1.5 $states/(eV \cdot atom)$. Density of states in all the cases were calculated for equiatomic NiTi and the discrepancies are mostly may be accounted to the used lattice parameters, atomic positions and level of resolution in energy.

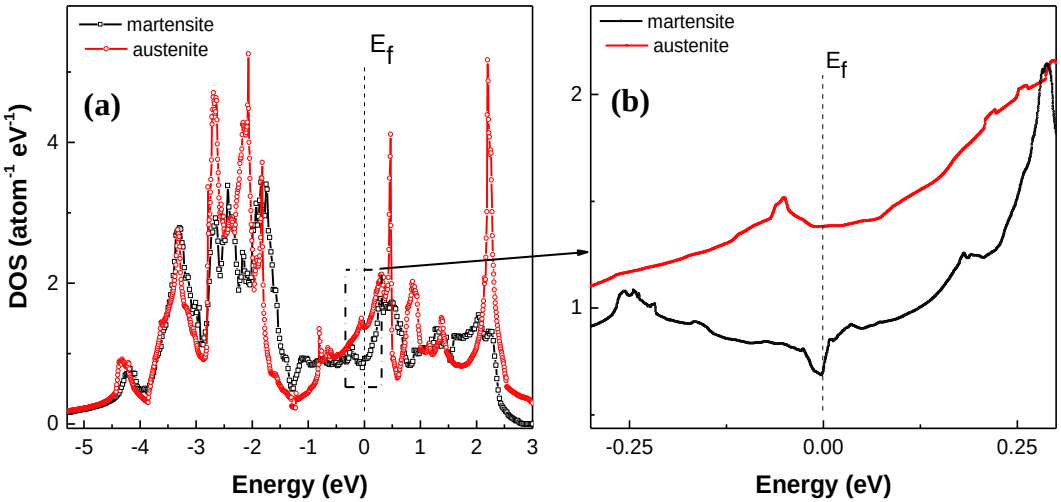

Figure 22. Density of states per atom calculated on the base of lattice parameters of the studied NiTi sample for one spin direction(a) and the magnified region around Fermi level of the DOS recalculated with a small step(b).

Typical M(T) characteristic of studied NiTi samples in broad range of temperatures in Figure 23 shows positive slope in martensite phase and negative in austenite phase, the signs of the slopes confirm the results of Shabalovskaya et al. [72], [77], however in austenite the slope is smaller and in martensite is much larger. The results of Brodovoi et al.[67] shown in section I.2.5 demonstrated that the shape of M(T) curve, as well as the slopes, depend on the treatment history of an alloy, such as sintering, fusion, annealing or oxidation. It may explain the differences between M(T) characteristics reported by different groups, the weak Pauli paramagnetism can be easily affected by precipitations, especially if they possess much stronger Curie paramagnetism. Moreover, during the melting process, an alloy may be contaminated by impurities, in particular by ferromagnetic elements. From this perspective, we can assume that the NiTi alloy in this study is a purer alloy, so it is more suitable for study intrinsic properties of equiatomic NiTi, such as magnetism. As it was shown in section II.1.2, no other phases then NiTi have been found in sufficient quantity to be detected by means of XRD or TEM. Except for oxidized Ti-rich surface layer (as it will be shown in Chapter IV), however, its thickness in the range of 12 nm sounds insufficient to significantly contribute to magnetic signal of 20μm NiTi.

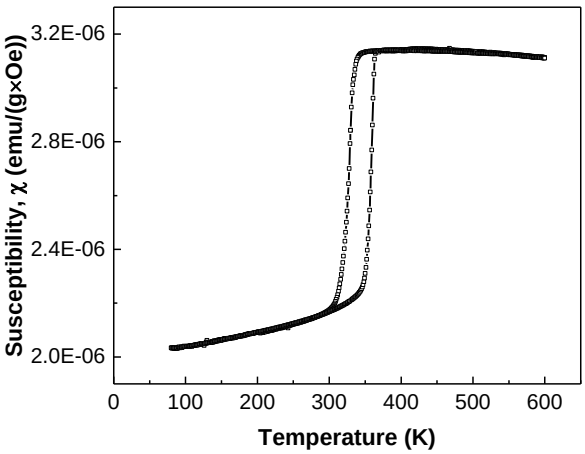

Figure 23. Typical measured M(T) dependence of NiTi in the wide region of temperatures.

Now we can discuss the values of magnetic susceptibility and its temperature dependence. Experimentally measured magnetic susceptibilities are in average $\chi_M = 2.2 \times 10^{-6}\ emu/(g \cdot Oe)$ in martensite phase and $\chi_A = 3.2 \times 10^{-6}\ emu/(g \cdot Oe)$ in high temperature austenite phase. If we compare the ratio of $D(E_f)$ of martensite to one in the austenite we get $\frac{D(E_f)_M}{D(E_f)_A} = 0.51$, while corresponding ratio of experimental susceptibilities is $\chi_M/\chi_A \approx 0.67$. It is noteworthy, that the above mentioned references

of DOS calculation mostly give $\frac{D(E_f)_M}{D(E_f)_A} \approx 0.63$, while only the article of Kulkova et al.[76] contains the ratio of ~0.5, like in our case. Using equation 4 resulted susceptibilities are χ_M=0.28·10^{-6} $emu/(g \cdot Oe)$ and χ_A=0.55·10^{-6} $emu/(g \cdot Oe)$. Finally, difference of experimental susceptibilities in both phases $\Delta\chi = (\chi_a - \chi_m) = 1 \pm 0.08 \times 10^{-6}$ is highly reproducible, but the corresponding difference of calculated values is ~0.3× 10^{-6}, that is in 3 times smaller. While the ratio of susceptibility looks reasonable to some extent, the absolute values are in 5.8 times smaller in austenite and in 7.8 times in martensite phase.

Common equation of Pauli paramagnetism, used in this section assumes non-interacting itinerant electrons. However electron-electron interactions may contribute as enhancement factor to Pauli susceptibility, as it is known in the case of Al, Cu or Ti [109]–[111]. According to it $\chi^*_{pauli} = \mu_B^2 D(E_f) \frac{1}{1-I*\eta}$, where η is the exchange enhancement parameter, also known as the Stoner exchange parameter[111], which depends on the strength of electron-electron interaction and density of states. From this point of view large exchange enhancement suggested in [66]. On the other hand large contribution from Ti_2Ni phase was assumed in [67], however in our case no other phases were found while magnetic susceptibility magnitude is similar to observed by the authors.

Certain many-body effects are included to the notion of effective mass in contrast to free electron mass considered in DOS calculations. Effective mass contribution to $D(E_f)^*$ may be experimentally estimated from low temperature electronic specific heat coefficient: $\gamma = \frac{2}{3}\pi^2 k_B^2 D(E_f)^*$. Unfortunately, we could not conduct specific heat measurements on our samples because of the not enough mass. The experimental values found in literature are 2.5-2.8 mJK^{-2}mol^{-1} [107], [112], [113]. Resulted $D(E_f)^*/D(E_f)$ ratio is ~1.6, it means we can expect increase in susceptibility for martensite phase, but not in 8 times. Need to notice that exchange enhancement depends only on spin, so it doesn't contribute to electronic specific heat coefficient. One of the possible explanations of larger experimental $D(E_f)^*$ can be found in ref. [107], where range of composition-dependent DOS calculations were performed for Ni-rich NiTi samples by Punniken et al.. It was pointed out that chemical disorder leads to smoothing and broadening of the DOS peaks, thus it may increase the $D(E_f)$, however this increase was assumed to be in ~1.3 times. The composition dependent change of the transformation temperatures was

accounted on the anomalies in the electron-phonon system. In [72] it was suggested that the phase transitions in NiTi and its high sensitivity to composition, and even temperature dependence of magnetic susceptibility are related to peculiarities of NiTi electronic structure, such as nesting Fermi surfaces and DOS peak near Fermi-level. Nesting Fermi surfaces related to the charge density fluctuation waves and the latter may be responsible for anomalies in magnetic susceptibility and its temperature dependence[110], for example in Pd. Further we will try to consider temperature contribution to DOS in order to quantitively estimate influence of the narrow hollow at Fermi level and to correlate magnetic susceptibility variation with temperature.

The influence of temperature on the density of states is rarely discussed in the literature. In [114] Kriessman and Callen reviewed temperature variations of Pauli magnetic susceptibility in several transition elements and proposed the method of its calculation based on simplified Fermi distribution. Two contributions as a function of temperature are considered: increasing of the width of $D(E_f)$ averaging interval and shift of the Fermi level. When applying this method [114], simply the average of the DOS from Figure 22 was taken at the $5.5k_BT$ interval around Fermi level, while the shift of the Fermi level was considered to be negligibly small at the temperatures of interest. This leads to increase of $D(E_f)$, especially in martensite phase because of the deep hollow at E_f. Applying $5.5k_BT$ averaging, $D(E_f)_M$ increases from 0.71 to 0.838 states/(Ev*atom) while $D(E_f)_A$ becomes 1.416 instead of 1.382. Clearly, such smoothing of the DOS distribution around E_f brings the ratio $\frac{D(E_f)_M}{D(E_f)_A}$ closer to 0.67 (expected from experimental susceptibility measurements): $\frac{D(E_f)_M}{D(E_f)_A} = 0.59$ for $5.5k_BT$ averaging instead of 0.51 in the "ground state" DOS.

Concerning experimental temperature dependence of magnetic susceptibility, intervals from 100K to 300 K in martensite and from 450K to 700K in austenite phase are considered. Experiments give us increase of martensite susceptibility in the range from 1.5 to 3.9 %/100K and decrease in austenite from -0.5 to -2 %/100K.

In austenite phase, usual DOS calculation made for the range of lattice parameter *a*, which was deduced from XRD in the section II.1.2. Resulted DOS variation demonstrates increase at Fermi level of $D(E_f)$=+0.6% per 100°K. Averaging of $5.5k_BT$ interval leads also to the rise of $D(E_f)$ to +0.28%/100°K. However, the variation of the $D(E_f)$ in austenite very close to zero. It is noteworthy then in experimental data slope of χ(T) becomes negative only after 450K, while from Af temperature to 450K it is nearly

constant. However, the reasons for different behavior after and before 450K are still unclear.

In martensite phase, averaging of ground state DOS from Figure 22 results in *+3.8%* per 100°K increase which is close to experimental <+2.2%> result. If consider lattice parameters change itself, density of states calculated for the set of lattice parameters deduced from XRD in section II.1.2 results in almost negligible variation, equal to *+0.15 %* per 100°. Fusion of these two approaches, that is averaging of DOS curves calculated from low temperature XRD measurements gives +7.5% per 100°.

D(E$_f$) renormalization reasons	$\boldsymbol{D(E_f)^*/D(E_f)}$
• Experimental $D(E_f)^*$ From $\gamma = \frac{2}{3}\pi^2 k_B^2 D(E_f)^*$:	Martensite: ×**1.6**
• Chemical disorder	Martensite: ×**1.3**
• Temperature contribution ➢ DOS "smearing" =>	Martensite: ×**1.2** Austenite: ×**1.02**

Table 1. Sugested renormalization factors $\boldsymbol{D(E_f)^*/D(E_f)}$ of the calculated density of states at Fermi energy.

Summarizing, magnetic susceptibility values and its temperature dependence was quantitively examined based on considerations that NiTi is Pauli paramagnetic material. Calculated magnetic susceptibility from the electronic density of states at Fermi energy is in 6-8 times smaller than experimentally measured one, while the ratio of experimental and theoretical values of magnetic susceptibilities in austenite and martensite phases was reasonably close, especially after temperature contribution considerations. The overall increase of calculated magnetic susceptibility in ~2.5 times was estimated from some of the factors that were not taken into account in the density of states calculation, and they are summarized in Table 1. Moreover there is a number of different peculiarities of electron system of NiTi[72], [107], that may contribute to the magnetic susceptibility. The presence of the deep narrow hollow makes the DOS related properties even more sensitive to any changes of the electronic structure. Also, exchange enhancement is expected to contribute significantly to observed discrepancy. Temperature variation of magnetic susceptibility in both phases was compared with possible temperature related DOS change. In martensite phase DOS increases in the same range as experimentally measured magnetic susceptibility (<+2.2%> per 100°K from experiment versus from

+0.15% to +7.5%, depending on approach). In austenite phase used method suggests DOS increase around +0.4%, however the experimentally observed variation in average results in -1.2%.

II.2.4. Relationships between crystal phase of NiTi and its magnetism.

As it was shown in previous sections, magnetization change of NiTi alloy is a manifestation of B2 to B19' crystal structure transition which is linked by the electron density of states to NiTi paramagnetism. Magnetization as a function of temperature measurements reveal transformation temperatures As, Af, Ms, and Mf in accordance with X-ray diffraction technique and differential scanning calorimetry. Therefore, magnetometry may be considered as an alternative probing and analyzing technique of martensite transformation, as recently was pointed out also in [115]. The aim of this section is to demonstrate a few more examples of magnetometry probing capabilities.

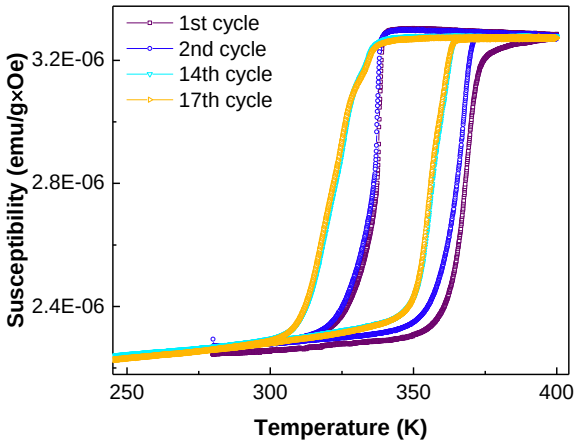

Figure 24. R-phase emergence during cycling and change of transformation path.

Figure 24 shows the case when R-phase appears after thermal cycling of the NiTi sample. The shape of transformation hysteresis changes between 1st, 2nd and 17th cycle. Difference between first and second cycle indicates that some stresses were present in the sample before measurement, this question will be discussed in the next chapter. Elongation of transformation path in 14th and 17th cycles probably comes from dislocation structure forming during thermal cycling, which constrain the transformation, as it was discussed in section I.2.4. The emergence of R-phase also should be related to the defects acquired during transformation, but R-phase doesn't emerge always on cycling, and exact reason remains uncertain. One batch of our samples was more predisposed to R-phase formation.

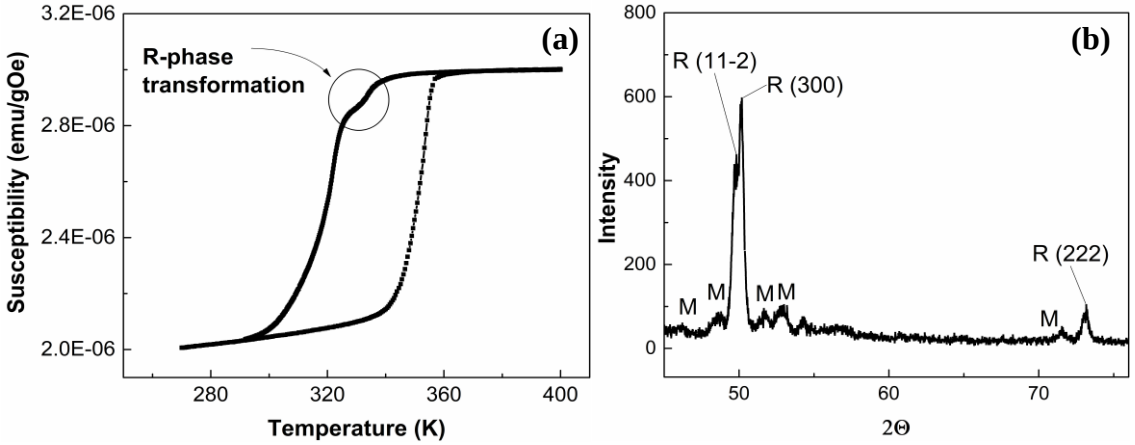

Figure 25. M(T) measurement showing transformation to intermediate R-phase on cooling (a) and corresponding XRD measurement at 325K confirming the presence of R-phase along with martensite peaks (designated by "M") growing (b).

As it was mentioned in section I.2.2, the intermediate R-phase may appear in MT from austenite phase. In Figure 25(a) R-phase transformation on cooling from B2 to B19' is shown. It looks like a small deepening in the region of martensite start transformation. To prove it XRD measurements demonstrated nearby have been done at 325K. So-called R-phase, P-3 space group, was found along with monoclinic phase rudiments. To examine again that DOS at Fermi energy is a source of magnetism in NiTi, the ratio of magnetization in R-phase to its value in martensite and austenite phases is compared to respective DOS ratios at Fermi energy. DOS values have been taken from Fukuda calculations[75]. These calculations are less consistent with ours calculations, but it is the only one where we found DOS of R-phase in NiTi, so the $D(E_f)$ of martensite and austenite phase are also taken from the same reference to preserve the ratio:

$$\frac{D(E_f)_R}{D(E_f)_{B2}} = \frac{9.3}{10.4} = 0.89 \text{ and } \frac{D(E_f)_{B19'}}{D(E_f)_R} = \frac{6.7}{9.3} = 0.72$$

Corresponding ratios of susceptibilities from our experiments show similar values:

$$\frac{\chi_R}{\chi_{B2}} = 0.94 \pm 0.02 \text{ and } \frac{\chi_{B19'}}{\chi_R} = 0.71 \pm 0.02$$

The quantities are very similar taking into account that simulation has been done for different NiTi samples.

Another example in Figure 26(a) demonstrates the incomplete transformation of austenite to martensite. Incomplete cooling loops (ICL) reveal untransformed parts of the austenite phase at different stages. It is noteworthy that neither transformation path nor final magnetization doesn't change compared to a regular full cycle. We can see that at

the highest stage even the R-phase is involved in the reverse transformation to austenite, despite the stop temperature looks below R to B19' finish transformation.

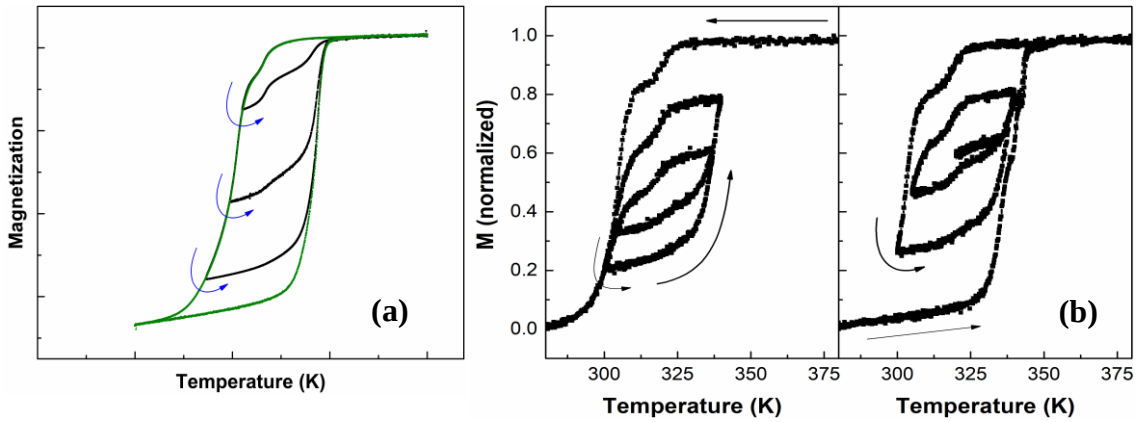

Figure 26. Incomplete transformation and "spiral" MT.

In another experiment (Figure 26(b)) ability to follow the ratio of martensite and austenite phases was applied in order to get to the middle of the transformation hysteresis, that is to have approximately equal parts of each phase. For the first loop started in austenite the temperature sequence was as follows:400-300-340-303-337-320-280[K]; for the second one starting from martensite: 280-345-300-340-305-335-320-380[K].

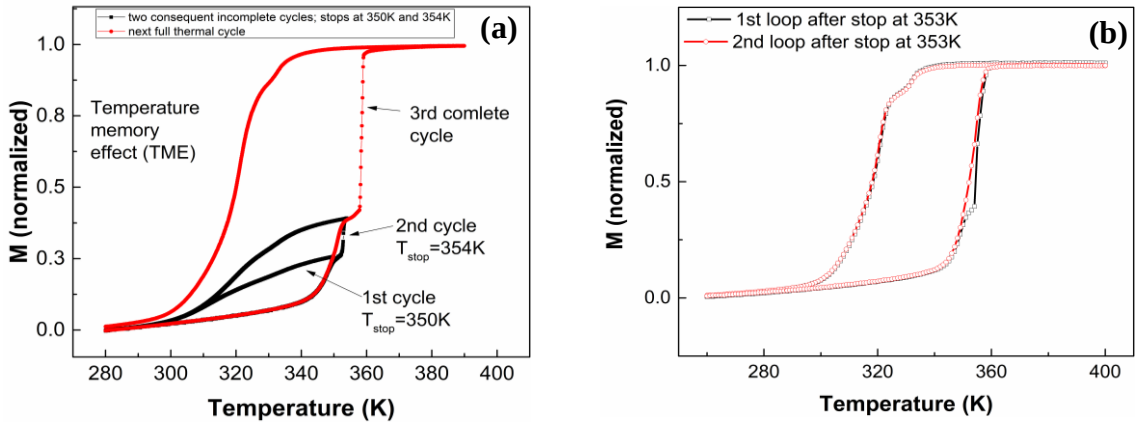

Figure 27. Temperature memory effect as a result of incomplete heating cycles in NiTi.

Another interesting feature arising from incomplete transformation is known as temperature memory effect (TME)[116]. TME in shape memory materials is still under research for application in the field of over-heating monitoring [117]. This effect arises when a transformation is stopped at any temperature T_{stop} between As and Af, then material cooled back below As, and on the next transformation kinetic stop appears slightly above T_{stop}.

The observations of the effect through magnetic measurements are coherent with the other studies of TME in NiTi[116]–[119] done by means of calorimetry or resistivity measurements. When NiTi is transformed back to martensite after incomplete transformation to austenite, there are two different martensite phases, first one that was not transformed upon incomplete heating and the newly formed one. The bump observed in M(T) plot during the next transformation to austenite is correlated to the stress at the interface between both martensite phases, the martensite formed after temperature stop transforms first and then the initial martensite finishes the transition to austenite. TME vanishes after first full transformation, as new coherent martensite arises from the austenite phase (Figure 27).

The examples in this section demonstrate that magnetic measurements may serve as an efficient probe for martensite transformation visualization, revealing the changes in transformation during thermal cycling, amount of the phases and any changes related to crystal structure transformation between martensite, austenite and intermediate R-phase. Equivalently to typical for SMAs thermomechanical tests, magnetometry measurements may be feasible for constant stress (phase temperature diagram depending on stress level) or other measurements that may study the influence of mechanical or thermal conditions on martensite transformation and shape memory effect. Moreover, magnetometry is a non-destructive, basically contactless method, except the need to attach the sample to the sample holder.

Summary

In this chapter we investigated magnetic and structural features of sputtered NiTi shape memory alloy. The samples were defined as slightly Ti-rich, with B2-B19’ martensite transformation and, also, with B2-R-B19’ transformation. It was demonstrated that magnetic susceptibility reflects all the stages of the transition. No noticeable influence of an external magnetic field on neither transformation temperatures, nor magnetization amplitudes was found. The magnetometry probing capabilities of shape memory alloys transition temperature and stress state are demonstrated, magnetic measurements are feasible to reveal some particularities as temperature memory effect, change of the transition path or relative amount of each phase.

As was assumed in few previous publications, magnetic susceptibility in NiTi originates from Pauli paramagnetism. This assumption was quantitatively examined by comparing the experimental results with ab-initio calculations. Partially satisfying results were found, in particular on the temperature dependence of magnetic susceptibility. The role of exchange enhancement and some other particularities of electronic system are discussed.

CHAPTER III. **MAGNETISM OF NITI DEFORMED IN TENSION**

In the previous chapter NiTi magnetism and its correlation to crystal structure and to the density of states were investigated. Now, it is of particular interest to test and to study these relations as a function of strain. First, because the strain is expected to modify NiTi structure at both macroscopic and microscopic levels. Second, because deformation is the common procedure of NiTi treatment, and it is necessary to induce a shape memory effect, which will be applied for magnetic anisotropy control in the last chapter.

III.1. **Tensile deformation of NiTi and experimental limits**

The aim of the section is to establish the deformation experiments, to characterize tensile deformation applied to the studied NiTi ribbons while preparing the set of the deformed samples for the following study of their structure, magnetism and for anisotropy control.

Tensile deformation experiments were done with the valuable help of Marc Poncot and Adrien Letoffe in the Institute Jean Lamour. Deformation Devices System (DDS) by Kammrath Weiss Gmbh was used. All the samples were deformed at room temperature, i.e. in the martensite phase of the alloy. Deformation was performed at 2 μm/sec deformation velocity. During regular tension experiment, elongation of the specimen was measured by linear displacement gauge equipped in DDS and the corresponding force was recorded. In several cases, ARAMIS Adjustable camera system was used along with tension experiments in order to measure local strain and to compare with average strain measured by DDS. It is a digital image correlation (DIC) technique, that allows precise measurements of strains in 3D. After deformation, magnetometry is performed on the samples at the same martensitic state without any additional processing.

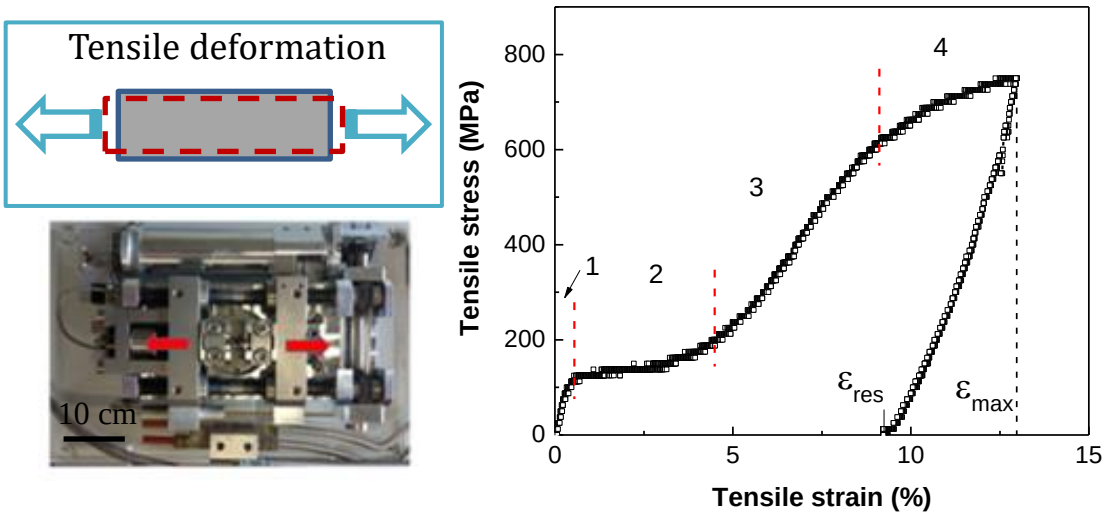

Figure 28. Sketch of tensile deformation provided by the machine on the photo with the direction of stretching. On the right, resulted stress-strain curve of NiTi in martensite measured by DDS.

Typical stress-strain curve of sputtered NiTi 20μm sheets is presented in Figure 28. Tensile stress in y axis is an engineering stress ε_E, which is the force applied to the initial cross-section of the specimen. All the expected stages of stress-strain behavior of standard NiTi are observed, as it was described in section I.2.4. When stress reaches 120MPa, initial elastic deformation replaced by stress plateau at stage 2. The plateau is finished at 180 MPa of applied stress resulting in 4.5% tensile deformation. At this point, stress-strain values are very similar to regular NiTi samples that could be found in the literature [1],[43],[120]. However, the onset in the beginning and the end of the plateau is not observed in our measurements. This stress-drop associated with the start of Luders band nucleation [121]. But this type of band was not observed in DIC experiments upon deformation. In a couple of articles where one may find stress-strain curves of sputter deposited NiTi in the martensite phase, such stress drops are not present as well [2],[122],[65]. After this stage, the significant yield of stress takes place until the yield slightly decreases at stage 4, where deformation of the maximally reoriented sample (as much as it possible for a particular case) becomes mainly plastic and strain rises until fracture. The observed differences may be accounted on different texture and type of the sample(e.g. sheet or wire)[121].

Set of DIC experiments have been performed in order to characterize in details strain distribution along the specimen length and to correlate it with conventionally measured engineering strain for the whole sample:

$$\varepsilon_E = \frac{\Delta L}{L}, \quad (4)$$

where L is the initial sample's length and ΔL is the relative elongation of the sample along the tension direction.

The experiment was also dedicated to measuring strain recovering abilities of the sample, that is shape memory effect (SME). The specimen is painted with random black and white pattern, it permits ARAMIS DIC setup to measure relative displacement in any point of the surface recognized by the software. The green area in Figure 29(I) shows the pattern area recognized for processing by DIC software. In the stress-strain plot, only this area is demonstrated, without a real surface of the sample, to make the figures clearer.

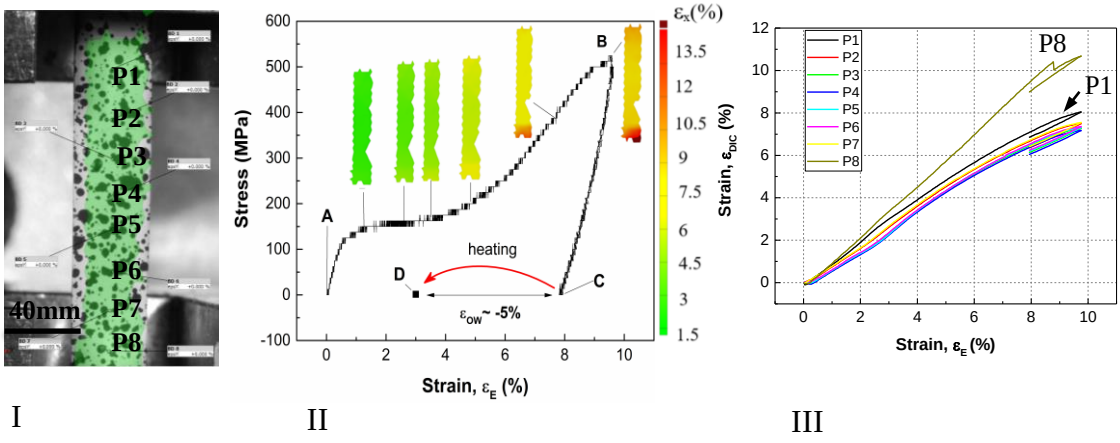

Figure 29 (I) Image of the sample and numerical pattern seen by software before deformation. The indicated points were used in the part (III) to plot the strain distribution along the sample. (II) Stress-strain curve of the experiment with corresponding strain maps.

Strain maps presented in Figure 29(II) visualize the tensile deformation of the sample at particular points on the stress/strain curve. Points designated in Figure 29(I) are plotted on part III of the figure as a function of overall strain ε_E. Strain evolution along the sample is almost equal in the elastic part of the stress-strain curve. Then, at the beginning of the stress plateau, edges start to deflect from the central part of the sample. At the end of the plateau, variation of the strain ε_D ≈1% between the middle and the edges of the NiTi sheet. At this point, significant deformation starts to localize near one of the sample's edges (P8) and at the maximum deformation point B, $\varepsilon_D \approx 3.5\%$. However, for the central part of the sheet (P2 - P7), strain distribution is not larger than 0.4% for the whole deformation path till stress release at point C. For following experiments, only the central part of the NiTi sample have been used unless the DIC technique was applied along with tension experiments. To avoid confusion, the central part of the sample is an area of ~12mm long (2/3 of the specimen's area between the clamps of the tensile machine) in the middle of the deformed NiTi sheet.

To supplement this investigation, the case of the largest deformation is presented in Figure 30. The sample was deformed up to $\varepsilon_E = 20\%$ until fracture. Similar to the previous case tendency can be observed, deformation start to localize near the borders with the beginning of stress yield at stage 3. This localized deformation propagates to some extend towards the middle of the sample at the "plastic" stage 4 till the fracture. Finally, at the point just before the fracture, these areas near the borders exceed in up to two times the strains in the central zone. Still, the central part of the sample is much more homogeneous and local deformation at maximum tension is in the range from 15.8% to 19.3%.

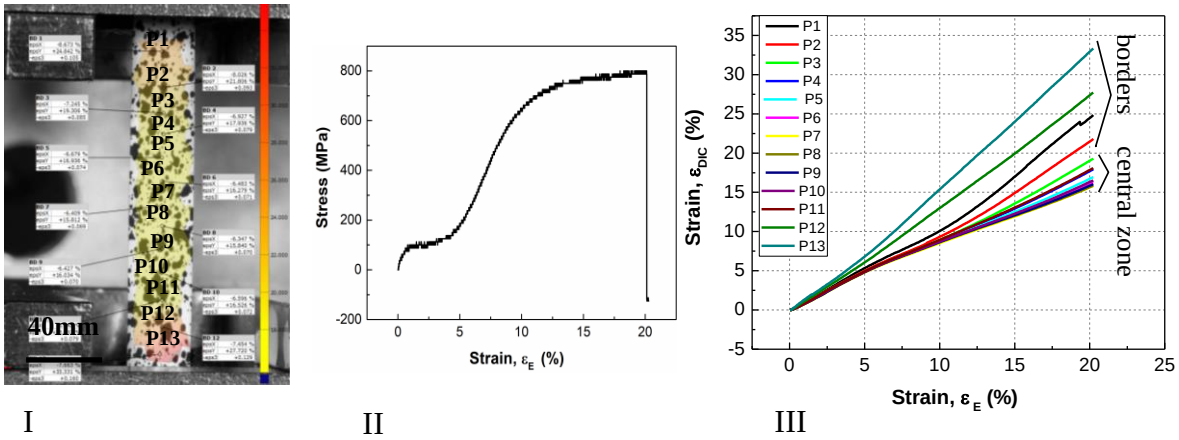

Figure 30. (I) Image of the sample inside the tensile machine at the maximum deformation before fracture. The indicated points were used in the part (III) to plot the strain distribution along the sample. (II) Stress-strain curve of the experiment.

Table 2 provides a summary of the dependence between strain measured by digital image correlation and tension tests. Values in Table 2 refer only to the central part of the sample with the exclusion of the area over~3mm from the lateral borders. Since most of the samples for the study of magnetism are deformed without DIC system, this table will be used in next chapter to define the error bars and the strain in particular part of the sample, knowing only engineering strain ε_E during tension. Besides, Figure 31 shows that residual deformation ε_{res} after stress relaxation (see point C in Figure 29) shows a fairly linear dependence on maximum engineering strain ε_{max} (point B in Figure 29). Therefore, we are able to get a quite precise value of ε_{res} just by measuring ε_{max} during tension tests.

ε_E, %	ε_{DIC}, % (average)	ε_D , % ($dispersion\ range$)
3	2.6	0.4
5	4.6	0.8
7	6.3	1
9	7.6	1.2
11	9.5	1.3
13	11.1	1.6
15	12.7	2
20	17.3	4

Table 2. Summary of strain dispersion and its correlation with maximum strain applied to the whole NiTi sheet.

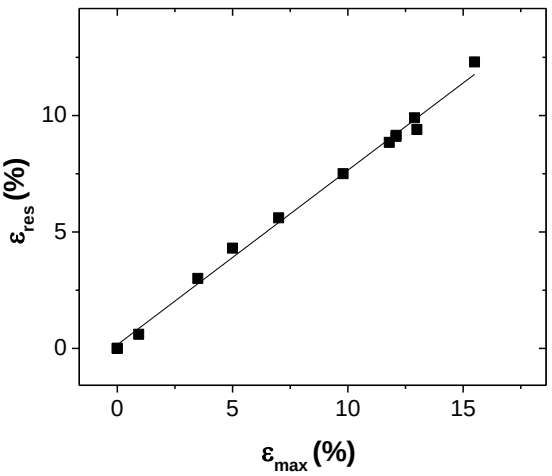

Figure 31. Correlation between maximum and residual strains.

After the deformation, the sample shown in Figure 29 was sequentially heated and cooled two times in order to record the strains induced by two-ways shape memory effect by DIC measurement. Strain at a central point (so-called P5 in Figure 29) is plotted as a function of temperature in Figure 32. Starting point C corresponds to a state with residual deformation at the end of tension experiment (Figure 29-II). While heating NiTi from point C to D, strain is recovered by $\varepsilon_{OW} = 4.9\%$. This observation corresponds to the one-way shape memory effect. Strain maps on Figure 32(II) demonstrate the process of length shrinkage upon the first heating of the specimen. Martensite transformation happened at a higher temperature then usual transformation. This feature of NiTi SMAs is known as martensite stabilization [123] and will be discussed later in the chapter.

During subsequent cooling (down to 300K) and heating (up to 450K), deformation of the sample is ±1.3% according to usual martensite transformation is shown. Hence, tensile deformation of the sample induced a two-way shape memory effect (TWSME). It is interesting that our results are very similar to analogous experiments on cold-rolled commercial equiatomic NiTi samples in the works of Liu et el [43], where the efficiency of TWSME developing by tensile deformation was studied. In other words, the dependence of ε_{OW} on ε_E is the same.

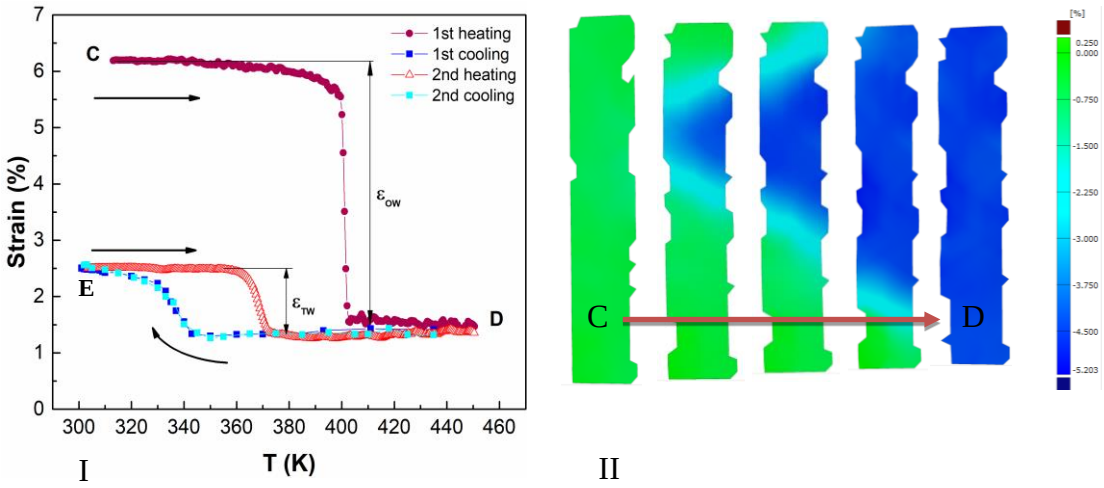

Figure 32. Shape memory effect after initial deformation measured by DIC: (I) strain along axis of tension as a function of temperature; (II) strain maps of the sample, corresponding to the transformation region upon heating .

The present section summarizes the results obtained on tensile deformation experiments and applied techniques. Distribution of the strain within the specimen is studied for different strain rates, its limits and dispersion are defined for the following sections, where the structure and magnetism of the samples will be investigated. Two-way shape memory effect induced by tensile deformation was measured and quantified.

III.2. **Structural study of deformed NiTi.**

In the previous chapter strain distribution of the NiTi ribbons is carefully characterized. Now the crystal structure will be studied as a function of the strain. The goal of this investigation is to find any common features at the atomic scale, which may influence the magnetism of the alloy. Lattice constants as a function of applied strain for martensite and austenite phases would be sufficient base to calculate Pauli magnetism.

III.2.1. XRD analysis of martensite phase

X-ray diffraction measurements were performed with the same equipment and conditions that are described in section II.1.2 unless the other is mentioned. Bruker D8 Discover diffractometer with Co Kα source was used in this section. In Figure 33 pairs of XRD measurements in 2θ/θ configuration corresponding to different tensile deformation values are shown with the offset in y-axis. Measurements are done for the crystallographic planes parallel to the surface. As always in this work, "Before" means the measurement of as-deformed sample after unloading, without any intermediate treatments (C state in Figure 32) and "after" means that measurement is done on the same sample after one full transformation to austenite and back to martensite (E state in Figure 32). In this way it allows us to compare self-accommodated martensite to its deformed ancestor. Measurements have been done at room temperature, but after heating temperature in the diffractometer is a bit higher (approximately ~5°K higher) then real ambient temperature around. It explains some bumps in "After" curves around 50° in Figure 34.

The set of XRD measurements of stretched NiTi samples comparing to non-deformed one is presented in Figure 34. Change in peak intensities of deformed ("Before") and self-accommodated martensite ("After") suggests that reorientation and detwinning processes result in the significant reorientation of crystallographic planes. Relative distribution of peak intensities in self-accommodated martensite comes close to the one of the non-deformed sample. While for the smallest deformation ε_{max}=3% the peaks intensities/profile after transformation are almost identical to one of non-deformed sample ε_{max}=0%, with increasing the strain this difference becomes more noticeable. At 16% of pre-deformation, which corresponds to the plastic stage of deformation this behavior looks different from all others. Apparently increase of plastic defects constrain the martensite from recovering after thermal transformation, that may explain intensities

of "after" XRD curve not so far from "before" for 16% of strain. However, the intensities of the peaks before/after should not be compared directly. Instead, the ratio of the intensities of the same measurement will be used for analysis. And to make this analysis clearer, intensities corresponding to perpendicular planes are compared to each other, especially (002) and (020). Therefore, the ratio of (020)/(002) peaks intensities before and after transition is presented as a function of strain in Figure 35. It shows that (020) planes grow at the expense of (002) as deformation increases. It means that the monoclinic lattice reorients in average to have (010) instead of (001) plane preferentially parallel to the surface. (020)/(002) ratio increases almost linearly with the strain, suggesting that the constant reorientation takes place along with deformation, whatever is the major twin type at the corresponding transformation stage. Concerning (11-1) and (111) planes, their ratio remains almost the same after any deformation and in the non-deformed sample, while (111) increases comparing to (11-1) in as-deformed sample.

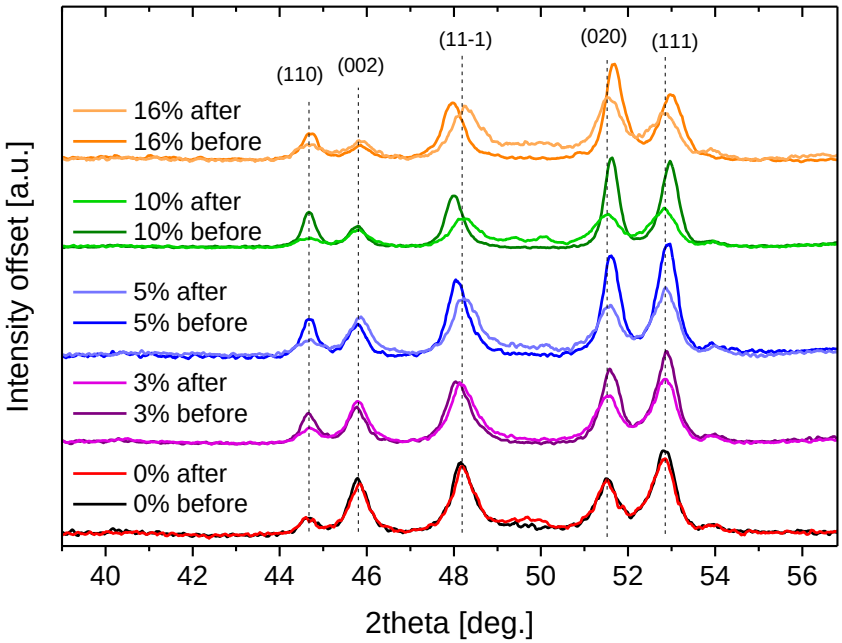

Figure 34. XRD of reference NiTi after tensile deformation, its amount indicated near corresponding couple of graphs. "Before" or "after" means measurement before/after full transformation to austenite and back to martensite.

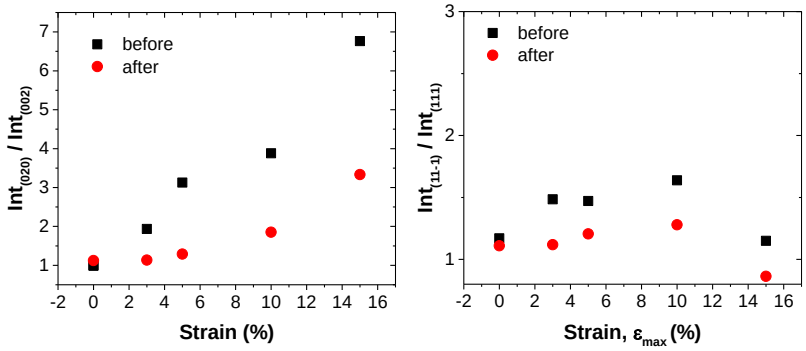

Figure 35. Ratio of (020)/(002) and (11-1)/(111) peaks intensities before and after transition.

In Figure 36 all the XRD measurements of the as-deformed samples together with reference non-deformed sample and the fit of NiTi powder taken from the literature [124] are presented to summarize the influence of the uniaxial tensile deformation on the NiTi crystal structure. First, one can conclude that the peak intensities of our non-deformed sample are very similar to untextured powder, (11-1) equal to (111), (002) is only slightly smaller than (020) while (110) is about one fourth of (002). Second important trend seen in the Figure 36 and Figure 34 is the monotonical shift of the peaks, that corresponds to the change of interplanar distances. Both trends, if they are proportional to strain, represented by the arrows near the corresponding peaks in the figure.

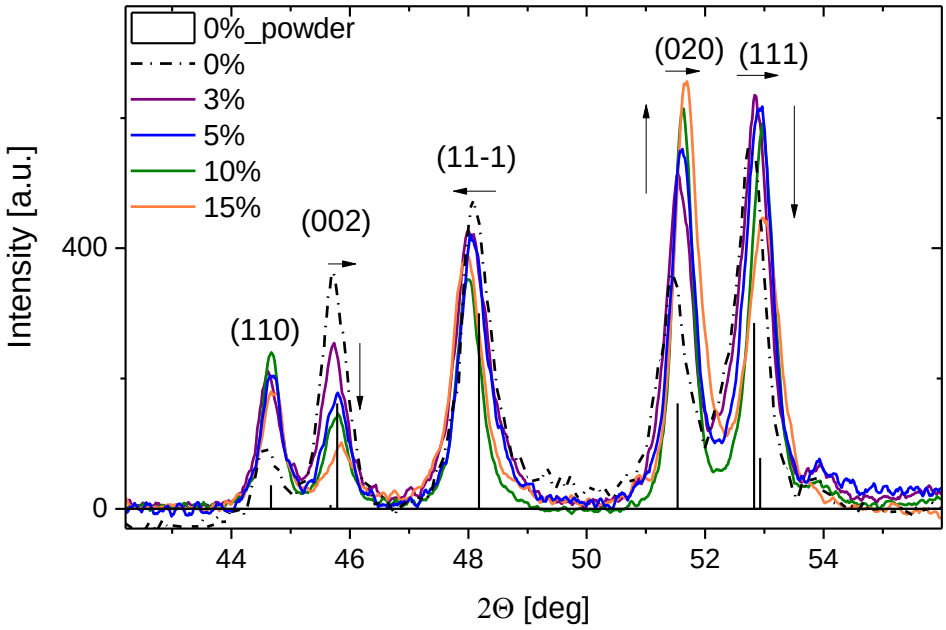

Figure 36. Comparison of deformed martensite XRD measurements before transformation with non-deformed sample and fit of NiTi powder from Pearson's Crystal Data, Ref.[124]. Arrows indicate changes of peak intensities and positions which are persistent with strain increase.

The XRD plots presented in the Figure 34 were used to make a fit of monoclinic lattice parameters using Diffrac.EVA software. These parameters are summarized in Figure 37 as a function of pre-strain. First, the most pronounced result is the change of monoclinic angle β, which increases proportionally to the magnitude of applied tensile strain in as-deformed sample and decreases after full thermal cycle. Increase of β is represented by the increasing distance between the (11-1) and (111) peaks in Figure 36. Concerning three other parameters, the measurement error is much more significant, nevertheless the correlation with strain is observable. The same variation as for β is clearly observed for parameter *a*, which is mostly defined by the same distance as angle

β and by (110) peak. In as-deformed sample parameter *b* decreases with increasing strain amplitude, while *c* increases, except the last point, corresponding to the largest deformation. In the "after" state, the picture is inverse: *b* increases, except for the largest deformation, while *c* decreases proportionally to strain magnitude.

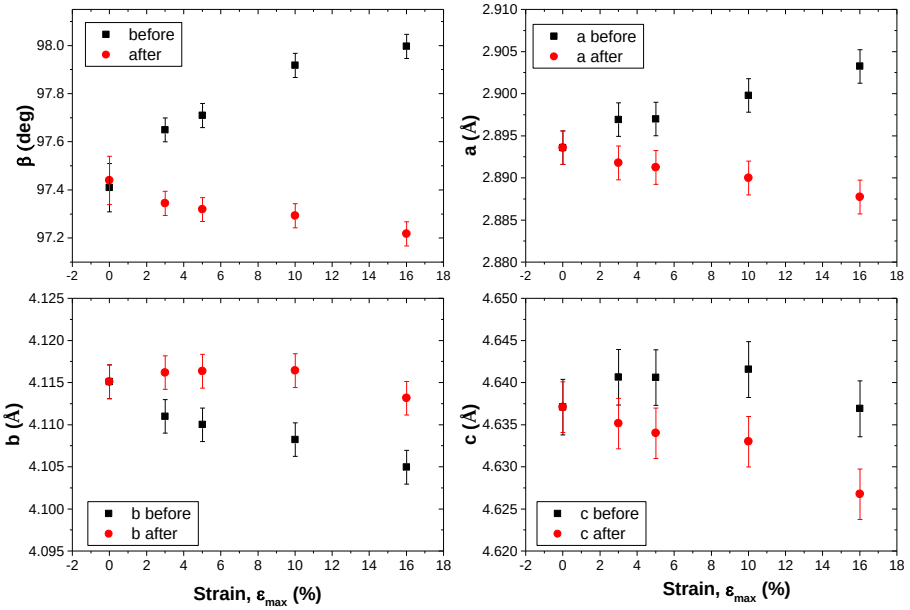

Figure 37. Lattice constants of monoclinic unit cell as a function of pre-stretching magnitude, extracted from the XRD measurements at ambient temperature.

Interestingly, we didn't find any equivalent studies in literature, where the influence of tensile strain in martensite phase on NiTi lattice was studied. For example in the case of deformation by rolling (and not tension), Prokoshkin et al. [125] didn't find any variation of lattice parameters more significant than measurement error. Usually stress-induced martensite is studied by deformation in austenite phase[126]–[128] that makes comparison with our results invalid because of different nature of martensite and its affection by strain.

As it was shown in the beginning of the chapter, we have strong reorientation after tensile deformation applied, that expressed in growing ratio of $I_{(020)}/I_{(002)}$ peak intensities. $I_{(020)}/I_{(002)}$ drastically increases in 2 times for 3% of pre-strain and in 7 times for 15% (see Figure 35). It means that monoclinic lattice reorients in such a way to have less (002) planes and more (020) planes parallel to the surface. To clarify the relation of this reorientation with the strain direction and so, to have a better understanding of NiTi texture, pole figures measurements were performed for (11-1), (020) and (002) peaks on the sample without pre-deformation(0%) and initially deformed(10%): before (as-deformed) and after transformation to austenite and back to martensite phase (Figure 38).

The polar angle α in the figures is the angle of in-plane rotation of the sample between the plane parallel to the pre-deformation axis and perpendicular to the sample surface from one side and the X-rays plane of incidence (Figure 38(b). Radius corresponds to the angle ψ of sample tilt, which is the angle between observed crystallographic planes and the sample surface. Colors correspond to the intensity of the measured point.

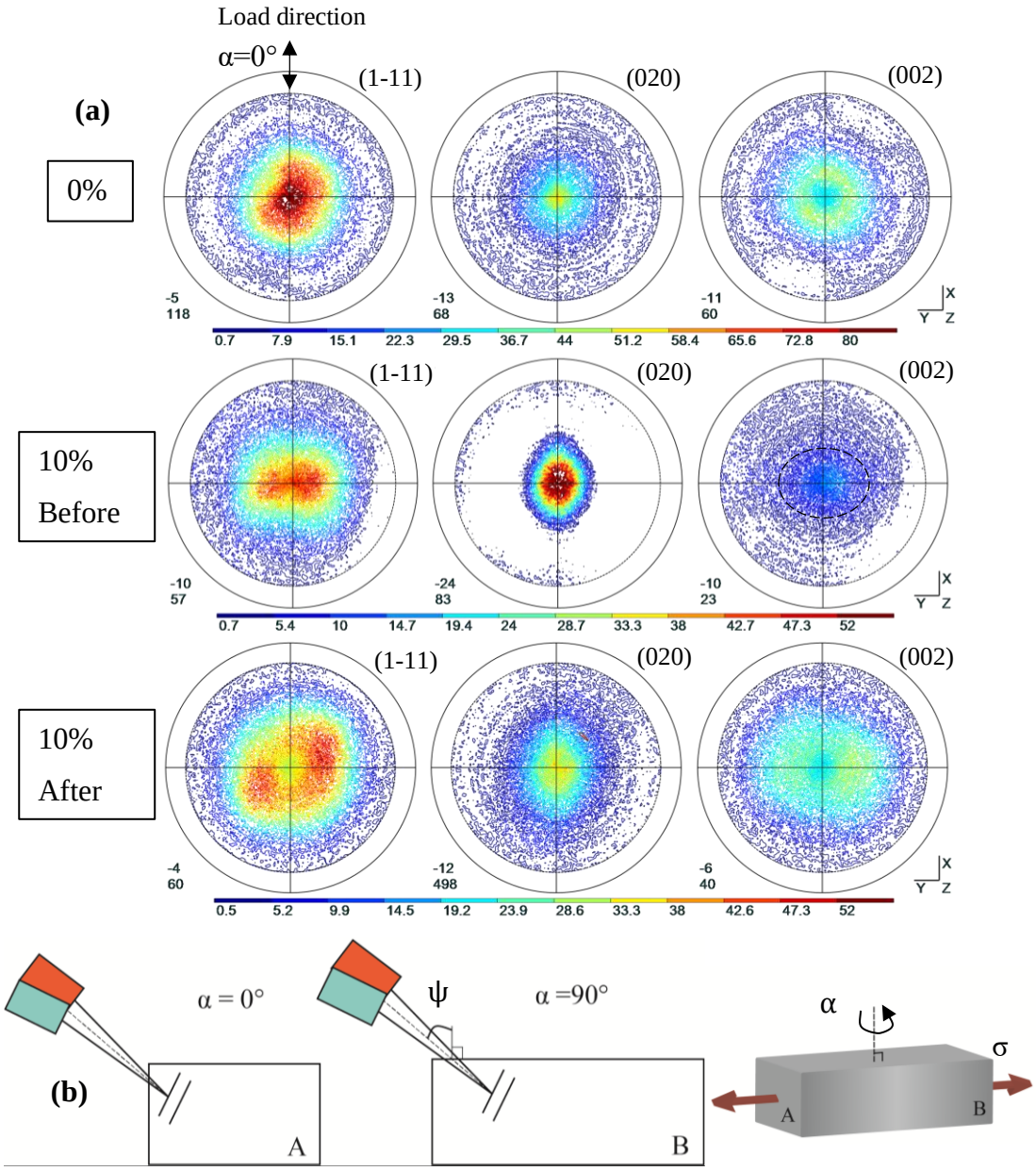

Figure 38. (a) Pole figures for (11-1), (020) and (002) NiTi peaks without pre-deformation(0%) and initially deformed (10%) : before (as-deformed) and after transformation to austenite and back to martensite phase. Pre-deformation direction is parallel to x axis. (b) Sketch showing the geometry of measurements in relation with sample and its stretching direction.

In the case of the non-strained sample, we see that all the measured planes are isotopically oriented and are mainly concentrated in the range of ψ from 0° to 50°. The next set of figures demonstrates anisotropic reorientation of the planes with respect to the pre-deformation direction (i.e. parallel to x axis). Indeed, in agreement with previous XRD measurements (see Figure 34) we observe a strong enhancement of (020) planes and reducing of (002) planes intensities at the small ψ angles, that is more parallel to the surface. In the same time (020) and (11-1) planes become more present at α=0° then at 90°, while (002) planes are more present at 90° though the difference is not so strong, and the planes are greatly spread at different angles. Generalizing, these results show that the partial reorientation happens in such a way to have {010} planes more parallel to applied stress and {001} more perpendicular, so [001] direction of monoclinic lattice tends to lie roughly in the direction of applied tensile stress. Such reorientation along [001] looks reasonable from the perspective that this is the longest side of the lattice, thus it minimizes elastic energy of the microstructure. Preferred [001] reorientation is also in agreement with investigations of texture under applied uniaxial stress presented in the literature [42], [59]. After heating, the features observed in the as-deformed sample texture partially disappear. It is noteworthy that concentrated near the surface (020) planes, and (11-1) in lesser manner, are spread in different ψ angles, that explain observed reduction of peak intensities in Figure 34. Indeed, distribution of intensities get closer to non-deformed sample, however preferential orientation of (020) along α=90° is still present. In the same time (1-11) and (002) planes looks to be turned on 45°.

III.2.2. XRD analysis of austenite phase

After martensite phase, XRD analysis was performed at high temperature austenite phase. Diffraction plots of NiTi in austenite phase for 0%,3%,10% and 16% of pre-strain showed in Figure 39, the pattern correspond to base cubic centered lattice of austenite. After being deformed in tension, each sample was heated to 470K in order to complete transformation to austenite phase, then the XRD measurements were done at 400K. In contrast to martensite, no significant changes in peak positions were not observed. However, it was not possible to fit all austenite peaks together, it may indicate distortion of the austenite lattice. The average fitted *a* parameter of cubic lattice shows no significant dependence on strain and variates around 3.016±0.002 Å. It is noteworthy

that the main diffraction peak, corresponding to (110) plane, is broadening as pre-strain increases. While for 3% it is almost the same as for 0% strain, peaks corresponding to 10% and 16% of pre-strain are much wider. Peak broadening, as well as distortion of lattice, can be related to microstresses induced by dislocation networks of deformed martensite, which are confirmed by TWSME. Moreover twin domains, induced by martensite deformation twins , were also observed in austenite phase transformed from martensite strained above 3%[59], [62]. Peak broadening was also observed in [63] as a result of shear deformation.

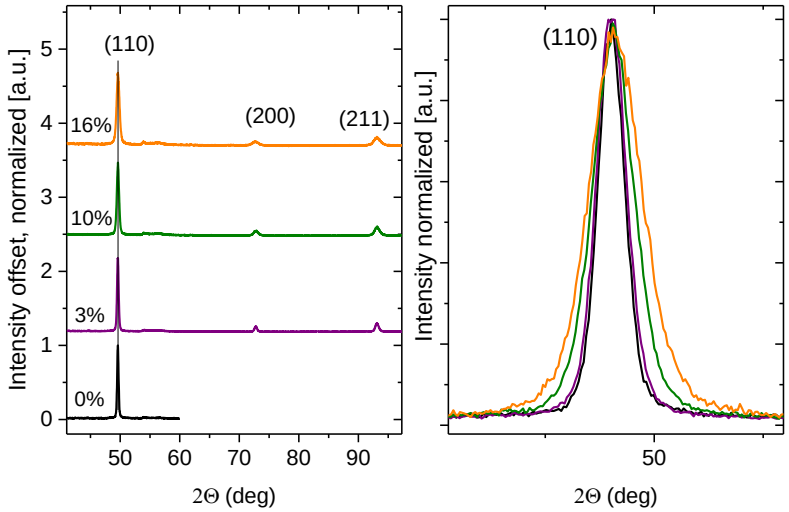

Figure 39. XRD of NiTi in austenite phase at 400K for 0%,3%,10% and 16% of pre-strain (on the left) and the plot of superimposed (110) peaks with normalized intensity for all the represented strains (on the right).

Series of XRD measurements done at high temperature in section II.1.2 compared to analogous measurement of deformed sample. Resulted lattice parameter *a* of austenite BCC structure of severely pre-strained sample and non-deformed NiTi in Figure 40 demonstrates equal temperature dependence in both cases.

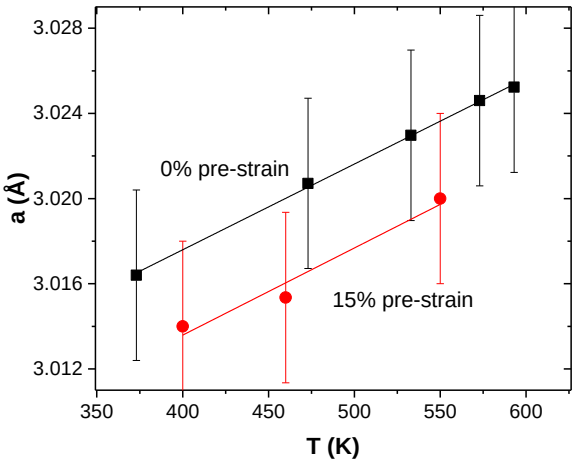

Figure 40. Lattice parameter a of BCC austenite structure as a function of temperature.

III.2.3. Discussion and conclusions on common features from XRD analysis.

Summarizing the strain dependent X-ray diffraction study of NiTi a few important conclusions may arise. First, increasing tensile deformation generates a monotonic change of lattice parameters (see Figure 36): increase of monoclinic angle β, lattice parameters *a* and *c*, and decrease of *b*. This trend is completely opposite for the same deformed NiTi sample after the full thermal cycle to austenite and back to martensite. In both cases, there is one point at maximum deformation which is out of trend, but the 16% sample demonstrated discrepancies and distinct behavior also in XRD and magnetic measurements, which can be accounted for dominated plastic deformation at this stage or more significant error. Noteworthy, that the same tendency of β, *a, c* increase and *b* decrease was observed on cooling in our samples (Figure 15), as well as by other authors [51] and theoretically predicted [86]. The same tendency of lattice parameters change was observed in the number of other studies, where different influences on NiTi system were studied. In [51], [125], [129] authors demonstrated that in binary NiTi alloy increasing of Ni content above 50% and increasing of transformation temperature leads to the same behavior. Another interesting example can be found in [130], where the authors demonstrated that the addition of Hf to NiTi alloy from 0% to 15% leads to the same changes in the monoclinic lattice.

The theoretical DFT studies of NiTi rationalize the observations stated above. Huang et al.[131] first showed with their extensive DFT study that experimentally observed B19' monoclinic structure is unstable in energy ground state in favor of orthorhombic BCO structure. Since simulations consider the lattice without defects and twin/grain boundaries, the responsibility for stabilization towards observed B19' structure with β~98° was assigned to internal microstresses, generated by these interfacial defects (including twin and grain boundaries). Wagner et al. [132] calculated that the shear stress in order of 1 GPa stabilizes ground state structure to experimentally observed B19'. Sestak et al. [133] superposed the shear stress with compressive or tensile normal stresses and demonstrated stabilization of B19' structure. Ko et al.[86], [134] showed with his modified DFT calculation that temperature also plays the role in stabilizing of monoclinic angle. In [135] Wang and Sehitoglu considered intermediate transition state B19'[1], which plays a role of a barrier between BCO and B2 phases and

showed that this barrier increases and B19' becomes ground state phase when tensile isotropic pressure is applied.

The most interesting for our study, that all above mentioned DFT calculations are showing analogous dependence of the lattice parameters on β [129], [131], [132], [134]. Calculated energy landscapes show that minimizing of energy in NiTi system leads to increase of monoclinic angle β, which results in increase of *a* and *c* and decrease of *b* parameters. Relative change of lattice parameters as a function of β was plotted in Figure 41, where the scatter points represent our experimental data and the solid line is DFT calculations from [131]. Zero in y-axis was assigned for both sets of data at β=97.4° because it corresponds to our reference non-deformed sample and in this way comparison will be easier. The pre-strain dependent change of lattice parameters versus β in the present study is in the same range and direction as the theoretically predicted one. So, one can conclude from our observations that in the scale of crystal lattice the system reacts on applied stress by shear-like movement. Moreover, the same but opposite tendency is seen in newly grown martensite after transformation to austenite and back. It tends to suggest that internal directional stresses responsible for the preferential growing of martensite variants also contribute to such deformation of martensite lattice.

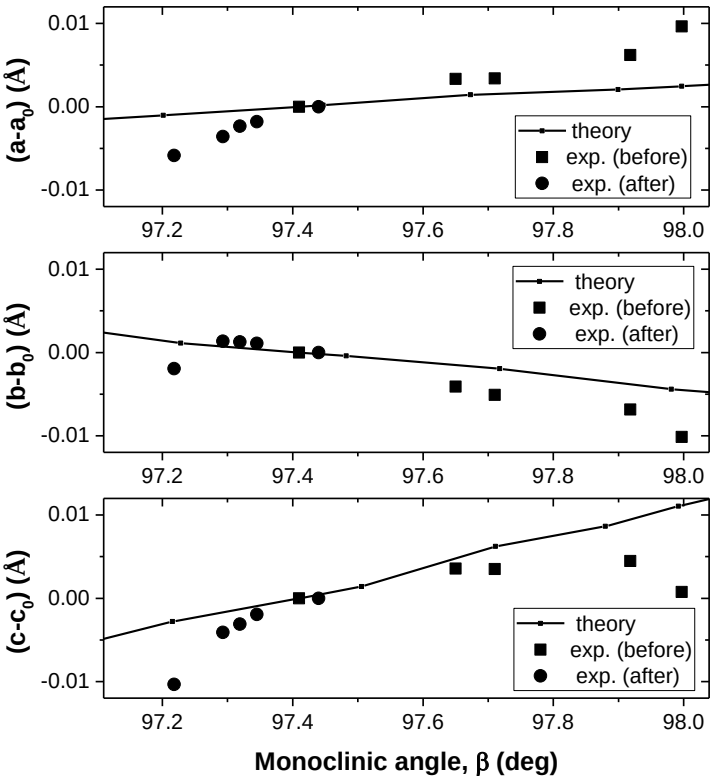

Figure 41. Relative change of lattice parameters as a function of β, where the scatter is our experimental data and the solid line is theoretical predictions from [131]. Zero at y-axis is chosen at β=97.4°, which corresponds to our reference non-deformed sample.

At the same time, in section III.2.1 we demonstrated partial reorientation of monoclinic lattice in the deformed sample in such a way that plane (010) concentrates more parallel to the surface and [001] direction is favored to lie more parallel to the pre-deformation direction, while after transformation observed texture get closer to non-deformed state, but with certain particularities. Therefore, it follows that the tensile stress applied to NiTi leads to structural changes and consequent stress field together with texture change after tensile deformation and after full thermal cycle, which results in the observed tendency of lattice parameters change.

Concluding, shear-like trend in monoclinic crystal lattice resulted from the stresses induced by stretching of NiTi martensite is observed. Such systematical changes on the level of crystal lattice should influence on Pauli paramagnetism. As it was proposed that Pauli paramagnetism is responsible for magnetic response of NiTi, we should be able to see the signs of deformed NiTi in magnetic measurements.

III.3. **Strain influence on paramagnetism of NiTi and martensite transformation.**

Now, when the systematical changes of the NiTi structure depending on applied tensile load are found, we can expect that it may modify the electronic density of states and, consequently magnetic response of NiTi. In the following section this assumption will be examined and NiTi magnetism will be investigated as a function of strain. Then ab-initio calculations will be performed, utilizing the derived lattice parameters, in order to verify the corresponding behavior of magnetism.

Measurement errors and error bars used hereinafter are explained in Appendix A.

Tensile deformation of the NiTi sample typically results in magnetic susceptibility versus temperature characteristic as plotted in Figure 42. Here we realize 2 successive thermal cycles from 250K to 400K and back to 250K. Magnetic field is 20kG, as always in this work. There are two main differences between the first and second thermal cycles of NiTi. The first effect consists in increase ΔT of the reverse transformation temperatures (Af and As) as compared with Af and As of the second cycle, while Ms and Mf remain the same. The second effect consists in the shift $\Delta\chi$ between susceptibility in martensite state before and after heating.

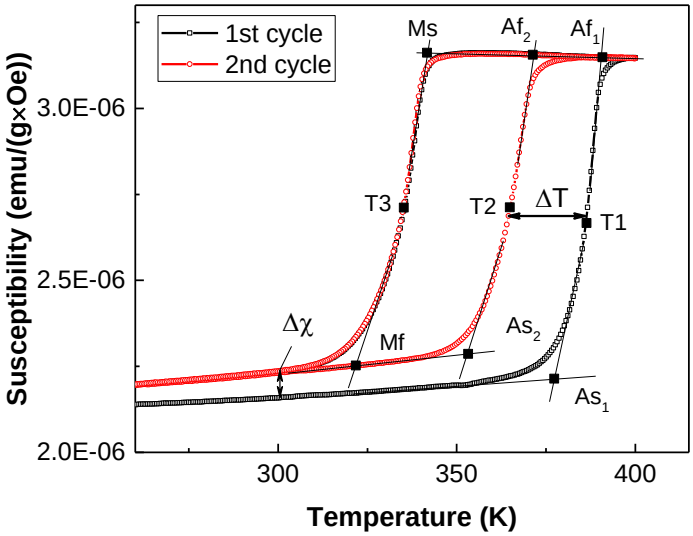

Figure 42. Susceptibility versus temperature data of the sample deformed in tension(ε_{max}=3%).

Transformation temperatures and temperature shift of the first and the second thermal cycle measured in NiTi as a function of strain are summarized in Figure 43. Reverse transformation temperatures increase is the one-time effect, in subsequent cycle As and Af temperatures restore its usual values. The effect is often called deformation or

stress-induced martensite stabilization and obtained results are consistent with the literature [56],[123],[136]. As it was highlighted in section I.2.4, deformation consists of several processes, as the common elastic deformation, martensite reorientation, and new twins formation, as well as detwinning of already present twins, and pure plastic deformation, accompanied by emergence of the defects. Stabilization effect is usually accounted for additional energy needed to overcome above mentioned reoriented martensite, detwinned structures, dislocations and related internal stresses that oppose to transformation. It was suggested in [63] that grain boundaries play an important role, imposing frictional resistance to the shape recovering on heating. Indeed, in [137] it was demonstrated that in single crystal NiTi the effect of martensite stabilization after deformation is much smaller. Moreover, after the transformation is accomplished, some residual oriented stresses remain, especially due to induced dislocation array. It may explain the lowering of T3 temperature of the first direct transformation on cooling. Lowering of T2 is not proportional to the strain and it shifts to some stable value for any strains that exceed the elastic limit. These residual stresses guide martensite transformation on cooling, resulting in preferred orientation of newly formed martensite, which is also responsible for already observed two-way shape memory effect along the direction of applied strain [63],[138].

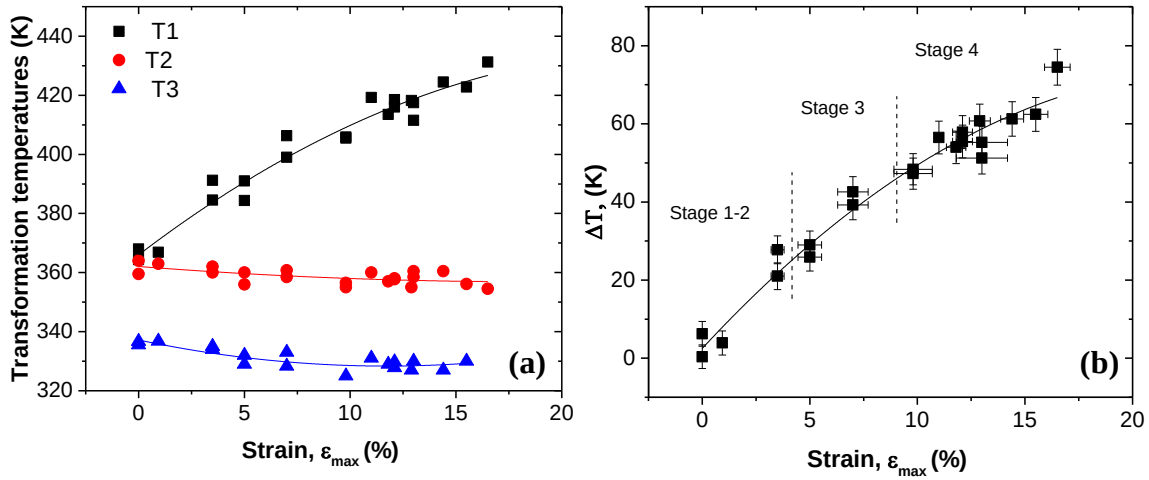

Figure 43. Shift of the transformation temperatures as a function of pre-strain. T1 and T2 are the temperatures of the first and second reverse transformation respectively, T3 is the temperature of second direct transformation (a). Temperature shift between first and second cycle after deformation (b).

The change of the slope of ΔT seems to coincide with the deformation stages. With the given dispersion of the data, it is hard to confirm the slope difference between

stages 2 and 3. On the other hand, decrease of the slope at stage 4 is clear, which may indicate the minor contribution of plastic deformation, dominated at this stage.

Now let's look closer on the systematic features of NiTi magnetic response depending on the strain magnitude. The representative χ(T) plots for the range of applied deformations are shown in Figure 44. Strain values have been selected along the range of all the deformations to have the samples from the different stages. In the same way, as in the previous Figure 42, two consecutive χ(T) measurements after deformation are presented. It is clear that both gaps in susceptibility and in temperature are increasing with applied strain. Moreover, the second transformation cycle is slightly reduced, while the shape of both cycles is less steep. It is interesting that a similar effect of the transformation path smoothing was already observed in the cycling experiment in Figure 24. Similar features can be also found in the strain versus temperature measurement for different pre-strain values in [42], where the "smoothing'' around transformation temperatures appear, or at least much more pronounced at the "plastic" stage 4, as seen here for ε_{max} equal to 12% and 16.5%.

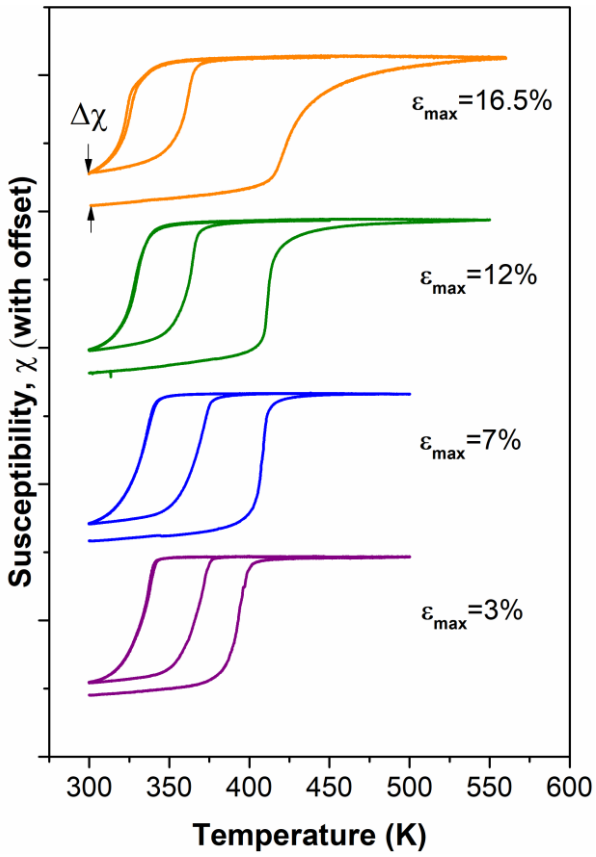

Figure 44. X(T) plots of two subsequent measurements after tensile deformation. Measurements are in original scale but with offset along y axis.

The values of the gap in magnetic susceptibility Δχ as a function of pre-strain are shown in Figure 45. Because of the significant dispersion of the data after 10% it is hard to be sure about the right correlation function between these two parameters. The lowering of the slope occurs after the dashed line which corresponds to plastically dominated stage 4. The data point with non-zero Δχ at 0% strain represents the case when the sample contains some residual stresses after deposition. Depending on the deposition batch, this effect was sometimes observed as a small shift in temperature and susceptibility, like in Figure 24.

The strain-dependent behavior is similar for both ΔT and Δχ, but for ΔT correlation looks more linear. Then it is interesting to look at Δχ as a function of ΔT. A comparison of both in Figure 46 shows that ΔT makes correlation more linear. Divergence from the linear fit decreases because data points belonging to the same pre-strain value relocate in a more rational way, especially in the first part of the plot. However, we don't know what the exact relationship between two phenomena is, so we will examine $\Delta\chi$ further as a function of strain. According to the important role of grain boundaries on martensite stabilization effect[63], it sounds unlikely that considered magnetic effect, or observed in previous section structural changes on lattice scale are closely related.

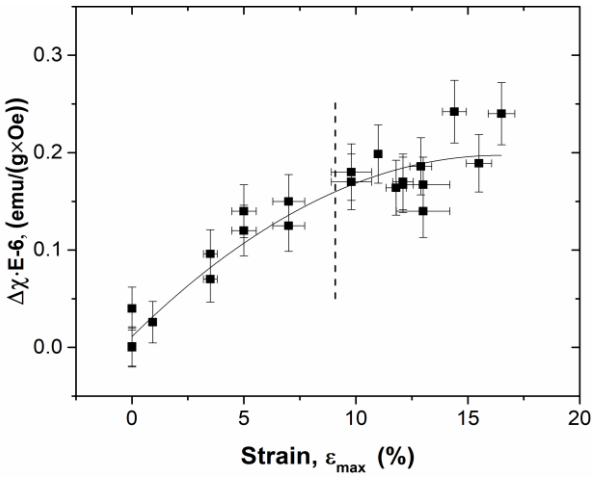

Figure 45. Difference $\Delta\chi$ of magnetic susceptibility in martensite phase before and after full thermal cycle. Dash line shows approximate beginning of deformation stage 4. Quadratic fitting function is used.

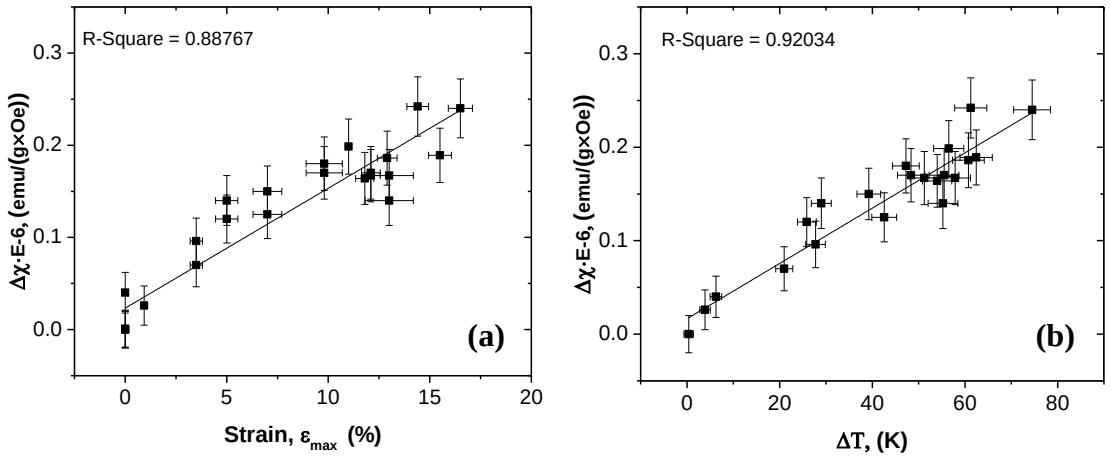

Figure 46. $\Delta\chi$ as a function of: (a)temperature shift on first heating ΔT; (b) pre-straining value ε_{max}. Substitute of strain by temperature makes the correlation stronger, R-square is the coefficient of determination.

To summarize the influence of strain on magnetization behavior of NiTi, three distinct M(T) plots corresponding to maximum, minimum and no pre-deformation is shown in Figure 47. The curves are superposed in such a way to have the same susceptibility in high temperature austenite phase. Such arrangement is rationalized by the shape of density of states at fermi level $D(E_f)$, discussed in section II.2.3. It is

relatively flat in austenite phase, comparing to martensite, so any possible changes of $D(E_f)$ value in austenite expected to be significantly lower. Moreover, no significant changes in the crystal lattice of austenite phase were not found.

From that perspective, effect of strain on magnetic susceptibility may be considered as the sum of amplitudes of the first thermal cycle $[\chi_A - \chi_{1M}]$ and $[\chi_A - \chi_{2M}]$ of the second (see Figure 47(b) and (c) respectively). Not surprisingly, this representation demonstrates larger noise comparing to $\Delta\chi$ versus strain, but the trends of $[\chi_A - \chi_{1M}]$ increasing and $[\chi_A - \chi_{2M}]$ decreasing are clear. We consider that both representation of susceptibility (as $\Delta\chi$ and $[\chi_A - \chi_M]$) versus strain are coherent, because as it was shown by XRD study in previous section that microstructure of deformed martensite is related to its structure after complete transformation to austenite and back.

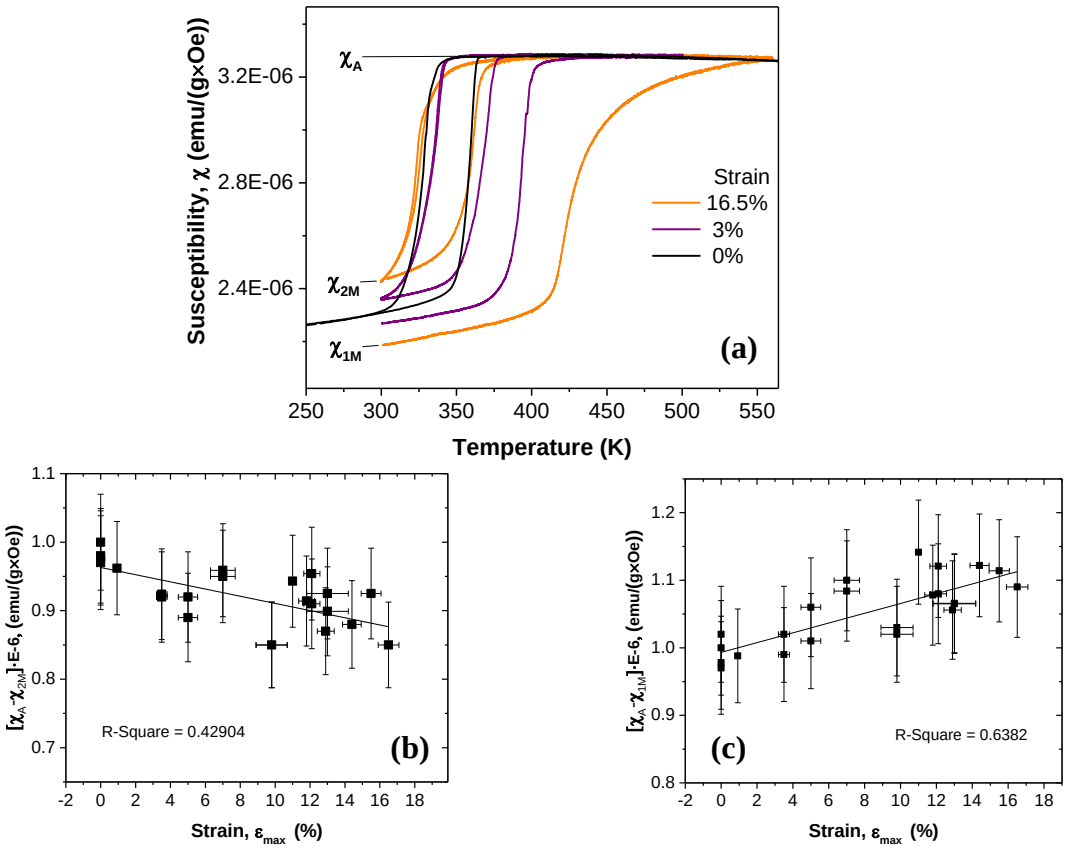

Figure 47. χ(T) plots of the first two measurements after pre-straining up to 3% and 16.5%, with the offsets along χ to have an overlap at high temperature phase (a); $[\chi_A - \chi_{1M}]$ amplitude of the first thermal cycle (b) and $[\chi_A - \chi_{2M}]$ of the second consecutive hysteresis (c) as a function of strain.

The dependencies of the NiTi magnetic susceptibility proportionally to strain were observed, as well as for the transformation temperature shift and crystal lattice. One may expect that χ variation as a function of strain is related to corresponding variation of lattice parameters. Now, the magnetic susceptibility change may be examined by comparing the DOS extracted from the lattice changes.

Ab-initio calculations of strain-dependent DOS

Lattice parameters from the set of NiTi samples, deformed in tension, extracted in section III.2 were used to make DFT calculation of the corresponding density of states in B19'martensite phase of NiTi. In austenite phase, it was found that the changes in lattice parameters are negligibly small and resulted DOS almost the same because of the flat region in the vicinity of E_f. Three representative DOS profiles in martensite phase are shown in Figure 48(a), they correspond to the samples with 0%, 3% and 16% of applied strain. As it was expected, even small changes of lattice parameters modify DOS profiles, especially at Fermi energy due to the narrow dip around it. Summary of $D(E_f)$ corresponding to the four different pre-stretching magnitudes are presented in Figure 48(b). In agreement with magnetic measurements, density of states at Fermi energy increases in state "After" and respectively decreases in state "Before". However, because of the hollow shape, we see that the $D(E_f)_B$ decrease comparing to non-strained sample is one-time in fact, and it becomes almost constant between 3% and 16%. In after state, $D(E_f)_A$ increase is more proportional to strain because Fermi energy in this case appears on the side of the hollow, which moves left as strain increases.

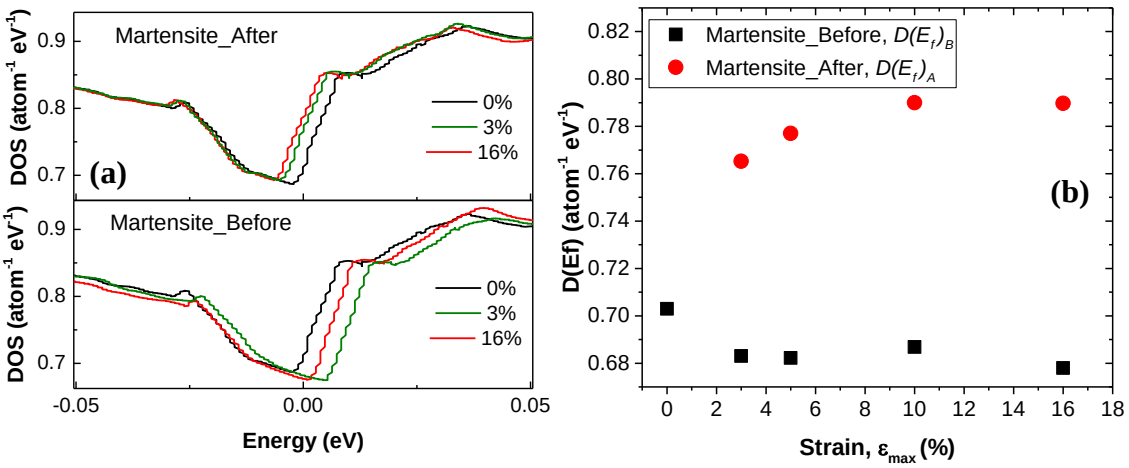

Figure 48. (a) DOS of deformed samples before first heating to austenite and after full transformation to austenite and back to martensite; (b) DOS at Fermi energy.

Results observed above suggest that the correlation between magnetic susceptibility upon tensile deformation of NiTi through the Pauli paramagnetism exists, however, the quantitative relation is still unclear. Consideration of DOS renormalization or exchange enhancement factors, discussed in II.2.3, may put the ratio resulted from DOS calculations magnetic susceptibilities in the range of experimentally observed values, or, considering $5.5k_BT$ averaging $\frac{\chi_{2m}}{\chi_{1m}}$=1.096 and 1.12 for 3% and 16% respectively, while experimental ratios are in the range from 1.04 to 1.18. So, dependence still is not linear, as it was observed in magnetic measurements. In other words, rate of $D(E_f)$ change as a function of strain is not as high as magnetic susceptibility change. Some other contributions should arise. For example, increase of dislocation density is anticipated along the strain increasing, especially at higher deformation magnitudes. It is known that appearance of dislocations in some metals (e.g. Cu) may influence their magnetic susceptibility, it is explained by appearance of narrow quasi-local electron levels near Fermi energy (see [110] and the references inside). Then, upon next thermal cycle, some part of dislocations disappears in newly grown martensite. This factor may provide a nonlinear contribution to magnetic susceptibility variation $\frac{\chi_{2m}}{\chi_{1m}}$. Also, one should to note, that lattice parameters used for calculations were extracted from the planes parallel to the surface, but these parameters should change with the respect to applied load direction. Including these two factors in the future studies may clarify the relation between magnetism and strain in NiTi.

Summary

First, distribution of the strain within the specimen is studied for different strain rates, its limits and dispersion are defined for the following sections. Two-way shape memory effect induced by tensile deformation was measured and quantified. Then, the crystal structure of NiTi is studied as a function of strain by means of X-ray diffraction techniques. Eventually, it was found that tensile deformation generates a monotonic change of lattice parameters in monoclinic structure, mainly characterized by increase of monoclinic angle β proportionally to applied tensile strain and reducing upon full thermal cycle. Presence of identical tendency in monoclinic lattice was found in literature, as the consequence of energy minimization or external influences. Similar inversed tendency for the same deformed NiTi samples after full thermal transformation to austenite and back to martensite was also found. On the other hand, it was rationalized from our XRD

experiments and reinforced by available observations in the literature that unless NiTi is completely polycrystalline, tensile stress induces certain texture in NiTi. It is mainly characterized by a preferential reorientation in such a manner to have [001] direction along applied tensile stress and (010) plane parallel to the surface. Moreover, after reverse martensite transformation the texture becomes close to the non-strained case but with certain particularities related to as-deformed state. Finally, we concluded that in the scale of crystal lattice the system reacts on applied stress by some preferred reorientation and shear-like distortion.

The dependencies of the NiTi magnetic susceptibility proportionally to strain were observed during magnetometry experiments, as well as for the transformation temperature shift. It is shown that the tensile deformation of NiTi results in increasing of magnetic susceptibility amplitude between martensite and austenite phases. Then, after transition to austenite phase and back to martensite, the same magnetic susceptibility amplitude is decreasing, comparing to the non-deformed sample. Taking into account, weak influence of deformation on austenite phase, this effect can be regarded as the gap in magnetic susceptibility $\Delta\chi$ in martensite phase before and after thermoelastic martensite transformation. Strain dependence of $\Delta\chi$ is nearly linear and is similar to observed in the same time martensite temperature stabilization.

Finally, electronic density of states calculations were performed based on extracted lattice parameters from strain-dependent XRD measurements. Results suggest that the deformation induced change in magnetic susceptibility is related to the density of states at Fermi energy $D(E_f)$ in NiTi, as for the Pauli paramagnet material. However, the rate of $D(E_f)$ change is much lower than in magnetic susceptibility. Therefore, some important contributions, which are not included in the model, should be present. For example, the increase of dislocation density with the tensile strain should contribute to magnetic susceptibility.

CHAPTER IV. **MAGNETOELASTIC COUPLING IN NITINOL/ NICKEL BILAYER**

Tensile deformation experiments on NiTi were performed, strain distribution along NiTi ribbon is characterized and, finally, the shape memory effect was observed. In the present chapter the strain, resulted from shape memory effect, is applied to control magnetic anisotropy of Ni. First, the NiTi/Ni interphase is investigated, then the effect of strain on magnetic anisotropy is quantified and the strength of magnetoelastic coupling is discussed.

IV.1. **NiTi/Ni deposition and structural analysis**

We used 20μm thick NiTi sheets, studied in the previous chapter, as substrates to grow 20nm thick Ni film, capped with 5nm platinum. Deposition of Ni(20nm)/Pt(5nm) stack was performed by DC magnetron sputtering at room temperature on AJA physical vapor deposition (PVD) system. PVD base pressure was around 10^{-8} mTorr while the Ar+ pressure during deposition was set between 5 and 6 mTorr. Deposition rate was ensured by profilometer measurement. We also deposited the same Ni/Pt stack on regular Si substrate with native oxide SiOx. They were used for reference measurements and to verify the Ni thickness by small angle X-ray reflectivity.

In order to later discuss the strain transfer from NiTi to Ni, it is required to characterize as much as possible NiTi/Ni interface structural features. Due to time constrain, we could do it only by two methods (atomic force microscopy AFM and transmission electron microscopy TEM) and on a limited number of samples.

First, AFM was used to characterize NiTi surface roughness as shown in Figure 49 (a-c). The overall topography mostly ranges from 0 to 100 nm at the scale of the 20×20μm area and is composed of micron-sized grains, each of which has local roughness below 20nm. Such roughness is still large as compared with Ni(20nm)/Pt(5nm). As was noted in section I.2.2, during martensite transformation NiTi martensite plates grow in highly ordered austenite until they encounter grain boundary, other plates or sample's surface. When reaching the surface, martensite plates uplift the surface and make it rough. Change from smooth austenite surface to rough martensite surface is shown in Figure 49(d-f) with 3 consecutive optical microscope images of stress-induced martensite transformation in our NiTi samples provided by Acquandas

company. Unfortunately, we did not have the capability to measure AFM image at elevated temperatures and therefore we were unable to further quantify austenite roughness.

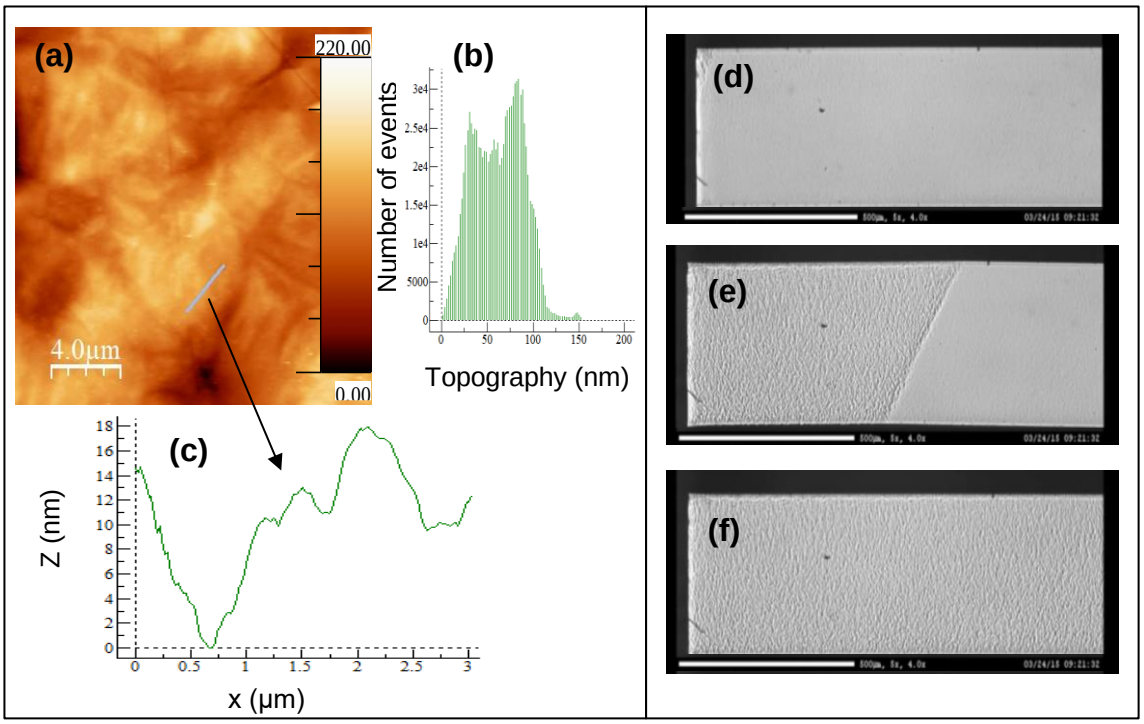

Figure 49. (a) 20×20µm AFM image of NiTi surface at room temperature. (b) Height occurrence as a function of height shows a peak to peak roughness of 100nm over micron distances. (c) Local surface profile corresponding to blue line in (a). (d-f) Optical microscopy images of NiTi ribbon surface that undergoes stress-induced martensite transformation from austenite (d) to martensite (f). Roughness is strongly increased in martensite state.

After deposition of Ni/Pt stack, AFM measurements have been done again (see Figure 50(a)). Local roughness over the smoother plateaus is still of the order of 15nm over few microns but an additional roughness of the order of one or two nanometers now exists at a smaller spatial scale. From Figure 50 (a) it is unclear if the nickel layer is continuous or not. We used magnetic force microscopy (MFM) imaging to get more information. Figure 50(c) shows MFM image at the same location as Figure 50(a). Contrast borders, that are white and black lines are observed, they correspond to the location of magnetic domain wall between domains of opposite magnetization (Ni magnetic moment laying in the film plane). In other words, one magnetic domain of uniform magnetization is always between a white and a black border. The whole imaged area is covered with magnetic domains and the magnetic domain boundaries do not match AFM profile. Therefore, we conclude that the Nickel layer must follow NiTi roughness and it is continuous over the whole tested area. Similar roughness has been measured by

AFM in other regions of the same sample as well as on pre-stretched samples after heating to austenite and cooling back to martensite.

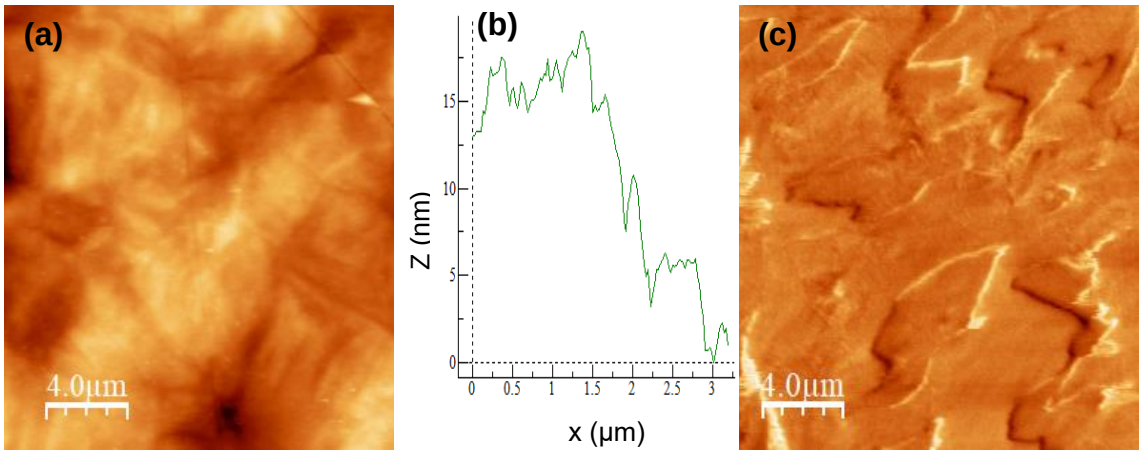

Figure 50. (a) AFM and (c) MFM of the same 20x20µm region on Ni/Pt surface deposited on NiTi. (b) height as a function of position corresponding to the blue line in (a).

To obtain direct information on the NiTi/Ni interface structure and composition, we performed transmission electron microscopy (TEM). After deposition of Ni/Pt stack on 7% stretched NiTi substrate, the sample was heated up to 450K (NiTi austenite phase), cooled back to room temperature and then FIB preparation of ultrathin section was done. Figure 51(a) and (b) show STEM-HAADF (Scanning Tunneling Microscopy- High-Angle Annular Dark-Field) image of the full stack NiTi/Ni/Pt in transverse geometry, i.e. the cut of the initial stack is done along stretching direction(see Figure 51).

In Figure 51(b), TEM confirms that Ni layer is continuous and that its 20 nm thickness is constant over the whole image. Ni is found to be face-centered cubic and polycrystalline with grain size is of the same order of its thickness. Pt surface profile show roughness that matches AFM results in Figure 50(a). TEM shows that this roughness originates from NiTi substrate roughness and that Ni/Pt bilayer just follows NiTi surface landscape. A closer look to NiTi/Ni interface reveals 8 to 18nm thick layer at the top of the NiTi substrate whose crystallinity is different from NiTi and Ni ones. Chemical analysis performed by energy dispersive spectroscopy (EDS) unit in a microscope (see Figure 51(c) reveals that this interfacial layer is an oxidized Ti-rich layer.

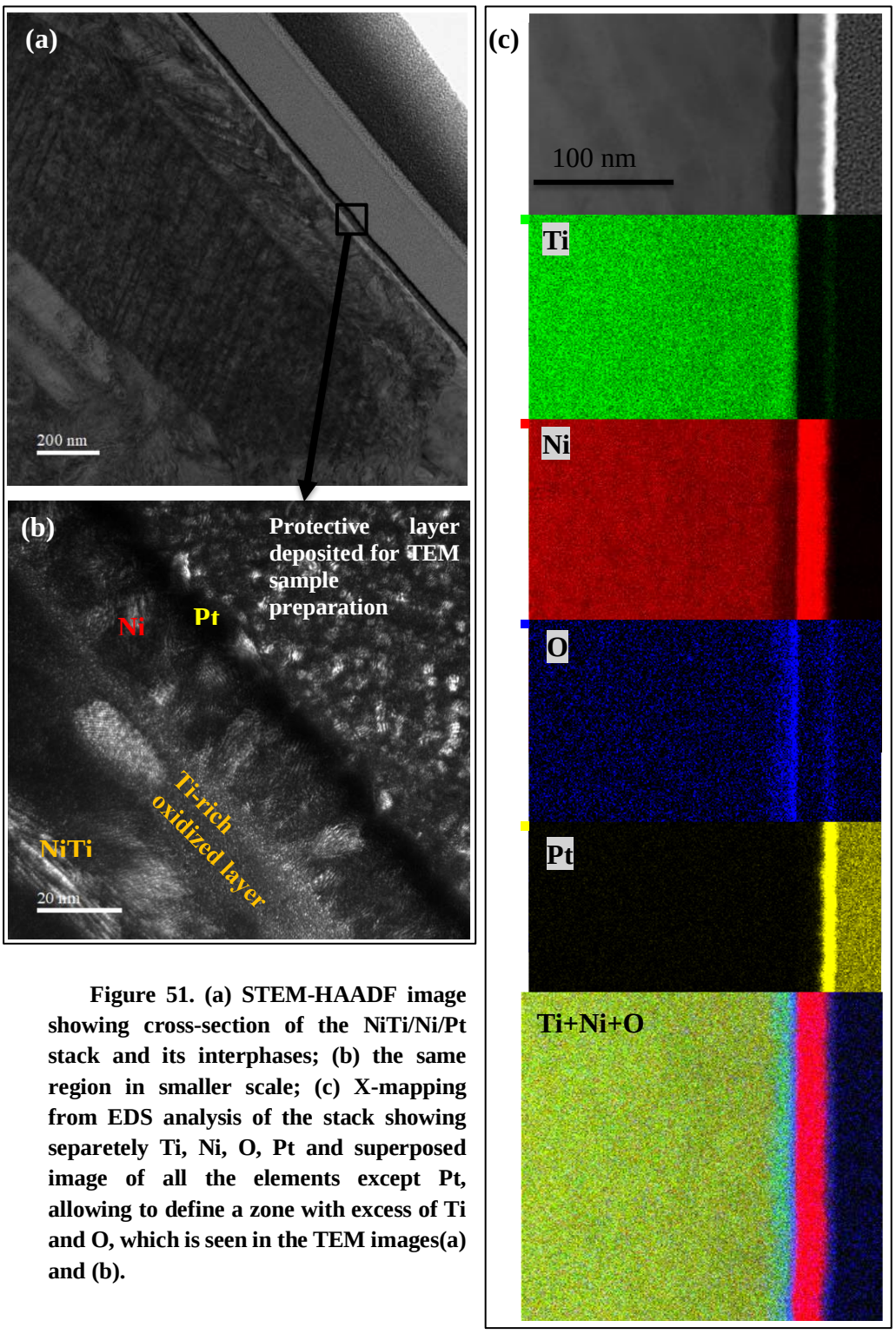

Figure 51. (a) STEM-HAADF image showing cross-section of the NiTi/Ni/Pt stack and its interphases; (b) the same region in smaller scale; (c) X-mapping from EDS analysis of the stack showing separetely Ti, Ni, O, Pt and superposed image of all the elements except Pt, allowing to define a zone with excess of Ti and O, which is seen in the TEM images(a) and (b).

Oxygen can either form an oxide phase or dissolve in NiTi matrix as impurity[139]. It is known that oxygen tends to create a bonds with Ti, forming TiO_2 [140], [141] or Ti_2NiO is also often observed in Ti-rich alloys[65], [82]. NiTi has a property to form naturally oxide on its surface in ambient conditions[142] and clearly, there was enough time between NiTi production and Ni deposition to form this oxide

layer that we observe with TEM. However, the composition rate of our Oxygen-rich layer doesn't allow to conclude neither about TiO_2 nor Ti_2NiO, because the level of Ni is too high. Probably it is also related to the Ni diffusion from the Ni layer that may happen on heating, the narrow(~3nm) Ni-rich layer at the border between deposited Ni and O-rich layer of NiTi is observed as brighter than around stripe in Figure 51(b). Its composition of Ni is rising to 60% in contrast to 30% few nanometers further to NiTi, while O only increases from 5% in bulk to more than 20% at NiTi/Ni interphase.

Before discussing magnetic features of Ni layer, strain in Ni film may be extracted from TEM image. The sample underwent the same stress/temperature history as those studied by magnetometry. So quantifying Ni strain will later help to characterize magnetoelastic coupling. Lattice strain was deduced from TEM images, in particular, those shown in Figure 52. Interplanar distances $d_{(111)}$ between (111) planes were calculated from diffraction patterns(second row in Figure 52) extracted by means of Fast Fourier Transform from the areas limited by red squares in high-resolution TEM images. The radius of the first diffraction circle corresponds to $d_{(111)}$ along z (vertical) and along x axis(horizontal). Poisson's ratio of Ni, $\nu_{Ni} = 0.31$ was used. First, expected "unstrained" interplanar distance d_0 was extracted from the relationship: $\upsilon_{Ni} = \frac{d_0 - d_z}{d_0 - d_x}$. Then in-plane strain in Ni (ε_x^{Ni}- ε_y^{Ni}) can be calculated, knowing that $\varepsilon_x^{Ni} = \frac{d_x - d_0}{d_0}$ and $\varepsilon_y^{Ni} = \varepsilon_x^{Ni} \cdot \upsilon_{Ni}$. Analysis showed that strain distribution is inhomogeneous, in-plane strain ε_x^{Ni}- ε_y^{Ni} changes from +0.1% to 3% in different zones, average value estimated over 9 different zones is +1.3%.

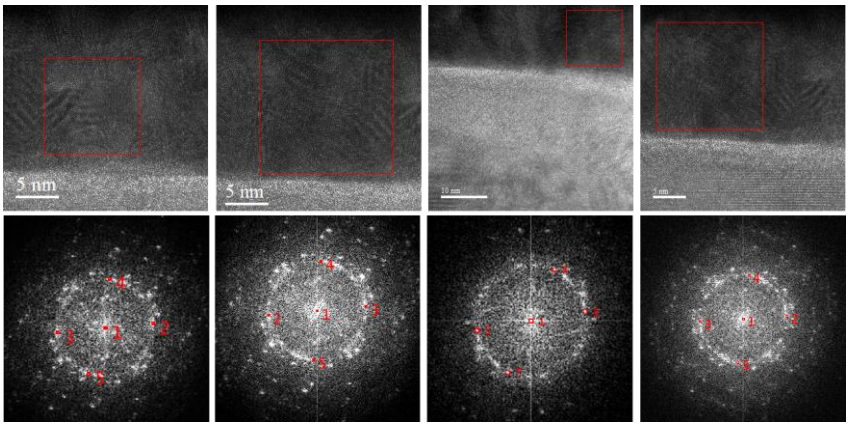

Figure 52. Some of HR-STEM images (upper row) and corresponding FFT, that were used to define lattice strain in Ni at state E.

IV.2. **Magnetic anisotropy of Ni induced by shape memory effect in NiTi**

After structural analysis of deposited NiTi/Pt stack and its interface with NiTi, the range of angle-sensitive in-plane magnetic measurements is performed in the following for the set of NiTi/Ni samples. The NiTi substrates in the form of ribbons are pre-stretched in the range of engineering strains ε_E from 3% to 11% prior to deposition.

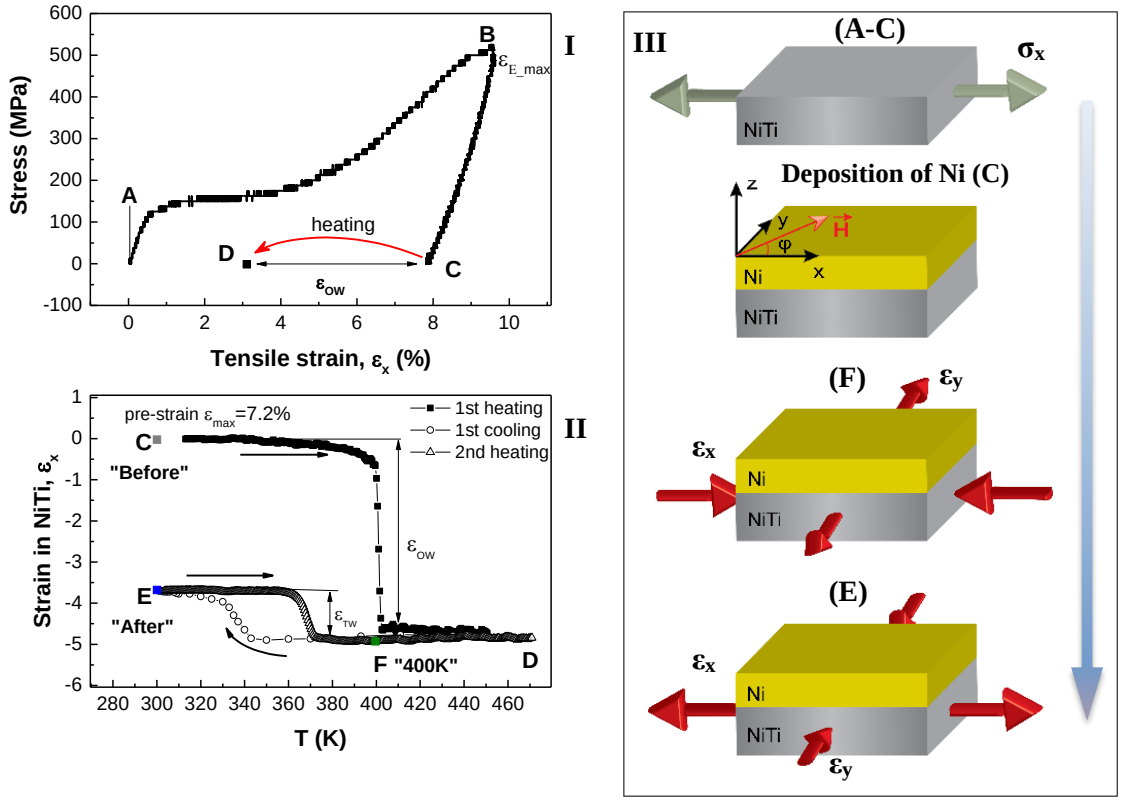

Figure 53. Workflow of sample preparation and its "life cycle". The sketches on the right(III) correspond to the points A-F on the left: (I) pre-straining the NiTi sheet(A-C), gray arrows indicate direction of applied stress; then deposition of the Ni film at the point (C); (II) heating of the NiTi/Ni stack up to 270K (D) then cooling down to room temperature(D-F-E). Red arrows illustrate expected in-plane strains of the stack relatively to preceding state.

Figure 53 describes the workflow of the experimental work presented in this chapter. First, the NiTi sample is deformed in tension (I), then it is cut in rectangular pieces. At the next step, Ni is deposited on top of NiTi. Figure 53(II) shows the strain measured by digital image correlation (DIC) technique in the NiTi following previous tensile deformation. The measured strain is parallel to the x-axis in the coordinates defined for this study. We performed angle-dependent measurements of M(H) and Mr(φ) at points C, F and E. After measurement at the state C, the sample is heated up to 470K

to overcome elevated temperature of martensite stabilization and so the sample shrinks to its parent austenite phase. Then the sample is cooled to room temperature and measured at point E after heating. As we have shown already in section III.1, tensile deformation induces two-way shape memory effect in the NiTi. Two-way SME, in this case, consists in the sample's elongation after transformation to martensite state and shrinking on the heating to the austenite phase, where it is measured at 400K. Sketches in Figure 53(III) represent the sample at the main steps of the workflow, showing an expected modification of in-plane strains. Note that data in Figure 53(I) and (II) were measured on a sample without Ni layer, to analyze only the NiTi strains in section III.1. Therefore, this data doesn't correspond to the specific specimen measured with magnetometry in this chapter and it has indicative character.

Magnetization versus applied magnetic field measurements of the NiTi/Ni samples pre-stretched up to 3%,5%, and 11% are shown in Figure 54 and compared to the strain-free sample. The magnetic field is applied in the Ni plane, either along pre-strain direction ($\varphi=0°$) or perpendicular to it ($\varphi=90°$). As-deposited samples (first column) has almost no magnetic anisotropy. This result is consistent with the polycrystalline nature of Ni layer as measured by TEM(see Figure 51(b)). Actually, some small differences between 0° and 90° may be seen in the magnified insets in the figure. Corresponding residual magnetization M_r on polar graphs in Figure 54 confirm a very weak anisotropy. Nevertheless, the direction of this as-grown Ni anisotropy seems to randomly vary from sample to sample for all the tested samples.

Strain-free sample ($\varepsilon_{max}=0$) loses completely its weak anisotropy after heating. Both for State E and F, M(H) curves of perpendicular directions are identical and $Mr(\varphi)$ is represented by a circle. On the contrary, peanut-like shape arises in $Mr(\varphi)$ at stage E and F for pre-strained samples (Figure 55). Interestingly, $Mr(\varphi)$ peanut-like shape in E and F states are orthogonal to each other.

Let us now focus on why in state F easy axis (EA) of magnetization lies at $\varphi=0°$, that is parallel to the pre-stretching direction of NiTi whereas at room temperature, in E state, it is perpendicular. Ni possesses negative magnetostriction coefficient λ_s (or positive magnetoelastic coefficient B), which implies that the easy axis tends to be parallel to compressive strain or hard axis is perpendicular to the tensile [11]. Indeed, from sketches in Figure 53(II), we expect compression along the main axis x when the sample is heated from C to D (ε_{OW}). On the other hand, tensile strain along x is expected

when cooling from F to E due to the two-way shape memory effect ε_{TW} induced by pre-stretching.

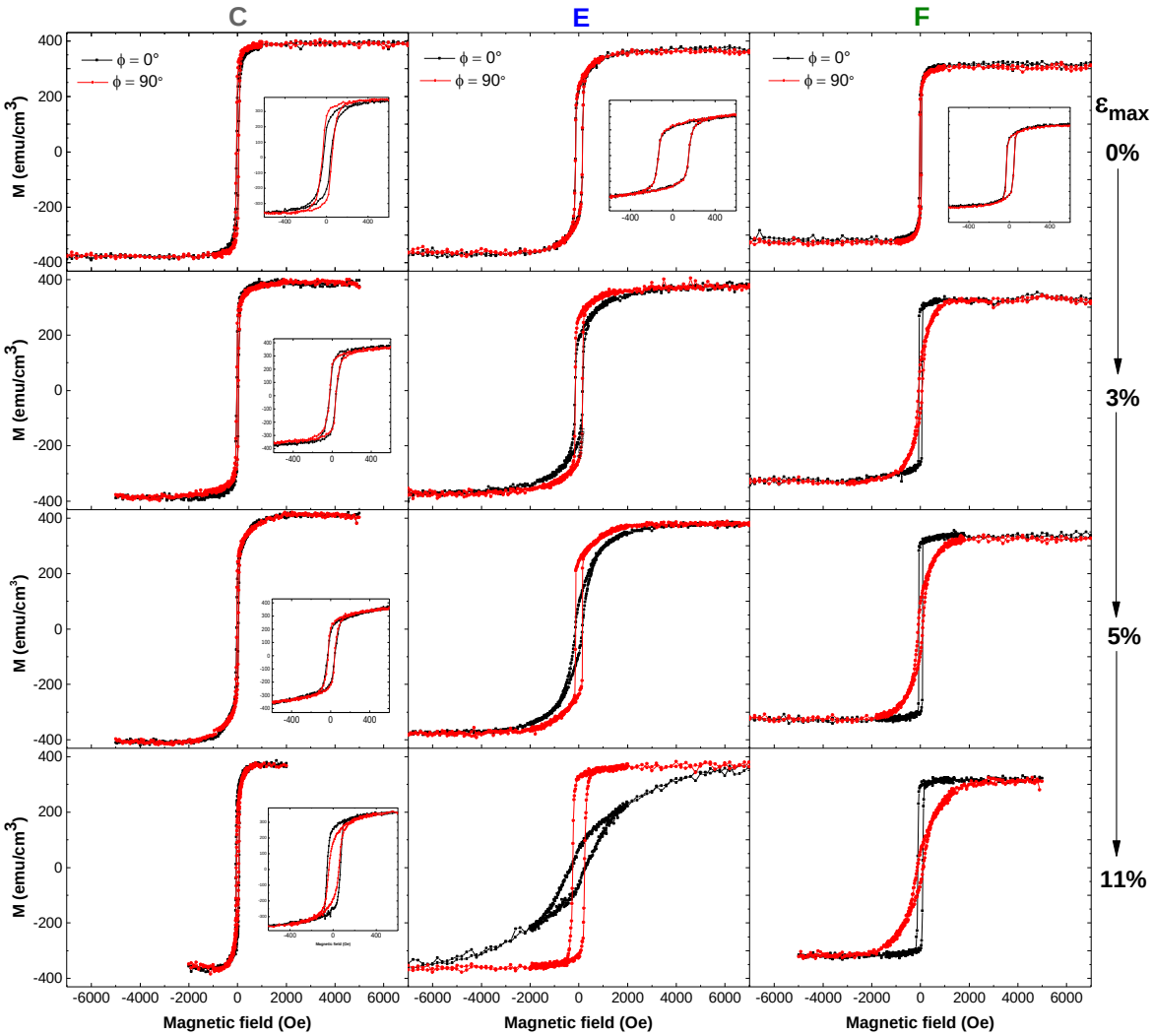

Figure 54. M(H) in-plane measurements in the direction parallel (φ=0°) and perpendicular(φ=90°) to the initial tension of the four representative samples pre-strained to 3%, 5%, 11% and strain-free NiTi/Ni stack (see corresponding strain magnitude on the right side of each row). Three columns correspond to measurements done in the states C, E and F described in Figure 53.

At state E, anisotropy field H_K changes drastically from 1400 Oe to almost 5000 Oe with increasing the pre-stretching amount ε_{max} of NiTi from 3% to 11%. At 400K, in state F, H_K also increases along with ε_{max}, but much more moderately (from 850 Oe just to 1500 Oe). The compressive strain ε_{OW} induced in the film by the first heating (C to D) is always larger than ε_{TW}. Therefore, Ni should be in compressive strain state in both

phases comparing to initial as-deposited state C. It is therefore counterintuitive that anisotropy field of F state is smaller than those of E state.

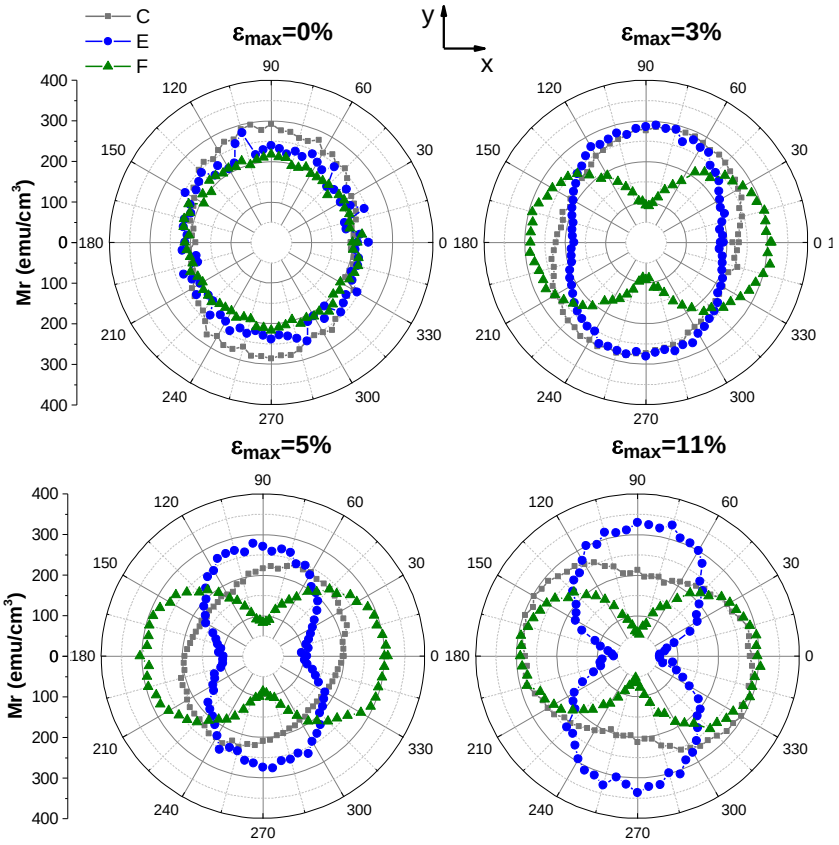

Figure 55. Residual magnetization Mr of the samples presented in Figure 54 as a function of angle φ between pre-strain and magnetic field directions.

Recrystallization and/or structural relaxation of Ni film must occur when the sample is heated from C to D. Several percent of ε_{OW} strain in Ni, may lead to cracking of Ni thin film [11]. Here temperature must favor relaxation. Some evidences of recrystallization of textured polycrystalline Ni at 470K have been found by authors of [143] and micro-strain relaxation at similar low annealing temperatures[144]. In support of the recrystallization of the sample, it was observed that the initial magnetic anisotropy of non-deformed sample disappears after first heating in Figure 54 and even much more pronounced case is shown in Figure 56 . The fact that the magnitude of H_K in F (and the peanut shape) is more or less constant for any ε_{max} above 3% gives also credit to Ni strain relaxation from C to D. Besides, in another set of experiments, Ni was deposited on non-deformed NiTi and only then stretched and measured according to the usual workflow. The results were compared with the NiTi/Ni sample produced in the usual way, when NiTi was stretched before the deposition to the same extent. Magnetic behavior and

anisotropy field are identical to those of NiTi/Ni sample produced in the usual way, where NiTi was stretched before the deposition (see Figure 57). Finally, we can conclude that residual ε_{OW} strains at 470K are responsible for the anisotropy in F state, while anisotropy of state E is governed by ε_{TW}.

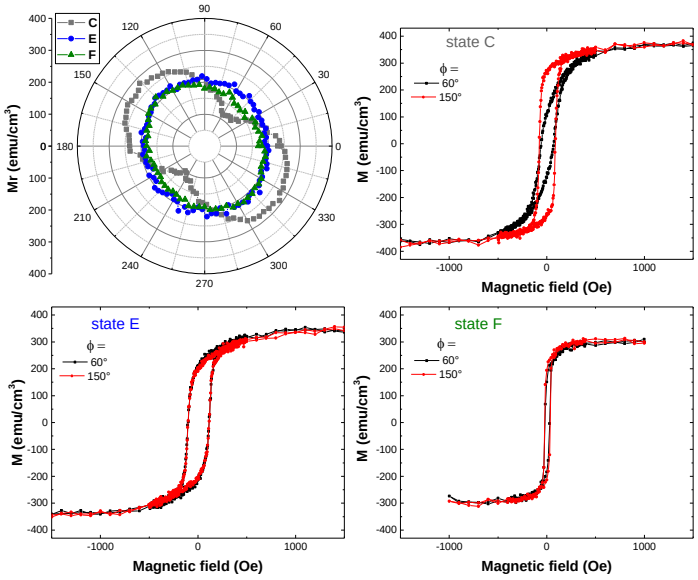

Figure 56. M(H) and Mr measurements of Ni deposited on strain-free NiTi. It demonstrates that initial random magnetic anisotropy of as-deposited Ni vanishes by annealing at 470K.

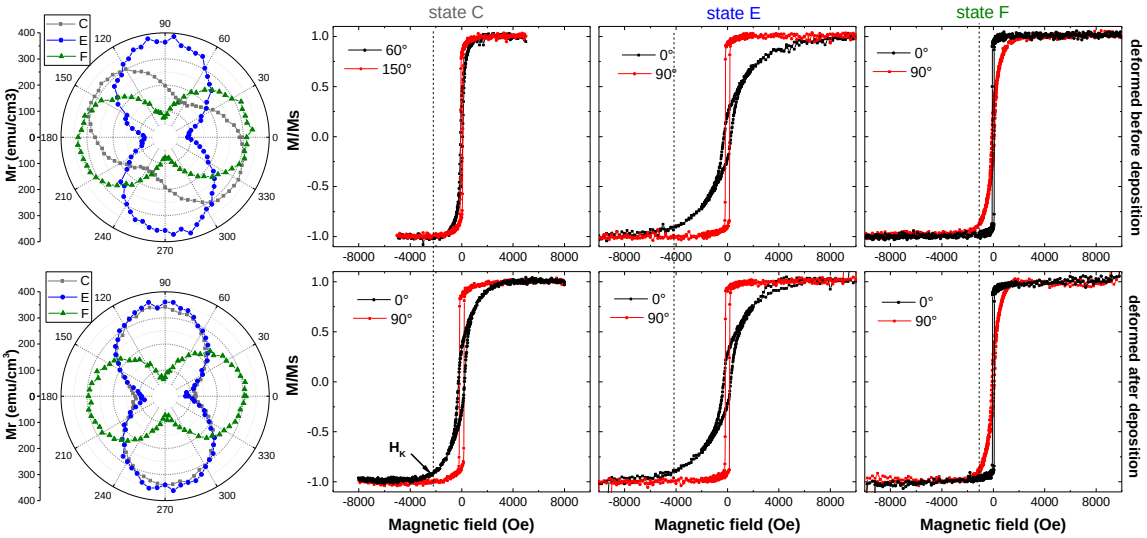

Figure 57. Comparison of the sample pre-deformed before deposition of Ni (usual case) to the sample pre-deformed after Ni deposition to the same amount of ε_{max}, demonstrates that Before state doesn't influence on subsequent states.

Before performing a more quantitative analysis of magnetic anisotropy, we can look on the variation of two other magnetic features that are coercivity H_c and saturation magnetization M_s. From Figure 54 we see that saturation magnetization M_s decreases by 5% after first heating, i.e. in state E comparing to state C. Comparing state E to high temperature state, decrease of M_s in average by 12% regardless amount of strain is observed. The reduction of M_s in temperature is clearly accounted for approaching to Curie temperature. In turn, decrease of M_s in state E comparing to state C probably may be accounted for interdiffusion of Ni into NiTi and/or because of the strain, as it was shown in [6] for FePt. No dependence on strain have been found in our work, while the signs of interdiffusion was observed in TEM and the literature confirms that it occurs on the interface between Ni and Ti even at 450K[145], [146]. Interdiffusion may be coherent with strain relaxation and recrystallization suggested before to happen at high temperature in the system.

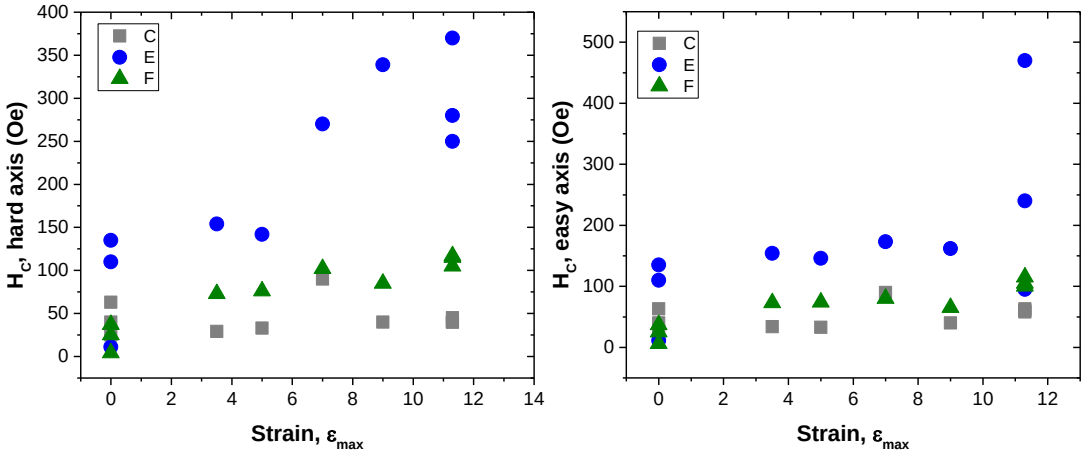

Figure 58. Coercive field of hard axis and easy axis loop as a function of strain.

Coercive field H_c at state E increases with the strain, and it is always larger in 5-10 times than in as-deposited Ni. It is noteworthy, that in 0% strain sample H_c increases as well after heating to the level of 3% and 5% pre-deformation values. It is known from the literature that H_c is one of the parameters that may be tuned with strain, in particular in nickel [27], [147]. However, H_c will not be used further for quantitative characterization, because it is complex parameter, which may depend on interphase, its roughness, thickness, crystallinity, anisotropy distribution etc. NiTi/Ni interphase cannot be compared with commonly studied Si/Ni so it is not reasonable to use H_c in order to evaluate magnetoelasticity of studied stack.

While studying Ni/Pt stack on the NiTi, it was important to make a "control" deposition in the same time on usual Si/SiOx substrate. First of all, M(H) measurements of the Si/Ni at the same stages of the usual workflow as NiTi/Ni in Figure 59, show no magnetic anisotropy in all the states. In contrast to NiTi/Ni, this sample demonstrate decrease of H_C after first heating (between state C and B). Therefore, H_C increase observed in strain-free NiTi/Ni is not related to recrystallization at elevated temperature but apparently to NiTi/Ni interphase particularities, as roughness change or interdiffusion. The presence of interdiffusion in NiTi/Ni also confirming by the fact that Ms doesn't change between the states C and E in Si/Ni.

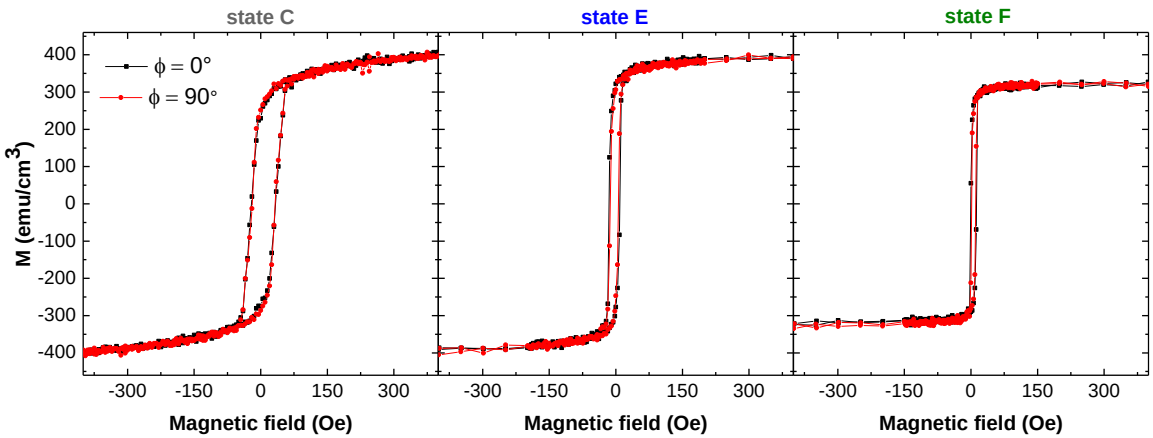

Figure 59. M(H) measurements of the Si/Ni structure, showing no anisotropy at all the stages.

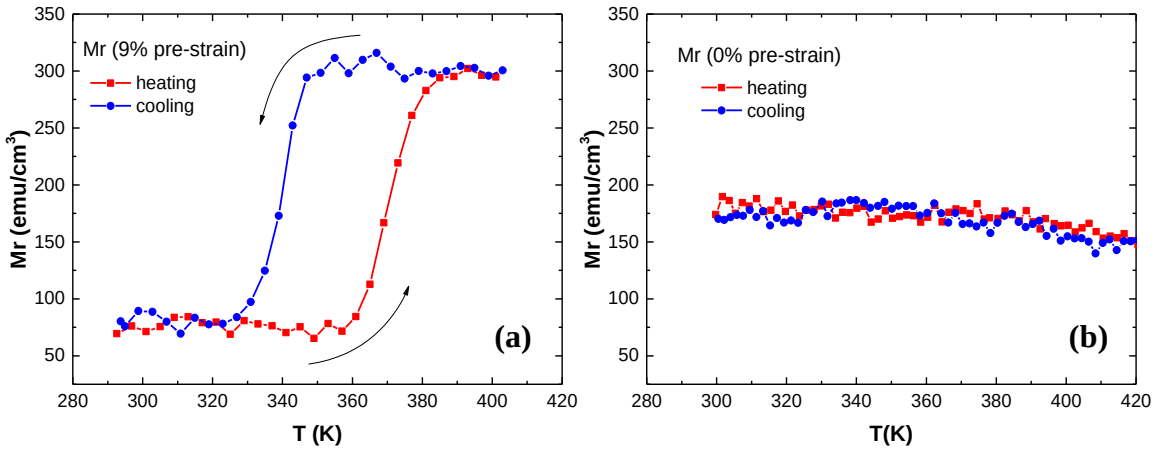

Figure 60. Residual magnetization as a function temperature of the stack deposited on pre-deformed (a) and non-deformed (b) NiTi.

Residual magnetization as a function of temperature of Ni deposited on pre-strained NiTi in Figure 60(a) clearly demonstrates that anisotropy of the Ni, represented by residual magnetization Mr, switches in hysteretic manner according to the

temperatures of martensite transformation in NiTi. Comparison to Mr(T) of deformation-free NiTi in Figure 60(b) proves that there is no additional sources of anisotropy change, characteristic decreases monotonically because of approaching to Ni Curie temperature.

As it is shown by equation (1) magnetoelastic energy is defined by lattice strain of Ni. Apparently, recrystallization and strain relaxation occur in Ni at 470K, hence Ni magnetic anisotropy mostly governed by two-way shape memory effect strains of NiTi. Therefore, discussion of Ni magnetoelasticity should be continued in terms of ε_{TW}, the strain in Ni film should be figured out as well and this question will be examined in the next section.

IV.3. **Quantitative analysis of Ni magnetic anisotropy and strain transfer in NiTi/Ni structure.**

The aim of this section is to understand better magneto-mechanical coupling of the NiTi/Ni structure. In order to do that we will estimate the in-plane strains in NiTi resulted from TWSME, as well as compression after the first heating (one-way SME), then we will calculate expected lattice strains in Ni and compare to NiTi strains.

Looking back to equation (1) of magnetoelastic energy and taking into account polycrystalline untextured structure of Ni, we can assume that the Ni film has isotropic magneto-elastic properties and ε_{zz}, ε_{xy}, ε_{yz}, ε_{zy} are negligibly small compared to ε_{xx} and ε_{yy}. Simplifying designations, in-plane strains ε_{xx} and ε_{yy} will be labeled as ε_x and ε_y according to coordinates in Figure 53(III), magnetoelastic energy simplifies to uniaxial magnetic anisotropy[27] :

$$E_{me} = K_{me}(1 - \alpha_2^2) \tag{5}$$

Where magnetoelastic anisotropy:

$$K_{me} = B(\varepsilon_x - \varepsilon_y); \tag{6}$$

or

$$K_{me} = \frac{3}{2}\lambda_s E(\varepsilon_x - \varepsilon_y); \tag{7}$$

As discussed in the previous chapter, magnetic anisotropy in E state is mostly governed by two-way shape memory effect strains of NiTi. Therefore, discussion of Ni magnetoelasticity should be continued in terms of ε_{TW} while trying to extract the real strains in Ni film transferred from NiTi.

First, magnetic anisotropy energy from anisotropy field H_K is calculated according to the equation:

$$K_U = \frac{1}{2}M_S H_K \tag{8}$$

Anisotropy magnitude in F and E states are presented in Figure 61 as a function of maximum engineering strain ε_{max} in NiTi. Minus sign is assigned to anisotropy favoring a direction of magnetization parallel to the NiTi pre-stretching direction (along x-axis). The magnitude of K_{U_F} at high-temperature phase is greatly smaller than at E state. Anisotropy energy observed in austenite phase changes just from $-1.3\cdot10^5$ to $-2.3\cdot10^5$ erg/cm^3 in contrast to 2.5 to $10\cdot10^5$ erg/cm^3 at state E. Such large difference in absolute values cannot be accounted just for Ni magnetic anisotropy energy temperature dependence, which leads to reduction by 20% from 300 to 400K [25].

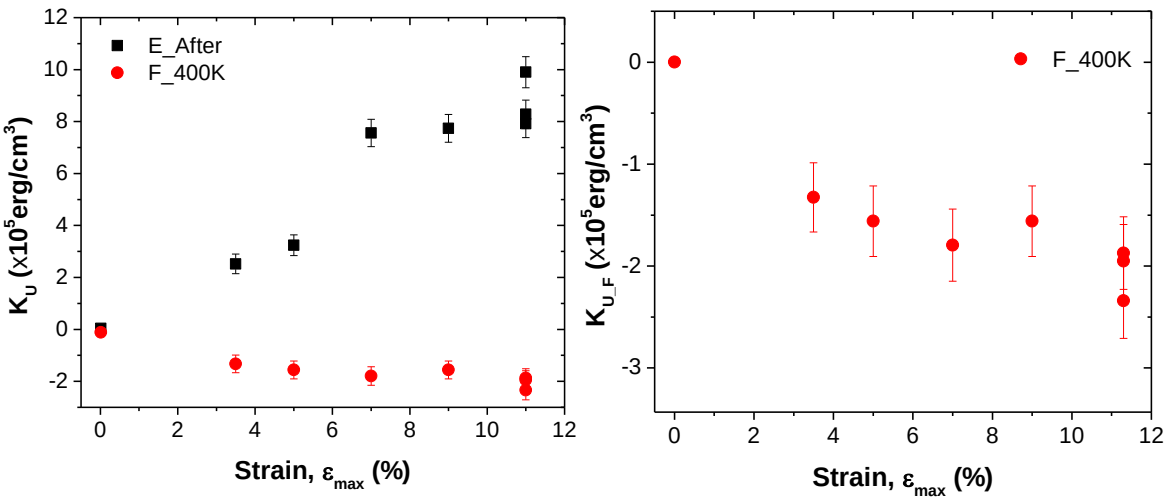

Figure 61. In-plane anisotropy energy as a function of NiTi pre-strain; on the right the plot of anisotropy at high temperature is plotted on a smaller scale.

At the next step, in-plane strains ε_{TW} and ε_{OW} in NiTi due to the two-way and one-way shape memory effect respectively are evaluated. Because of the current technical limits of our DIC sept up, only one DIC experiment was successfully performed in order to measure NiTi strain variation while sweeping temperature. It was presented in Figure 53 for ε_{max} = 7% in B (i.e. for ε_{res_x}=6.2% in C). In Figure 53, only axial strain along the x-axis is shown. Both in-plane strains are shown in Figure 62. The other NiTi substrates used for Ni deposition were stretched without DIC, so we know only engineering strains ε_{res} and $\varepsilon_{max,}$ the latter was indicated as the amount of pre-deformation in the previous section. The correlation between real local strains ε_{Est_max} and ε_{Est_res} in the central part of the NiTi ribbon measured by DIC technique and the engineering strains by tensile machine was established in section III.1. To further estimate axial strains ε_{TW_x} and ε_{OW_x} for other pre-deformation values, the paper of Liu et al.[43] was used where authors investigated a two-way shape memory effect in NiTi induced by pre-stretching. This paper was selected because the amount of ε_{TW_x} obtained in our experiment was almost identical to one obtained in the paper: ε_{TW_x} =1.4% and ε_{OW_x} =4.9% at ε_{res_x}=6.2% in the paper of Liu and ε_{TW_x} =1.3% and ε_{OW_x} =4.9% at ε_{res_x}=6.2%.

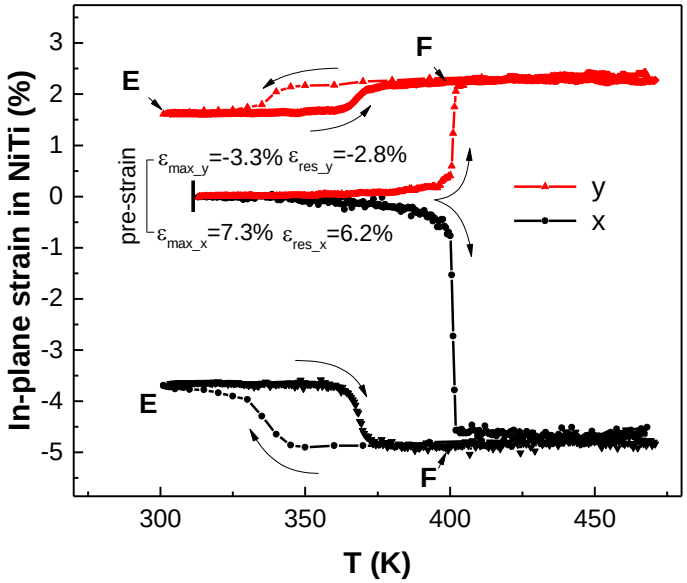

Figure 62. Axial(x) and transversal (y) strains of the sample pre-deformed in tension (ε_{max}) during two consecutive thermal cycles.

Concerning transversal strains in NiTi, the ratio between axial and transversal strain $\frac{\varepsilon_y}{\varepsilon_x} \approx 0.43$ was found during all our DIC measurements as a function of temperature for different tensile strain amplitudes. This value is different from NiTi Poisson's ratio (0.33) since Poisson's ratio only characterizes elastic deformation whereas we are working here with strain above 1% (limit of the elastic regime). The resulted strains estimated by the procedures stated above presented in.

Table 3. Estimated strains in NiTi.

$\varepsilon_{E\_max\_x}$ [%]	$\varepsilon_{Est\_max\_x}$ [%]	$\varepsilon_{E\_res\_x}$ [%]	$\varepsilon_{Est\_res\_x}$ [%]	ε_x^{tw} [%]	ε_y^{tw} [%]	ε_x^{tw}- ε_y^{tw} [%]	ε_x^{ow}- ε_y^{ow} [%]
maximal engineering	*maximal estimated*	*residual engineering*	*residual estimated*	*TWSME axial strain*	*TWSME transversal strain*	*TWSME in-plane strain*	*OWSME in-plane strain*
11.3	9.8	9	7.5	1.9	-0.82	2.72	7.25
9	7.6	7.5	5.8	1.35	-0.58	1.93	6.09
7	6.3	6	4.9	1.1	-0.47	1.57	5.22
5	4.6	4.3	3.3	0.65	-0.28	0.93	3.9
3.5	3	3	2.4	0.4	-0.17	0.57	2.9

As Ni film in our experiment is polycrystalline and shows no magnetic anisotropy after first heating, we can conclude that its anisotropy is defined by strain propagated from NiTi, hence anisotropy energy K_U calculated in the previous section can be considered as only magnetoelastic anisotropy energy K_{me}. The out-of-plane contribution

is not considered here, as well as shape anisotropy. From this perspective lattice strain of Ni can be defined as a function of $K_{U.}$ It is usually preferable to measure the lattice strains directly and to define then magnetoelastic coupling coefficient or saturation magnetostriction because these values vary depending on the structure, its interface, etc. Unfortunately, it was not feasible to access the Ni lattice by means of XRD in the present study, so the average magnetoelastic constants for polycrystalline samples will be used to estimate the lattice strain of Ni.

The difference between thin films and bulk magnetostriction of polycrystalline Ni was observed [148],[27],[22] by different authors. However, different sources report usually slightly smaller saturation magnetostriction λ_s in thin films, which can be as large as $-2.2\cdot10^{-5}$ [27] in contrast to average $-3.6\cdot10^{-5}$ [149]–[151] in bulk polycrystal. Figure 63(a) shows the Ni in-plane strain (ε_x^{Ni}- ε_y^{Ni}) in E state, calculated for the $\lambda_s = -2.2\cdot10^{-5}$ and for the average bulk $\lambda_s = -3.6\cdot10^{-5}$, in order to have an idea about possible divergence, plotted versus TWSME NiTi in-plane strain (ε_x^{tw}- ε_y^{tw}) from Table 3.

In the case of high temperature state F, it was reported that Ni saturation magnetostriction decreases by 16-20% from 300K to 400K, thus λ_s equal to $1.8\cdot10^{-5}$ and $3\cdot10^{-5}$ were taken to calculate the Ni strain in Figure 63(b). Young's modulus E of Ni taken for calculation is 200 GPa for room temperature and for high temperature phase is 196 GPa to take into account though weak but known reduction of elastic modulus in temperature[144]. For room temperature anisotropy, thin film λ_s provides the average value of strain propagation (ε_x^{Ni}- ε_y^{Ni})/(ε_x^{tw}- ε_y^{tw}) equal to 0.55 while for the bulk value it is around 0.33. The latter ratio is not far from the one found in NiTiNb(0.5mm)/FePt(10-20nm) bilayer[4]. However, comparison to the (ε_x^{Ni}- ε_y^{Ni}) value deduced from TEM (see Figure 52 in section IV.1) suggests even larger strain transmission ratio. Thus for the sample with (ε_x^{tw}- ε_y^{tw}) = 1.6%, TEM gives 1.3% in contrast to 0.75%-1.15% estimated from anisotropy magnitude. Unfortunately, only the one single TEM measurement was possible to perform in the frame of this study, so from the point of view of statistical significance, we cannot say that the 1.3% is the most realistic value. Nevertheless, it reinforces the validity of the upper border of strain in Figure 63(a) and suggests that we have magnetostriction value close to one observed in Ni thin films.

As we can see, expected average Ni lattice strain variates from -0.15% to -0.4%, which is in ~3 times smaller than corresponding values in room temperature. As it was concluded in the previous section, magnetic anisotropy at 400K is probably results from

residual compression strain, that remained after recrystallization. Estimation that the strains ratio is expected to be the same as in room temperature suggests that about 10% of compressive strain upon first heating remains.

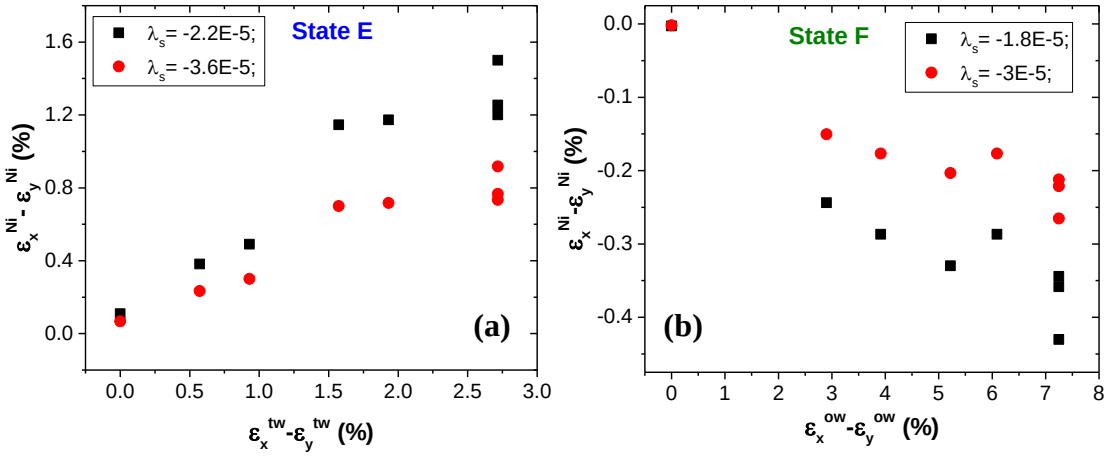

Figure 63. In-plane lattice strains in Ni (ε_x - ε_y) at low temperature state E (a) and high temperature state F (b) calculated from anisotropy energy for minimum and maximum λ_s versus expected NiTi two-way (a) and one-way (b) shape memory effect strain.

One of the reasons of strain transmission ratio reduction is the difference in Young's modulus between the substrate and the film[152]. In martensite phase of NiTi it is equal to 75-83 GPa and to 28-40 GPa in austenite, while for Ni this quantity is around 200 GPa. It means that the same uniaxial stress causes much smaller strain in Ni than in NiTi. However, this parameter characterizes material only in the linear elasticity regime, as well as Poisson's ratio, which mismatch also decreases magnetoelastic coupling. Not less important the quality of the interface, lattice matching between Ni and NiTi lattices. TEM images show that NiTiO phase in order of 10 nanometres exists at the interface between NiTi and Ni. Such intermediate layer must affect the strain transfer. Another potential limitation is change of surface roughness, related to the phase transformation, it may contribute to non-uniformity of strain transfer.

Summary

Coupling between strain from NiTi shape memory alloy and magnetic properties of Ni was explored in the chapter. 20nm of Ni was deposited by physical vapor deposition on pre-stretched NiTi substrates and capped with 5nm of Pt. NiTi/Ni structure was studied by atomic(magnetic) force microscopy and transmission electron microscopy.

The Ni layer is continuous and not damaged after strain release. Elemental-sensitive analysis revealed the 10nm thin Ti-rich oxidized level at the top of NiTi surface, which works as the buffer layer between Ni and NiTi.

The range of angle-sensitive in-plane magnetic measurements were done as the function of temperature. The induction and switching of the magnetic anisotropy are achieved in Ni thin film by means of thermally induced strain from NiTi. As-deposited Ni films are quasi-isotropic and untextured. However, as high as $1 \cdot 10^6$ erg/cm^3 uniaxial magnetic anisotropy is attained upon thermal sweeping, which is the largest value to our knowledge in the literature. We demonstrated reproducible switching of Ni anisotropy by 90° when going from room temperature to 400K, and vice-versa. In the present configuration, induced magnetic anisotropy in 2-4 times smaller at high temperature phase then at room temperature.

The strain propagation from NiTi to Ni layer was carefully estimated and verified with lattice strain in Ni extracted from TEM. We approximately calculated the average transmission ratio of strain from NiTi to Ni in range of 0.6. It is a promising result since many parameters such as lattice matching, ferromagnet thickness, NiTi TWSME amplitude or NiTi roughness, can be improved. Smaller anisotropy change at high temperature is mainly accounted for the first heating up to 480K and may be changed by tuning of transformation temperatures and/or deposition at the different stage of thermo-mechanical treatment. Besides, present experiments demonstrate the feasibility of the temperature threshold sensor, which was introduced in the beginning of the dissertation as one of the starting ideas for the study.

Conclusions and perspectives

This thesis consists of two general parts, in the first part we investigated paramagnetic and structural properties of NiTi, while in the second magnetoelastic coupling in NiTi/Ni bilayer. Conclusion of this study are grouped and presented in logical order:

- Magnetization versus temperature measurements reflects B2-R-B19' and B19'-B2 transformation and their transition temperatures. Magnetometry visualizes some features as temperature memory effect, change of the transition path or relative amount of each phase. Tensile deformation of NiTi strongly affects its magnetic susceptibility. Magnetic susceptibility χ of as-deformed NiTi decreases, while after thermal transformation susceptibility of newly accommodated martensite increases comparing to non-deformed material.
- At the crystal lattice scale, NiTi system reacts on applied stress in the martensite phase by [001] (including, but not exclusively) preferred reorientation and shear-like distortion. Lattice distortion is mainly characterized by the increase of monoclinic angle β proportionally to tensile strain magnitude. The same, but inversed tendency of lattice distortion was found in newly accommodated martensite after thermal transformation and in non-deformed NiTi on heating from 100K to 300K.
- Density of states at Fermi energy $D(E_f)$ in both phases, as well as deformation and temperature-induced changes in $D(E_f)$ are related to experimentally observed magnetic susceptibilities, reinforcing assumption about Pauli paramagnetism of NiTi. However, some important contributions are discussed, which are not included in the model but result in divergence between calculated and observed values of magnetic susceptibility.
- Shape memory effect in NiTi is effective to induct and reproducibly switch by 90° the uniaxial magnetic anisotropy in Ni thin film as a function of temperature. As high as $1 \cdot 10^5$ J/m^3 uniaxial magnetic anisotropy is attained in previously untextured Ni film, which is the largest value on our knowledge in the literature. The average transmission ratio of strain from NiTi to Ni is estimated to lie in the range of 0.6. It is a promising result since many

parameters such as lattice matching, ferromagnet thickness, NiTi TWSME amplitude or NiTi roughness, can be improved.

Perspectives

We believe this study allows us to conclude that shape memory effect is the purely thermoelastic non-volatile effect, that can efficiently introduce tensile or compressive deformation to coupled ferromagnetic layer, depending on NiTi phase and the stage when Ni is deposited. Taking into account the possibility to tune the characteristic temperatures and hysteresis width of martensite transformation in NiTi-based alloys together with tuning the amount of strain released upon this transformation, makes this approach promising for the range of technologies and opens the road (together with previous studies of NiTiNb/FePt or Fe [4]–[6]) to the numerous application-oriented studies.

Controlling or inducing out-of-plane anisotropy by shape memory effect looks promising since out-of-plane anisotropy is more interesting for potential applications in memory or information technologies. Another perspective is the studying of time scale limits of shape memory effect induction. For now, the best results on our knowledge were attained by current pulses, and they are in the range of tens of μs. Therefore, the possibility of ultrafast optical switching may attract great attention of scientific society. Switching of magnetic anisotropy or other electrical or transport properties at the picosecond scale looks feasible if one imagines SMA-based device at the micrometer scale or less, especially when SMA is the single crystal. Moreover, utilization of naturally produced heat or heat, which is the secondary output of the system, as an actuation force, may open many sensing applications. In particular, the presented results demonstrate the feasibility of the non-volatile temperature threshold sensor, that irreversibly switches its magnetic anisotropy when the threshold temperature is exceeded. This sensor was one of the starting ideas for the study.

Concerning the continuation of the research on NiTi itself, grain boundaries produce additional constraints and add uncertainty in the study. Hence, experiments on the single crystal should reinforce or doubt our conclusions about the common structural changes resulted from tensile deformation, and its influence on magnetic susceptibility. Also, the model of magnetic susceptibility used in the work may be extended. For example, lattice parameters used for calculations should be extracted from all the plane

orientations, to take into account anisotropic stress. Twin junctions and dislocations are anticipated to change atomic positions in the lattice[62], thereby this may be included into the calculations. Exchange enhancement and many-body effects contribution to magnetic susceptibility may be verified experimentally by measuring effective mass using angle-resolved photoemission, for example.

Appendix

A.

The experimental errors and the error bars (error bars used in the Chapter III).

Magnetic susceptibility measurement error:

- In studied samples geometry factor variates depending on dimensions in range from 0.97 to 1.035 = +/-3%. Size of the sample changes also before and after heating as a result of shape memory effect. Resulted geometry factor depends on the amount of strain and reaches +/-5% at maximum strains.
- Initial stress state of the sample is not always the same, magnetic susceptibility change $\Delta\chi$ of non-strained samples after first heating is not always 0. Average deflection for non-strained samples is 0.02E-6 emu/g*Oe.
    - The error for all type of $\Delta\chi$ is 0.02 which corresponds to the average deviation for 0 strain samples between 1st and 2nd thermal cycle in addition to 5% of the $\Delta\chi$ value, as explained above.
- Strain measurement error, deformation dispersion defined before for the samples deformed without DIC in section III.1. Hysteresis of the first batch of the samples is much wider (roughly 38 vs 30K).
    - The final error bar for strain is the values defined in section III.1 and +3% from the strain magnitude.
- Temperature measurement error: 2K, as an average deflection of transformation temperatures from one to another measurement + 3% from ΔT value. The latter is coming from the fact that when pre-strain increases, transformation path to austenite phase elongates because of martensite stabilization effect upon heating, and it complicates defining the actual transformation temperatures.
- All the sample that have been broken during the tensile deformation, have atypical $\Delta\chi$, ΔT and XRD results, which deflect from other samples. It may be explained by strain localization and nonhomogeneous deformation or/and the “after” state is different when unloading is not monotonical progression but an abrupt release.

Bibliography

[1] D. C. Lagoudas, Ed., *Shape memory alloys: modeling and engineering applications*. New York, NY: Springer, 2008.

[2] G. Siekmeyer, A. Schüßler, R. L. de Miranda, and E. Quandt, "Comparison of the Fatigue Performance of Commercially Produced Nitinol Samples versus Sputter-Deposited Nitinol," *J. Mater. Eng. Perform.*, vol. 23, no. 7, pp. 2437–2445, Jul. 2014, doi: 10.1007/s11665-014-1101-x.

[3] C. Bechtold, R. L. de Miranda, C. Chluba, and E. Quandt, "Fabrication of self-expandable NiTi thin film devices with micro-electrode array for bioelectric sensing, stimulation and ablation," *Biomed. Microdevices*, vol. 18, no. 6, p. 106, Dec. 2016, doi: 10.1007/s10544-016-0131-6.

[4] C. Feng *et al.*, "Reversible and Nonvolatile Modulations of Magnetization Switching Characteristic and Domain Configuration in L10-FePt Films via Nonelectrically Controlled Strain Engineering," *ACS Appl. Mater. Interfaces*, vol. 8, no. 11, pp. 7545–7552, Mar. 2016, doi: 10.1021/acsami.5b12699.

[5] C. Feng *et al.*, "Thickness-dependent electronic structure modulation of ferromagnetic films on shape memory alloy substrates based on a pure strain effect," *Appl. Phys. Lett.*, vol. 109, no. 21, p. 212401, Nov. 2016, doi: 10.1063/1.4967996.

[6] C. Feng *et al.*, "Nonvolatile modulation of electronic structure and correlative magnetism of L10-FePt films using significant strain induced by shape memory substrates," *Sci. Rep.*, vol. 6, no. 1, Apr. 2016, doi: 10.1038/srep20199.

[7] C. A. F. Vaz, J. A. C. Bland, and G. Lauhoff, "Magnetism in ultrathin film structures," *Rep. Prog. Phys.*, vol. 71, no. 5, p. 056501, May 2008, doi: 10.1088/0034-4885/71/5/056501.

[8] U. Gradmann and J. Müller, "Flat Ferromagnetic, Epitaxial 48Ni/52Fe(111) Films of few Atomic Layers," *Phys. Status Solidi B*, vol. 27, no. 1, pp. 313–324, 1968, doi: 10.1002/pssb.19680270133.

[9] J. B. Staunton *et al.*, "Temperature Dependent Magnetic Anisotropy in Metallic Magnets from an Ab Initio Electronic Structure Theory: L10-Ordered FePt," *Phys. Rev. Lett.*, vol. 93, no. 25, p. 257204, Dec. 2004, doi: 10.1103/PhysRevLett.93.257204.

[10] T. Burkert *et al.*, "Magnetic anisotropy of L 1 0 FePt and Fe 1−x Mnx Pt," *Phys. Rev. B*, vol. 71, no. 13, p. 134411, Apr. 2005, doi: 10.1103/PhysRevB.71.134411.

[11] D. Sander, "The correlation between mechanical stress and magnetic anisotropy in ultrathin films," *Rep. Prog. Phys.*, vol. 62, no. 5, pp. 809–858, May 1999, doi: 10.1088/0034-4885/62/5/204.

[12] K. Ha and R. C. O'Handley, "Nonlinear magnetoelastic anisotropy in Cu/Ni/Cu/Si(001) films," *J. Appl. Phys.*, vol. 85, no. 8, pp. 5282–5284, Apr. 1999, doi: 10.1063/1.369855.

[13] E. Bauer, "Growth of thin films," *J. Phys. Condens. Matter*, vol. 11, no. 48, pp. 9365–9385, Nov. 1999, doi: 10.1088/0953-8984/11/48/303.

[14] C. Song, B. Cui, F. Li, X. Zhou, and F. Pan, "Recent progress in voltage control of magnetism: Materials, mechanisms, and performance," *Prog. Mater. Sci.*, vol. 87, pp. 33–82, Jun. 2017, doi: 10.1016/j.pmatsci.2017.02.002.

[15] C. A. F. Vaz *et al.*, "Origin of the magnetoelectric coupling effect in Pb(Zr0.2Ti0.8)O3/La0.8Sr0.2MnO3 multiferroic heterostructures," *Phys. Rev. Lett.*, vol. 104, no. 12, p. 127202, Mar. 2010, doi: 10.1103/PhysRevLett.104.127202.

[16] T. Maruyama *et al.*, "Large voltage-induced magnetic anisotropy change in a few atomic layers of iron," *Nat. Nanotechnol.*, vol. 4, no. 3, pp. 158–161, Mar. 2009, doi: 10.1038/nnano.2008.406.

[17] M. Endo, S. Kanai, S. Ikeda, F. Matsukura, and H. Ohno, "Electric-field effects on thickness dependent magnetic anisotropy of sputtered MgO/Co40Fe40B20/Ta structures," *Appl. Phys. Lett.*, vol. 96, no. 21, p. 212503, May 2010, doi: 10.1063/1.3429592.

[18] F. Matsukura, Y. Tokura, and H. Ohno, "Control of magnetism by electric fields," *Nat. Nanotechnol.*, vol. 10, no. 3, pp. 209–220, Mar. 2015, doi: 10.1038/nnano.2015.22.

[19] A. A. Bukharaev, A. K. Zvezdin, A. P. Pyatakov, and Y. K. Fetisov, "Straintronics: a new trend in micro- and nanoelectronics and materials science," *Phys.-Uspekhi*, vol. 61, no. 12, p. 1175, Dec. 2018, doi: 10.3367/UFNe.2018.01.038279.

[20] T. Brintlinger *et al.*, "In Situ Observation of Reversible Nanomagnetic Switching Induced by Electric Fields," *Nano Lett.*, vol. 10, no. 4, pp. 1219–1223, Apr. 2010, doi: 10.1021/nl9036406.

[21] M. Staruch *et al.*, "Reversible strain control of magnetic anisotropy in magnetoelectric heterostructures at room temperature," *Sci. Rep.*, vol. 6, p. 37429, Nov. 2016, doi: 10.1038/srep37429.

[22] S. Finizio *et al.*, "Magnetic Anisotropy Engineering in Thin Film Ni Nanostructures by Magnetoelastic Coupling," *Phys. Rev. Appl.*, vol. 1, no. 2, p. 021001, Mar. 2014, doi: 10.1103/PhysRevApplied.1.021001.

[23] K. Roy, S. Bandyopadhyay, and J. Atulasimha, "Hybrid spintronics and straintronics: A magnetic technology for ultra low energy computing and signal processing," *Appl. Phys. Lett.*, vol. 99, no. 6, p. 063108, Aug. 2011, doi: 10.1063/1.3624900.

[24] M. Barangi and P. Mazumder, "Straintronics: A leap toward ultimate energy efficiency of magnetic random access memories.," *IEEE Nanotechnol. Mag.*, vol. 9, no. 3, pp. 15–24, Sep. 2015, doi: 10.1109/MNANO.2015.2441106.

[25] M. Barangi and P. Mazumder, "Effect of temperature variations and thermal noise on the static and dynamic behavior of straintronics devices," *J. Appl. Phys.*, vol. 118, no. 17, p. 173902, Nov. 2015, doi: 10.1063/1.4934566.

[26] Q. Wang, J. Domann, G. Yu, A. Barra, K. L. Wang, and G. P. Carman, "Strain-Mediated Spin-Orbit-Torque Switching for Magnetic Memory," *Phys. Rev. Appl.*, vol. 10, no. 3, p. 034052, Sep. 2018, doi: 10.1103/PhysRevApplied.10.034052.

[27] A. Bur *et al.*, "Strain-induced magnetization change in patterned ferromagnetic nickel nanostructures," *J. Appl. Phys.*, vol. 109, no. 12, p. 123903, Jun. 2011, doi: 10.1063/1.3592344.

[28] J. Åkerman, "Toward a Universal Memory," *Science*, vol. 308, no. 5721, pp. 508–510, Apr. 2005, doi: 10.1126/science.1110549.

[29] D. Sander *et al.*, "The 2017 Magnetism Roadmap," *J. Phys. Appl. Phys.*, vol. 50, no. 36, p. 363001, Aug. 2017, doi: 10.1088/1361-6463/aa81a1.

[30] M. Re, "HAMR: the Next Leap Forward is Now," *Seagate Blog*, 23-Oct-2017. [Online]. Available: https://blog.seagate.com/craftsman-ship/hamr-next-leap-forward-now/. [Accessed: 27-Sep-2019].

[31] Seagate, "HAMR Technology," *https://www.seagate.com/www-content/ti-dm/tech-insights/en-us/docs/TP707-1-1712US_HAMR.pdf.* .

[32] L. H. Lewis, C. H. Marrows, and S. Langridge, “Coupled magnetic, structural, and electronic phase transitions in FeRh,” *J. Phys. Appl. Phys.*, vol. 49, no. 32, p. 323002, Jul. 2016, doi: 10.1088/0022-3727/49/32/323002.

[33] J. Mohd Jani, M. Leary, A. Subic, and M. A. Gibson, “A review of shape memory alloy research, applications and opportunities,” *Mater. Des. 1980-2015*, vol. 56, pp. 1078–1113, Apr. 2014, doi: 10.1016/j.matdes.2013.11.084.

[34] M. Kohl, *Shape Memory Microactuators*. Berlin Heidelberg: Springer-Verlag, 2004.

[35] Y. Fu, H. Du, W. Huang, S. Zhang, and M. Hu, “TiNi-based thin films in MEMS applications: a review,” *Sens. Actuators Phys.*, vol. 112, no. 2–3, pp. 395–408, May 2004, doi: 10.1016/j.sna.2004.02.019.

[36] L. Petrini and F. Migliavacca, “Biomedical Applications of Shape Memory Alloys,” *J. Metall.*, 2011, doi: 10.1155/2011/501483.

[37] N. B. Morgan, “Medical shape memory alloy applications--the market and its products,” *Mater. Sci. Eng. Struct. Mater. Prop. Microstruct. Process.*, vol. 378, no. 1–2, pp. 16–23, 2003, doi: 10.1016/j.msea.2003.10.326.

[38] D. Stoeckel, “Shape memory actuators for automotive applications,” *Mater. Des.*, vol. 11, no. 6, pp. 302–307, Dec. 1990, doi: 10.1016/0261-3069(90)90013-A.

[39] D. J. Hartl and D. C. Lagoudas, “Aerospace applications of shape memory alloys,” *Proc. Inst. Mech. Eng. Part G J. Aerosp. Eng.*, vol. 221, no. 4, pp. 535–552, Apr. 2007, doi: 10.1243/09544100JAERO211.

[40] T. Hauet, O. Hellwig, and L. Huang, “System, method and apparatus for strain-assisted magnetic recording for controlling switching field and tightening switching field distribution in bit patterned media,” US8129043B2, 06-Mar-2012.

[41] G. B. KAUFFMAN and I. MAYO, “The Story of Nitinol: The Serendipitous Discovery of the Memory Metal and Its Applications,” *Chem. Educ.*, vol. 2, no. 2, pp. 1–21, Jun. 1997, doi: 10.1007/s00897970111a.

[42] O. Benafan, S. A. Padula, R. D. Noebe, T. A. Sisneros, and R. Vaidyanathan, “Role of B19′ martensite deformation in stabilizing two-way shape memory behavior in NiTi,” *J. Appl. Phys.*, vol. 112, no. 9, p. 093510, Nov. 2012, doi: 10.1063/1.4764313.

[43] Y. Liu, Y. Liu, and J. Van Humbeeck, “Two-way shape memory effect developed by martensite deformation in NiTi,” *Acta Mater.*, vol. 47, no. 1, pp. 199–209, Dec. 1998, doi: 10.1016/S1359-6454(98)00325-5.

[44] H. Hou, R. F. Hamilton, and M. W. Horn, “Narrow thermal hysteresis of NiTi shape memory alloy thin films with submicrometer thickness,” *J. Vac. Sci. Technol. A*, vol. 34, no. 5, p. 050602, Jul. 2016, doi: 10.1116/1.4959567.

[45] E. Patoor, D. C. Lagoudas, P. B. Entchev, L. C. Brinson, and X. Gao, “Shape memory alloys, Part I: General properties and modeling of single crystals,” *Mech. Mater.*, vol. 38, no. 5–6, pp. 391–429, May 2006, doi: 10.1016/j.mechmat.2005.05.027.

[46] C.-Y. Nien, H.-K. Wang, C.-H. Chen, S. Ii, S.-K. Wu, and C.-H. Hsueh, “Superelasticity of TiNi-based shape memory alloys at micro/nanoscale,” *J. Mater. Res.*, vol. 29, no. 22, pp. 2717–2726, Nov. 2014, doi: 10.1557/jmr.2014.322.

[47] A. E. Volkov, W. Miszuris, and N. A. Volkova, “Strain Recovery by TiNi Element Under Fast Heating,” *Shape Mem. Superelasticity*, vol. 4, no. 1, pp. 256–263, Mar. 2018, doi: 10.1007/s40830-017-0138-8.

[48] K. Yamauchi, I. Ohkata, K. Tsuchiya, and S. Miyazaki, *Shape memory and superelastic alloys*. Woodhead Publishing Limited, 2011.

[49] J. Frenzel, A. Wieczorek, I. Opahle, B. Maass, R. Drautz, and G. Eggeler, "On the effect of alloy composition on martensite start temperatures and latent heats in Ni–Ti-based shape memory alloys," 2015, doi: 10.1016/j.actamat.2015.02.029.

[50] S. Kibey, H. Sehitoglu, and D. D. Johnson, "Energy landscape for martensitic phase transformation in shape memory NiTi," *Acta Mater.*, vol. 57, no. 5, pp. 1624–1629, Mar. 2009, doi: 10.1016/j.actamat.2008.12.008.

[51] S. D. Prokoshkin, A. V. Korotitskiy, V. Brailovski, S. Turenne, I. Yu. Khmelevskaya, and I. B. Trubitsyna, "On the lattice parameters of phases in binary Ti–Ni shape memory alloys," *Acta Mater.*, vol. 52, no. 15, pp. 4479–4492, Sep. 2004, doi: 10.1016/j.actamat.2004.06.007.

[52] H. C. Ling and R. Kaplow, "Macroscopic length changes during the B2 ⇆ R and M → B2 transitions in equiatomic Ni□Ti alloys," *Mater. Sci. Eng.*, vol. 51, no. 2, pp. 193–201, Dec. 1981, doi: 10.1016/0025-5416(81)90195-6.

[53] S. Miyazaki and K. Otsuka, "Deformation and transition behavior associated with theR-phase in Ti-Ni alloys," *Metall. Trans. A*, vol. 17, no. 1, pp. 53–63, Jan. 1986, doi: 10.1007/BF02644442.

[54] C. Urbina, F. Gispert-Guirado, F. Ferrando, and S. De la Flor, "Quantitative analysis of the microstructure in NiTi wires by Synchrotron X-ray diffraction: An approach to the cause of the Two Way Shape Memory Effect," *J. Alloys Compd.*, vol. 712, pp. 833–847, Jul. 2017, doi: 10.1016/j.jallcom.2017.04.071.

[55] P. Y. Manach and D. Favier, "Origin of the two-way memory effect in NiTi shape memory alloys," *Scr. Metall. Mater.*, vol. 28, no. 11, pp. 1417–1421, Jun. 1993, doi: 10.1016/0956-716X(93)90492-B.

[56] K. Otsuka and X. Ren, "Physical metallurgy of Ti–Ni-based shape memory alloys," *Prog. Mater. Sci.*, vol. 50, no. 5, pp. 511–678, Jul. 2005, doi: 10.1016/j.pmatsci.2004.10.001.

[57] Eleonora Zanaboni, "One Way and Two Way–Shape Memory Effect: Thermo–Mechanical Characterization of Ni–Ti wires," Universita degli Studi di Pavia, 2008.

[58] X. M. Zhang, J. Fernandez, and J. M. Guilemany, "Role of external applied stress on the two-way shape memory effect," *Mater. Sci. Eng. A*, vol. 438–440, pp. 431–435, Nov. 2006, doi: 10.1016/j.msea.2006.02.093.

[59] A. P. Stebner *et al.*, "Micromechanical quantification of elastic, twinning, and slip strain partitioning exhibited by polycrystalline, monoclinic nickel–titanium during large uniaxial deformations measured via in-situ neutron diffraction," *J. Mech. Phys. Solids*, vol. 61, no. 11, pp. 2302–2330, Nov. 2013, doi: 10.1016/j.jmps.2013.05.008.

[60] C. Yu, G. Kang, Q. Kan, and X. Xu, "Physical mechanism based crystal plasticity model of NiTi shape memory alloys addressing the thermo-mechanical cyclic degeneration of shape memory effect," *Mech. Mater.*, vol. 112, pp. 1–17, Sep. 2017, doi: 10.1016/j.mechmat.2017.05.005.

[61] P. Thamburaja, "Constitutive equations for martensitic reorientation and detwinning in shape-memory alloys," *J. Mech. Phys. Solids*, vol. 53, no. 4, pp. 825–856, Apr. 2005, doi: 10.1016/j.jmps.2004.11.004.

[62] P. Chowdhury and H. Sehitoglu, "Deformation physics of shape memory alloys – Fundamentals at atomistic frontier," *Prog. Mater. Sci.*, vol. 88, pp. 49–88, Jul. 2017, doi: 10.1016/j.pmatsci.2017.03.003.

[63] Y. Liu and D. Favier, "Stabilisation of martensite due to shear deformation via variant reorientation in polycrystalline NiTi," *Acta Mater.*, vol. 48, no. 13, pp. 3489–3499, Aug. 2000, doi: 10.1016/S1359-6454(00)00129-4.

[64] Y. Liu, Z. Xie, J. Van Humbeeck, and L. Delaey, "Asymmetry of stress–strain curves under tension and compression for NiTi shape memory alloys," *Acta Mater.*, vol. 46, no. 12, pp. 4325–4338, Jul. 1998, doi: 10.1016/S1359-6454(98)00112-8.

[65] J. X. Zhang, M. Sato, and A. Ishida, "Deformation mechanism of martensite in Ti-rich Ti–Ni shape memory alloy thin films," *Acta Mater.*, vol. 54, no. 4, pp. 1185–1198, Feb. 2006, doi: 10.1016/j.actamat.2005.10.046.

[66] M. A. Mitchell, F. E. Wang, and J. R. Cullen, "Electronic density of states in TiNi II and TiNi III," *J. Appl. Phys.*, vol. 45, no. 8, pp. 3337–3339, Aug. 1974, doi: 10.1063/1.1663782.

[67] A. V. Brodovoi *et al.*, "Titanium nickelide powder magnetic susceptibility," *Powder Metall. Met. Ceram.*, vol. 32, no. 4, pp. 355–360, Apr. 1993, doi: 10.1007/BF00560023.

[68] J. M. Peeters, E. E. H. van Faassen, and C. J. G. Bakker, "Magnetic resonance imaging of phase transitions in nitinol," *J. Biomed. Mater. Res. A*, vol. 80A, no. 4, pp. 938–945, Mar. 2007, doi: 10.1002/jbm.a.30966.

[69] D. Chovan, A. Gandhi, J. Butler, and S. A. M. Tofail, "Static magnetic susceptibility of radiopaque NiTiPt and NiTiEr," *J. Magn. Magn. Mater.*, vol. 452, pp. 451–457, Apr. 2018, doi: 10.1016/j.jmmm.2017.12.090.

[70] R. J. Wasilewski, S. R. Butler, and J. E. Hanlon, "On the Martensitic Transformation in TiNi," *Met. Sci. J.*, vol. 1, no. 1, pp. 104–110, Jan. 1967, doi: 10.1179/msc.1967.1.1.104.

[71] F. E. Wang, B. F. DeSavage, W. J. Buehler, and W. R. Hosler, "The Irreversible Critical Range in the TiNi Transition," *J. Appl. Phys.*, vol. 39, no. 5, pp. 2166–2175, Apr. 1968, doi: 10.1063/1.1656521.

[72] S. A. Shabalovskaya, "Phase Transitions in the Intermetallic Compound TiNi with Charge-Density Wave Formation," *Phys Stat Sol B*, vol. 132, no. 2, pp. 327–344, 1985, doi: 10.1002/pssb.2221320202.

[73] Y. Y. Ye, C. T. Chan, and K. M. Ho, "Structural and electronic properties of the martensitic alloys TiNi, TiPd, and TiPt," *Phys. Rev. B*, vol. 56, no. 7, pp. 3678–3689, Aug. 1997, doi: 10.1103/PhysRevB.56.3678.

[74] G. Bihlmayer, R. Eibler, and A. Neckel, "Electronic structure of the martensitic phases B19'-NiTi and B19-PdTi," *J. Phys. Condens. Matter*, vol. 5, no. 29, p. 5083, 1993.

[75] T. Fukuda, T. Kakeshita, H. Houjoh, S. Shiraishi, and T. Saburi, "Electronic structure and stability of intermetallic compounds in the Ti–Ni System," *Mater. Sci. Eng. A*, vol. 273–275, pp. 166–169, Dec. 1999, doi: 10.1016/S0921-5093(99)00283-X.

[76] S. E. Kulkova, V. E. Egorushkin, and V. V. Kalchikhin, "The electron structure of NiTi martensite," *Solid State Commun.*, vol. 77, no. 9, pp. 667–670, Mar. 1991, doi: 10.1016/0038-1098(91)90766-O.

[77] S. A. Shabalovskaja, A. I. Lotkov, I. I. Sasovskaja, A. G. Narmonev, and A. I. Zakharov, "Electron phase transition in TiNi?," *Solid State Commun.*, vol. 32, no. 9, pp. 735–738, 1979.

[78] M.-S. Choi, T. Fukuda, and T. Kakeshita, "Anomalies in resistivity, magnetic susceptibility and specific heat in iron-doped Ti–Ni shape memory alloys," *Scr. Mater.*, vol. 53, no. 7, pp. 869–873, Oct. 2005, doi: 10.1016/j.scriptamat.2005.05.040.

[79] S. Miyazaki, Y. Q. Fu, and W. M. Huang, "Overview of sputter-deposited TiNi based thin films," in *Thin Film Shape Memory Alloys*, S. Miyazaki, Y. Q. Fu, and W. M. Huang, Eds. Cambridge: Cambridge University Press, 2009, pp. 1–72.

[80] R. Lima de Miranda, C. Zamponi, and E. Quandt, “Micropatterned Freestanding Superelastic TiNi Films,” *Adv. Eng. Mater.*, vol. 15, no. 1–2, pp. 66–69, Feb. 2013, doi: 10.1002/adem.201200197.

[81] C. Bechtold, R. Lima de Miranda, and E. Quandt, “Capability of Sputtered Micropatterned NiTi Thick Films,” *Shape Mem. Superelasticity*, vol. 1, no. 3, pp. 286–293, Sep. 2015, doi: 10.1007/s40830-015-0029-9.

[82] J. Frenzel, E. P. George, A. Dlouhy, Ch. Somsen, M. F.-X. Wagner, and G. Eggeler, “Influence of Ni on martensitic phase transformations in NiTi shape memory alloys,” *Acta Mater.*, vol. 58, no. 9, pp. 3444–3458, May 2010, doi: 10.1016/j.actamat.2010.02.019.

[83] W. Tang, B. Sundman, R. Sandström, and C. Qiu, “New modelling of the B2 phase and its associated martensitic transformation in the Ti–Ni system,” *Acta Mater.*, vol. 47, no. 12, pp. 3457–3468, Sep. 1999, doi: 10.1016/S1359-6454(99)00193-7.

[84] S. Miyazaki and A. Ishida, “Martensitic transformation and shape memory behavior in sputter-deposited TiNi-base thin films,” *Mater. Sci. Eng. A*, vol. 273–275, pp. 106–133, Dec. 1999, doi: 10.1016/S0921-5093(99)00292-0.

[85] P. Krulevitch, A. P. Lee, P. B. Ramsey, J. C. Trevino, J. Hamilton, and M. A. Northrup, “Thin film shape memory alloy microactuators,” *J. Microelectromechanical Syst.*, vol. 5, no. 4, pp. 270–282, Dec. 1996, doi: 10.1109/84.546407.

[86] W.-S. Ko, B. Grabowski, and J. Neugebauer, “Development and application of a Ni-Ti interatomic potential with high predictive accuracy of the martensitic phase transition,” *Phys. Rev. B*, vol. 92, no. 13, p. 134107, Oct. 2015, doi: 10.1103/PhysRevB.92.134107.

[87] M. Buchner, K. Höfler, B. Henne, V. Ney, and A. Ney, “Tutorial: Basic principles, limits of detection, and pitfalls of highly sensitive SQUID magnetometry for nanomagnetism and spintronics,” *J. Appl. Phys.*, vol. 124, no. 16, p. 161101, Oct. 2018, doi: 10.1063/1.5045299.

[88] “3-078: Mondo Tronics : Flexinol® 100LT Muscle Wire.” [Online]. Available: https://www.jameco.com/z/3-078-Mondo-Tronics-Flexinol-reg-100LT-Muscle-Wire-5-Meters_357472.html.

[89] “Fort Wayne | Xylem Company.” [Online]. Available: http://www.xylemcompany.com/fort-wayne-metals.

[90] “Nitinol Technical Specifications: Discover the Unique Properties of Nitinol.” [Online]. Available: http://jmmedical.com/resources/221/Nitinol-Technical-Properties.html#nitinol-transformation-properties.

[91] Y. V. Kaletina, V. M. Schastlivtsev, and E. A. Fokina, “Effect of magnetic field on martensitic transformation in iron-nickel alloys with different size of austenite grains,” *Met. Sci. Heat Treat.*, vol. 50, no. 3–4, pp. 164–170, Mar. 2008, doi: 10.1007/s11041-008-9035-2.

[92] T. Kakeshita and T. Fukuda, “Effect of magnetic field on solid-solid phase transformations in iron-based ferromagnetic alloys,” *J. Phys. Conf. Ser.*, vol. 156, no. 1, p. 012012, 2009, doi: 10.1088/1742-6596/156/1/012012.

[93] R. Y. Umetsu, X. Xu, and R. Kainuma, “NiMn-based metamagnetic shape memory alloys,” *Scr. Mater.*, vol. 116, pp. 1–6, Apr. 2016, doi: 10.1016/j.scriptamat.2016.01.006.

[94] K. Shimizu and T. Kakeshita, “Effect of Magnetic Fields on Martensitic Transformations in Ferrous Alloys and Steels,” *ISIJ Int.*, vol. 29, no. 2, pp. 97–116, Feb. 1989, doi: 10.2355/isijinternational.29.97.

[95] H. Matsumoto, “Transformation behaviour of NiTi in relation to thermal cycling and deformation,” *Phys. B Condens. Matter*, vol. 190, no. 2, pp. 115–120, Jul. 1993, doi: 10.1016/0921-4526(93)90454-E.

[96] L. Jordan, M. Masse, J.-Y. Collier, and G. Bouquet, “Effects of thermal and thermomechanical cycling on the phase transformations in NiTi and Ni□Ti□Co shape-memory alloys,” *J. Alloys Compd.*, vol. 211–212, pp. 204–207, Sep. 1994, doi: 10.1016/0925-8388(94)90483-9.

[97] S. Miyazaki, Y. Igo, and K. Otsuka, “Effect of thermal cycling on the transformation temperatures of TiNi alloys,” *Acta Metall.*, vol. 34, no. 10, pp. 2045–2051, Oct. 1986, doi: 10.1016/0001-6160(86)90263-4.

[98] D. Jiles, *Introduction to magnetism and magnetic materials*, First. Chapman and Hall, 1991.

[99] M. S. Dresselhaus, *SOLID STATE PHYSICS*, vol. PART III, IV vols. 2001.

[100] G. Kresse and J. Furthmüller, “Efficiency of ab-initio total energy calculations for metals and semiconductors using a plane-wave basis set,” *Comput. Mater. Sci.*, vol. 6, no. 1, pp. 15–50, Jul. 1996, doi: 10.1016/0927-0256(96)00008-0.

[101] G. Kresse and J. Hafner, “Ab initio molecular dynamics for liquid metals,” *Phys. Rev. B*, vol. 47, no. 1, pp. 558–561, Jan. 1993, doi: 10.1103/PhysRevB.47.558.

[102] G. Kresse and J. Furthmüller, “Efficient iterative schemes for ab initio total-energy calculations using a plane-wave basis set,” *Phys. Rev. B*, vol. 54, no. 16, pp. 11169–11186, Oct. 1996, doi: 10.1103/PhysRevB.54.11169.

[103] P. E. Blöchl, “Projector augmented-wave method,” *Phys. Rev. B*, vol. 50, no. 24, pp. 17953–17979, Dec. 1994, doi: 10.1103/PhysRevB.50.17953.

[104] G. Kresse and D. Joubert, “From ultrasoft pseudopotentials to the projector augmented-wave method,” *Phys. Rev. B*, vol. 59, no. 3, pp. 1758–1775, Jan. 1999, doi: 10.1103/PhysRevB.59.1758.

[105] null Perdew, null Burke, and null Ernzerhof, “Generalized Gradient Approximation Made Simple,” *Phys. Rev. Lett.*, vol. 77, no. 18, pp. 3865–3868, Oct. 1996, doi: 10.1103/PhysRevLett.77.3865.

[106] P. E. Blöchl, O. Jepsen, and O. K. Andersen, “Improved tetrahedron method for Brillouin-zone integrations,” *Phys. Rev. B*, vol. 49, no. 23, pp. 16223–16233, Jun. 1994, doi: 10.1103/PhysRevB.49.16223.

[107] M. P. J. Punkkinen, K. Kokko, and I. J. Väyrynen, “Low-temperature specific heat of near-equiatomic Ni-rich B19′-TiNi-alloys,” *Solid State Commun.*, vol. 108, no. 8, pp. 567–571, Oct. 1998, doi: 10.1016/S0038-1098(98)00412-8.

[108] A. Kellou, Z. Nabi, A. Tadjer, N. Amrane, N. Fenineche, and H. Aourag, “Electronic study of FeTi, CoTi, and NiTi alloys: bulk, surfaces, and interfaces,” *Phys. Status Solidi B*, vol. 239, no. 2, pp. 389–398, Oct. 2003, doi: 10.1002/pssb.200301848.

[109] R. Dupree and D. J. W. Geldart, “Exchange enhancement of the spin susceptibility of metals,” *Solid State Commun.*, vol. 9, no. 2, pp. 145–149, Jan. 1971, doi: 10.1016/0038-1098(71)90275-4.

[110] S. V. Vonsovsky, M. I. Katsnelson, and A. V. Trefilov, “Anomalies in properties of d- and f-metals and alloys due to charge density fluctuations,” *J. Magn. Magn. Mater.*, vol. 61, no. 1, pp. 83–87, Sep. 1986, doi: 10.1016/0304-8853(86)90069-7.

[111] J. M. D. Coey, “Magnetism and Magnetic Materials by J. M. D. Coey,” *Cambridge Core*, Mar-2010. [Online]. Available: /core/books/magnetism-and-magnetic-materials/AD3557E2D4538CAA8488A8C1057313BC. [Accessed: 07-Oct-2019].

[112] K. Niitsu, Y. Kimura, X. Xu, and R. Kainuma, "Composition Dependences of Entropy Change and Transformation Temperatures in Ni-rich Ti–Ni System," *Shape Mem. Superelasticity*, vol. 1, no. 2, pp. 124–131, Jun. 2015, doi: 10.1007/s40830-015-0023-2.

[113] G. V. Minnigerode, "Göran Grimvall, E. P. Wohlfahrt (Eds.): The Electron-Phonon Interaction in Metals, Vol. 16, aus: Selected Topics in Solid State Physics. North Holland Publishing Company, Amsterdam, New York, Oxford 1981. 304 Seiten, Dfl 125,—," *Berichte Bunsenges. Für Phys. Chem.*, vol. 87, no. 5, pp. 453–454, 1983, doi: 10.1002/bbpc.19830870521.

[114] C. J. Kriessman and H. B. Callen, "The Magnetic Susceptibility of the Transition Elements," *Phys. Rev.*, vol. 94, no. 4, pp. 837–844, May 1954, doi: 10.1103/PhysRev.94.837.

[115] A. Nespoli *et al.*, "Non-Conventional Techniques for the Study of Phase Transitions in NiTi-Based Alloys," *J. Mater. Eng. Perform.*, vol. 23, no. 7, pp. 2491–2497, Jul. 2014, doi: 10.1007/s11665-014-1105-6.

[116] Z. G. Wang, X. T. Zu, S. Zhu, and L. M. Wang, "Temperature memory effect induced by incomplete transformation in TiNi shape memory alloy," *Mater. Lett.*, vol. 59, no. 4, pp. 491–494, Feb. 2005, doi: 10.1016/j.matlet.2004.10.029.

[117] L. Sun, T. X. Wang, and W. M. Huang, "Monitoring minor over-heating/cooling temperature based on the temperature memory effect in shape memory materials via DSC," *J. Therm. Anal. Calorim.*, pp. 1–13, Mar. 2018, doi: 10.1007/s10973-018-7188-9.

[118] Z. G. Wang, X. T. Zu, Y. Q. Fu, and L. M. Wang, "Temperature memory effect in TiNi-based shape memory alloys," *Thermochim. Acta*, vol. 428, no. 1, pp. 199–205, Apr. 2005, doi: 10.1016/j.tca.2004.11.018.

[119] L. Sun, W. M. Huang, and J. Y. Cheah, "The temperature memory effect and the influence of thermo-mechanical cycling in shape memory alloys," *Smart Mater. Struct.*, vol. 19, no. 5, p. 055005, Mar. 2010, doi: 10.1088/0964-1726/19/5/055005.

[120] Y. Liu, Z. Xie, J. V. Humbeeck, L. Delaey, and Y. Liu, "On the deformation of the twinned domain in Niti shape memory alloys," *Philos. Mag. A*, vol. 80, no. 8, pp. 1935–1953, Aug. 2000, doi: 10.1080/01418610008219095.

[121] G. Laplanche, T. Birk, S. Schneider, J. Frenzel, and G. Eggeler, "Effect of temperature and texture on the reorientation of martensite variants in NiTi shape memory alloys," *Acta Mater.*, vol. 127, pp. 143–152, Apr. 2017, doi: 10.1016/j.actamat.2017.01.023.

[122] A. Ishida, A. Takei, M. Sato, and S. Miyazaki, "Stress-strain curves of sputtered thin films of Ti−Ni," *Thin Solid Films*, vol. 281–282, pp. 337–339, Aug. 1996, doi: 10.1016/0040-6090(96)08634-8.

[123] G. Tan and Y. Liu, "Comparative study of deformation-induced martensite stabilisation via martensite reorientation and stress-induced martensitic transformation in NiTi," *Intermetallics*, vol. 12, no. 4, pp. 373–381, Apr. 2004, doi: 10.1016/j.intermet.2003.11.008.

[124] G. M. Michal and R. Sinclair, "The structure of TiNi martensite," *Acta Crystallogr. B*, vol. 37, no. 10, pp. 1803–1807, Oct. 1981, doi: 10.1107/S0567740881007292.

[125] S. D. Prokoshkin, A. V. Korotitskiy, V. Brailovski, K. E. Inaekyan, and S. M. Dubinskiy, "Crystal lattice of martensite and the reserve of recoverable strain of thermally and thermomechanically treated Ti-Ni shape-memory alloys," *Phys. Met. Metallogr.*, vol. 112, no. 2, p. 170, Aug. 2011, doi: 10.1134/S0031918X11020244.

[126] S. N. Kulkov and Yu. P. Mironov, “Martensitic transformation in NiTi investigated by synchrotron X-ray diffraction,” *Nucl. Instrum. Methods Phys. Res. Sect. Accel. Spectrometers Detect. Assoc. Equip.*, vol. 359, no. 1, pp. 165–169, May 1995, doi: 10.1016/0168-9002(94)01644-5.
[127] L. Héraud, “In situ synchrotron X-ray diffraction of the martensitic transformation in superelastic Ti-27Nb and NiTi alloys: a comparative study.”
[128] B. Zhang and M. L. Young, “High-energy synchrotron X-ray diffraction measurements of simple bending of pseudoelastic NiTi shape memory alloy wires,” *Powder Diffr.*, vol. 31, no. 2, pp. 104–109, Jun. 2016, doi: 10.1017/S0885715616000154.
[129] M. Mizuno, H. Araki, and Y. Shirai, “Compositional dependence of structures of NiTi martensite from first principles,” *Acta Mater.*, vol. 95, pp. 184–191, Aug. 2015, doi: 10.1016/j.actamat.2015.06.009.
[130] H. Sehitoglu *et al.*, “Superelasticity and Shape Memory Behavior of NiTiHf Alloys,” *Shape Mem. Superelasticity*, vol. 3, no. 2, pp. 168–187, Jun. 2017, doi: 10.1007/s40830-017-0108-1.
[131] X. Huang, G. J. Ackland, and K. M. Rabe, “Crystal structures and shape-memory behaviour of NiTi,” *Nat. Mater.*, vol. 2, no. 5, pp. 307–311, May 2003, doi: 10.1038/nmat884.
[132] M. F.-X. Wagner and W. Windl, “Lattice stability, elastic constants and macroscopic moduli of NiTi martensites from first principles,” *Acta Mater.*, vol. 56, no. 20, pp. 6232–6245, Dec. 2008, doi: 10.1016/j.actamat.2008.08.043.
[133] P. Šesták, M. Černý, J. He, Z. Zhang, and J. Pokluda, “Multiaxial stress–strain response and displacive transformations in NiTi alloy from first principles,” *Acta Mater.*, vol. 109, pp. 223–229, May 2016, doi: 10.1016/j.actamat.2016.02.043.
[134] W.-S. Ko, “Temperature dependence of NiTi martensite structures: Density functional theory calculations,” *Scr. Mater.*, vol. 154, pp. 134–138, Sep. 2018, doi: 10.1016/j.scriptamat.2018.05.037.
[135] J. Wang and H. Sehitoglu, “Resolving quandaries surrounding NiTi,” *Appl. Phys. Lett.*, vol. 101, no. 8, p. 081907, Aug. 2012, doi: 10.1063/1.4747488.
[136] X. L. Meng, W. Cai, Y. F. Zheng, Y. B. Rao, and L. C. Zhao, “Two-way shape memory effect induced by martensite deformation and stabilization of martensite in Ti36Ni49Hf15 high temperature shape memory alloy,” *Mater. Lett.*, vol. 57, no. 26–27, pp. 4206–4211, Sep. 2003, doi: 10.1016/S0167-577X(03)00291-X.
[137] Y. Liu, G. Tan, and S. Miyazaki, “Deformation-induced martensite stabilisation in [100] single-crystalline Ni–Ti,” *Mater. Sci. Eng. A*, vol. 438–440, pp. 612–616, Nov. 2006, doi: 10.1016/j.msea.2006.02.130.
[138] M. Piao, K. Otsuka, S. Miyazaki, and H. Horikawa, “Mechanism of the As Temperature Increase by Pre-deformation in Thermoelastic Alloys,” *Mater. Trans. JIM*, vol. 34, no. 10, pp. 919–929, 1993, doi: 10.2320/matertrans1989.34.919.
[139] MONIKA KUBENOVÁ, “PROCESSING AND MARTENSITIC TRANSFORMATIONS OF NiTi-BASED ALLOYS,” Brno university of technology, 2014.
[140] G. S. Firstov, R. G. Vitchev, H. Kumar, B. Blanpain, and J. Van Humbeeck, “Surface oxidation of NiTi shape memory alloy,” *Biomaterials*, vol. 23, no. 24, pp. 4863–4871, Dec. 2002, doi: 10.1016/S0142-9612(02)00244-2.
[141] B. G. Priyadarshini, S. Aich, and M. Chakraborty, “Nano-crystalline NiTi alloy thin films fabricated using magnetron co-sputtering from elemental targets: Effect of substrate conditions,” *Thin Solid Films*, vol. 616, no. Supplement C, pp. 733–745, Oct. 2016, doi: 10.1016/j.tsf.2016.09.034.

[142] S. Shabalovskaya, J. Anderegg, and J. Van Humbeeck, "Critical overview of Nitinol surfaces and their modifications for medical applications," *Acta Biomater.*, vol. 4, no. 3, pp. 447–467, May 2008, doi: 10.1016/j.actbio.2008.01.013.

[143] A. S. Dzhumaliev, Yu. V. Nikulin, and Yu. A. Filimonov, "Effect of annealing temperature and rate of sputtering on the magnetic properties and microstructure of the polycrystalline nickel films with (200) texture," *J. Commun. Technol. Electron.*, vol. 57, no. 5, pp. 498–505, May 2012, doi: 10.1134/S1064226912050038.

[144] E. Bonetti, E. G. Campari, L. Pasquini, and E. Sampaolesi, "Microstructure-related anelastic and magnetoelastic behavior of nanocrystalline nickel," *J. Appl. Phys.*, vol. 84, no. 8, pp. 4219–4226, Oct. 1998, doi: 10.1063/1.368639.

[145] P. Bhatt, S. M. Chaudhari, and M. Fahlman, "Influence of Ti layer thickness on solid state amorphization and magnetic properties of annealed Ti/Ni multilayer," *J. Phys. Condens. Matter*, vol. 19, no. 37, p. 376210, 2007.

[146] H. Aboulfadl, F. Seifried, M. Stüber, and F. Mücklich, "Interdiffusion in as-deposited Ni/Ti multilayer thin films analyzed by atom probe tomography," *Mater. Lett.*, vol. 236, pp. 92–95, Feb. 2019, doi: 10.1016/j.matlet.2018.10.085.

[147] L. Callegaro and E. Puppin, "Stress dependence of coercivity in Ni films: Thin film to bulk transition," *Appl. Phys. Lett.*, vol. 68, no. 9, pp. 1279–1281, Feb. 1996, doi: 10.1063/1.115952.

[148] M. Weiler *et al.*, "Voltage controlled inversion of magnetic anisotropy in a ferromagnetic thin film at room temperature," *New J. Phys.*, vol. 11, no. 1, p. 013021, Jan. 2009, doi: 10.1088/1367-2630/11/1/013021.

[149] R. C. O'Handley, *Modern magnetic materials: principles and applications*. New York: Wiley, 2000.

[150] Brown, W. F., *Magnetic Materials, Ch 8 in the Handbook of Chemistry and Physics*. Condon and Odishaw, eds., McGraw-Hill, 1958.

[151] R. R. Birss and E. W. Lee, "The Saturation Magnetostriction Constants of Nickel within the Temperature Range - 196 to 365 C," *Proc. Phys. Soc.*, vol. 76, no. 4, pp. 502–506, Oct. 1960, doi: 10.1088/0370-1328/76/4/307.

[152] Z. Tang *et al.*, "Magneto-mechanical coupling effect in amorphous Co40Fe40B20 films grown on flexible substrates," *Appl. Phys. Lett.*, vol. 105, no. 10, p. 103504, Sep. 2014, doi: 10.1063/1.4895628.

Resumé étendu

De nombreuses technologies existantes ou en développement reposent sur le contrôle de la direction d'aimantation d'un matériau ferromagnétique : capteurs microélectroniques, actionneurs et notamment des technologies de l'information telles que les disques durs ou les mémoires à accès sélectif magnétique (MRAM), etc. La miniaturisation et la réduction de la consommation d'énergie ont conduit à l'émergence de nouveaux domaines de recherche, tels que la spintronique [3] ou la straintronique (technologies impliquant des effets de contrainte) [4]. Les technologies d'enregistrement magnétique nécessitent non seulement une densité de bits (1 ou 0) croissante, mais également les nouvelles approches efficaces pour réduire la puissance nécessaire à la réécriture du bit. Cela place au premier plan les recherches sur le contrôle de l'anisotropie magnétique.

L'objectif initial de la thèse est d'étudier la manipulation de l'anisotropie magnétique d'une couche mince ferromagnétique par déformation dans une bicouche NiTi/ ferromagnétique où NiTi est un alliage à mémoire de forme. Dans une première partie de la thèse, les caractéristiques structurelles et la nature paramagnétique du NiTi sont étudiées. Dans une seconde partie, le couplage magnétoélastique dans une bicouche NiTi/Ni est étudié.

Le premier chapitre de la thèse est consacré à fournir au lecteur des informations de base et nécessaires à l'étude de la thèse. Les méthodes de manipulation des propriétés magnétiques telles que l'anisotropie magnétocristalline sont présentées dans le contexte de ses applications technologiques. L'attention est portée sur le rôle des interfaces et des mécanismes physiques sous-jacents. Le contrôle de l'anisotropie sous tension et sous contrainte dans des systèmes multiferroiques est en particulier discuté. Dans ce contexte général, les alliages à mémoire de forme apparaissent comme des candidats potentiellement intéressants pour les technologies magnétiques assistées par contrainte. Une seule démonstration expérimentale a été publiée en cours de thèse (en 2016 puis 2017) par le même groupe de recherche chinois. Les auteurs ont montré qu'ils pouvaient modifier l'anisotropie d'une film mince ferromagnétique au moyen d'un couplage structural avec un alliage à mémoire de forme dans NiTiNb / Fe et dans NiTiNb / FePt. En parallèle nous avions également fait le choix du NiTi car celui-ci peut être

déposé par pulvérisation cathodique, donc compatible avec des systèmes d'électronique de spin ou des média magnétiques usuels.

Au début du chapitre II, nous décrivons la méthode de croissance par dépôt physique en phase vapeur, gravure et structuration des échantillons auto-portés de NiTi (20 microns) utilisés dans l'ensemble de la thèse. La composition est mesurée comme étant proche de la composition Ni49.5 Ti51.5. Les échantillons ont été caractérisés par diffraction des rayons X (XRD) et par microscopie électronique à transmission (MET). Ces mesures ont révélé une transformation de martensite B2-B19 et, dans certains cas, une transformation de B2-R-B19. Aucune impureté, ségrégation ou autre phase que NiTi ne sont révélées. Après analyse de la structure, les techniques de magnétométrie permettre de mettre en lumière la nature paramagnétique de l'alliage NiTi. Les valeurs de susceptibilité sont différentes selon la phase cristalline : 2,2 10^{-6} en phase martensite et de $3{,}2\times10^{-6}$ en phase austénite. Celles-ci sont conformes avec les données trouvées dans la littérature. Dans la littérature, le sujet de l'origine du paramagnétisme est peu traité. Nous montrons ici que les valeurs de susceptibilité magnétique et leur dépendance en température ne peuvent s'expliquer que sur la base du paramagnétisme de Pauli. Le rapport expérimental des valeurs susceptibilités magnétiques en martensite et austénite, est proche ; toutefois, la susceptibilité magnétique calculée à partir de la densité d'états électronique (DOS) à l'énergie de Fermi est 4 à 5 fois plus petite que celle mesurée expérimentalement. Les termes d'interaction d'échange, l'influence de la température la température et le désordres chimique permettent de corriger significativement cette différence. Les limites du modèle d'électron libre face aux particularités du système électronique NiTi [74][108], et à la forme particulière de la DOS sont discutées. La variation de la température de la susceptibilité magnétique dans les deux phases est discuté indépendamment en considérant une variation en tempéarture de la DOS et des paramètres de maille cristallins. En phase martensite, le DOS augmente dans le même intervalle que la susceptibilité magnétique mesurée expérimentalement (<+ 2,2%> par expérience, par rapport à + 0,15% à + 7,5%, selon la méthode). En phase austénitique, l'une des méthodes utilisées suggère une augmentation de la DOS (0,3-0,6%), tandis que l'autre - une diminution (-0,4%), mais dans les deux cas, le changement est proche de zéro. La variation des résultats moyens observée expérimentalement est de +1,2%.

Il est connu que le NiTi soumis à un cycle thermique subit un effet de stabilisation de la transformation martensitique. Cet effet a été observé via des mesures

magnétiques, démontrant l'utilité du magnétisme pour caractériser de façon indirecte de tels effets structuraux. En revanche, aucune influence notable d'un champ magnétique externe sur les températures de transformation et l'amplitude M (T) n'a été observée. Le changement d'aimantation de l'alliage NiTi reflète non seulement la transformation entre la martensite et l'austénite, mais également la phase R intermédiaire. Par conséquent, la magnétométrie peut être considérée comme une technique alternative de sondage et d'analyse de la transformation de la martensite. Comme dans le cas des tests thermomécaniques classiques, les mesures de magnétométrie peuvent être réalisables pour une contrainte constante (diagramme de température de phase en fonction du niveau de contrainte) ou d'autres mesures susceptibles d'étudier l'influence des conditions mécaniques ou thermiques sur la transformation de la martensite et l'effet de mémoire de forme. De plus, la magnétométrie est une méthode non-destructive et à distance.

Le chapitre II est donc consacré aux propriétés magnétiques du NiTi et à leur corrélation avec la structure cristalline et la densité d'états. Le chapitre III en est une extension consacrée à l'étude des modifications du magnétisme avec la déformation. Premièrement, parce que la tension devrait modifier la structure du NiTi aux niveaux macro et microscopique. Deuxièmement, la déformation étant la procédure courante du traitement au NiTi, il est nécessaire d'induire un effet de mémoire de forme dans l'alliage. Ce dernier sera appliqué au contrôle de l'anisotropie magnétique dans le dernier chapitre. Premièrement, des expériences de déformation en traction de NiTi en phase martensite au moyen d'une machine de traction et de corrélation d'images numériques ont été réalisées. La distribution de la déformation dans l'échantillon est étudiée pour différentes valeurs de déformation maximales. L'effet de mémoire de forme induit par la déformation en traction est mesuré et quantifié. Ensuite, la structure cristalline de NiTi est étudiée en fonction de la déformation au moyen de techniques de diffraction des rayons X. La déformation en traction génère un changement monotone des paramètres de réseau dans la structure monoclinique, principalement caractérisée par une augmentation de l'angle monoclinique β. La même tendance est retrouvée dans la littérature comme conséquence de la minimisation d'énergie ou d'influences externes. De façon étonnante, les variations inverses sont obtenues après un cycle thermique complet pour les mêmes échantillons de NiTi déformés. Parmi les conclusions majeures, nous démontrons que le réseau monoclinique de NiTi se réoriente de manière à avoir une direction préférentielle le long de la contrainte de traction appliquée. Enfin, nous avons conclu de nos observations que dans l'échelle du réseau cristallin, le système réagissait

à la contrainte appliquée par une réorientation et une distorsion analogue à celles du cisaillement.

De tels changements systématiques au niveau du réseau cristallin influence le paramagnétisme de Pauli. La déformation en traction de NiTi se traduit par une augmentation de l'amplitude de susceptibilité magnétique entre les phases de martensite et d'austénite. Ensuite, après la transition thermique vers la phase austénitique à haute température et le retour à la martensite, la même amplitude de susceptibilité magnétique diminue, comparée à celle d'un échantillon non déformé. L'influence de la déformation sur la phase austénitique est faible et l'amplitude de la transition est principalement lié à une variation de susceptibilité magnétique $\Delta\chi$ en phase martensite avec la traction puis encore après un cycle de transformation martensitique. La dépendance de susceptibilité à la contrainte de $\Delta\chi$ est linéaire similairement au décalage en température de stabilisation de la martensite. Des calculs électroniques de densité d'états ont été effectués sur la base des paramètres de réseau extraits à des mesures DRX en fonction de la contrainte. En accord avec les mesures magnétiques, la densité d'états à l'énergie de Fermi correspondant à l'échantillon déformé diminue et augmente respectivement après l'état de chauffage. Ce résultat confirme lien entre la densité d'état au niveau de Fermi et paramagnétisme, comme attendu pour un alliage paramagnétique de Pauli. La prise en compte du facteur d'amélioration des échanges peut placer les susceptibilités magnétiques résultant des calculs de DOS dans la plage des valeurs observées expérimentalement, mais la dépendance n'est pas toujours pas linéaire, comme obtenu expérimentalement. Certaines autres contributions comme les dislocations ne sont pas prises en compte par notre modèle ab-initio alors qu'on sait qu'elles jouent un rôle important dans la naissance de l'effet mémoire de forme.

Dans le chapitre IV, le couplage magnétoélastique dans une bicouche Ni/ NiTi est étudié. Premièrement, 20 nm de Ni puis 5 nm de Pt sont déposés par dépôt physique en phase vapeur sur des substrats de NiTi préalablement étirés. La surface de Ni et NiTi a été analysée par microscopie à force atomique (magnétique), sa rugosité et ses domaines magnétiques ont été caractérisés. La microscopie électronique à transmission de la section transversale NiTi/Ni a été utilisée pour évaluer la qualité de l'interface. L'interface NiTi/Ni est peu rugueuse mais une couche d'oxyde NiTiOx agit comme une couche tampon entre Ni et NiTi. Des mesures magnétométriques dans le plan de l'échantillon en fonction de l'angle d'application du champ ont été effectuée pour

l'ensemble des échantillons NiTi/Ni, préalablement étirés dans la gamme de 3% à 11%. Nous avons démontré la formation d'une anisotropie magnétique uniaxiale dans la couche de Ni, pouvant atteindre $1 \cdot 10^5$ J/m3. Cette valeur est parmi les plus importantes de la littérature observée sur une film mince de Ni. La commutation de cette anisotropie est ensuite induite thermiquement à cause d'une contrainte en compression générée par l'effet de mémoire de forme. L'anisotropie peut ainsi être plus généralement contrôlée dans la couche de Ni en fonction de la phase cristalline de NiTi et du stade de dépôt de Ni. Nous démontrons ici la commutation de manière reproductible de l'anisotropie du nickel de 90 ° en passant de la température ambiante à 400 K, et inversement. L'anisotropie à haute température est beaucoup plus basse que celle à basse température, non pas du fait de la température elle-même mais bien de l'état de contrainte produit par le NiTi. La déformation de la couche de Ni a été soigneusement estimée à partir des données magnétiques et vérifiée avec les mesures TEM. Nous concluons que dans notre bicouche NiTi/Ni, 1.6% de déformation dans le plan de NiTi produise en moyenne 1% de déformation dans la couche Ni. Ce résultat est prometteur dans la mesure où de nombreux paramètres tels que l'accord des réseaux cristallins de NiTi et Ni, l'épaisseur de la couche ferromagnétique, l'amplitude de l'effet de forme, et la disparition de l'oxyde d'interface peuvent très certainement l'améliorer significativement. Tenant compte de la possibilité d'ajuster les températures caractéristiques et la largeur d'hystérésis de la transformation de la martensite dans les alliages à base de NiTi, ainsi que d'ajuster la quantité de déformation libérée lors de cette transformation, cette approche est prometteuse pour la gamme de technologies. Nous avons d'ailleurs proposé durant la thèse son utilisation pour un capteur de température.